

1
2
3
4
5
6
7
8
9
10
11
12

**DALROMS-NWA12 v1.0, a coupled circulation-ice-
biogeochemistry modelling system for the northwest Atlantic
Ocean: Development and validation**

Kyoko Ohashi¹, Arnaud Laurent¹, Christoph Renkl¹, Jinyu Sheng¹, Katja Fennel¹, Eric Oliver¹

¹Department of Oceanography, Dalhousie University, Halifax, NS B3H 4R2 Canada

Correspondence to: Kyoko Ohashi (kyoko.ohashi@dal.ca)

2 October 2024

13 **Abstract.** This study presents DalROMS-NWA12 v1.0, a coupled ocean circulation-sea ice-
14 biogeochemistry modelling system for the northwest Atlantic Ocean (NWA) in which the
15 circulation and biogeochemistry modules are based on ROMS (Regional Ocean Modeling
16 System). The circulation module is coupled to a sea ice module based on the Community Ice
17 CodE (CICE), and the physical ocean state simulated by the circulation module drives the
18 biogeochemical module. Study of the biological carbon pump in the NWA is one of the main
19 intended applications of this model. Global atmospheric and ocean reanalyses are used
20 respectively to force DalROMS-NWA12 at the sea surface and as part of its lateral boundary
21 input. The modelling system is also forced by tides, riverine freshwater input, and continental
22 runoff. The physical ocean state and sea ice from two simulations of the period 2015–2018, with
23 and without nudging of the simulated temperature and salinity towards a blend of observations
24 and reanalysis, are examined in this study. Statistical comparisons between model results and
25 observations or reanalyses show the control (nudged) simulation outperforms the prognostic (un-
26 nudged) simulation in reproducing the paths of the Gulf Stream and the West Greenland Current,
27 as well as propagation of the estuarine plume in the Gulf of St. Lawrence. The prognostic
28 simulation performs better in simulating the sea ice concentration. The biogeochemical module,
29 which is run only in the control simulation, performs reasonably well in reproducing the
30 observed spatiotemporal variations of oxygen, nitrate, alkalinity, and total inorganic carbon. To
31 examine the effects of tides and sea ice on the physical fields in the study area, results of
32 simulations from which either component is absent are compared to results of the prognostic
33 simulation. In the absence of tides, Ungava Bay in summer experiences a simulated surface
34 salinity that is higher by up to ~ 7 psu than in the simulation with tides, as well as changes in
35 horizontal distributions of surface temperature and sea ice. Without coupling to the sea ice
36 module, the circulation module produces summertime sea surface temperatures that are higher by
37 up to $\sim 5^\circ\text{C}$ in Baffin Bay.

38 **1 Introduction**

39 The northwest North Atlantic Ocean (hereafter NWA) is characterized by interactions among
40 physical and biogeochemical processes that affect the global atmosphere-ocean system. Air-to-
41 sea flux of CO₂ per unit area is estimated to be largest in the world in the Atlantic Ocean north of
42 50° N, due to factors such as strong winds in winter and high primary production in spring
43 (Takahashi et al., 2009). The sinking of particles formed during primary production has the effect
44 of transporting atmospheric CO₂ to the deep ocean and is referred to as the biological carbon
45 pump (BCP; Volk and Hoffert, 1985). The BCP is influenced by various physical processes over
46 an annual cycle. The presence of sea ice in winter can, on one hand, drive upward transport of
47 nutrients through brine rejection-induced vertical mixing (Jin et al., 2018) but on the other hand
48 can reduce wind-induced mixing (Rainville et al., 2011) and attenuate the solar radiation
49 (Legendre et al., 1992) by isolating the water column from the atmosphere. Seasonal changes of
50 the mixed layer depth is another physical process that governs the BCP. Shoaling of the layer in
51 spring, driven by freshwater input from runoff and sea ice, promotes primary production (Wu et
52 al., 2007 and 2008; Frajka-Williams and Rhines, 2010), while deepening of the layer in winter
53 can result in entrainment of dissolved inorganic carbon and respiratory CO₂ that had been in
54 shallow sub-surface waters (Körtzinger et al., 2008). In the Labrador Sea, deep convection in
55 winter is thought to be an additional pathway for removal of carbon from near-surface waters
56 (Tian et al., 2004).

57 Several field programs have been conducted to quantify the major processes at work in the
58 NWA, such as the Labrador Sea Deep Convection Experiment (The Lab Sea Group, 1998),
59 which focused on atmospheric and physical oceanographic processes, and the Atlantic Zone
60 Monitoring Program (Pepin et al., 2005) and its off-shelf counterpart (e.g., Yashayaev and Loder,
61 2017), which have made regular shipboard measurements of physical and biogeochemical (BGC)
62 fields at fixed locations. Simultaneous measurements of physical and BGC fields at moorings
63 (e.g., Martz et al., 2009; Strutton et al., 2011) and by profiling floats (e.g., Yang et al., 2020;
64 Wang and Fennel 2022) have expanded the coverage of observations, which is crucial given the
65 spatiotemporal variability in the processes that govern the BCP (Garçon et al., 2001).

66 Process-based numerical models can complement observations of oceanic processes by
67 providing four-dimensional estimates of relevant fields and by enabling experiments in which the
68 effects of key inputs are isolated or the future state of oceans under various climate scenarios are
69 simulated (Fennel et al., 2022). Early numerical studies of the NWA using coupled ocean
70 circulation-sea ice models focused mainly on specific processes, such as climatological sea ice
71 conditions (Mysak et al., 1991), sea ice variabilities on the interannual (Ikeda et al., 1996) and
72 intra-seasonal (Yao et al., 2000) time scales, and changes in sea ice and mixed layer properties
73 under different atmospheric conditions (Tang et al., 1999). As process-based numerical models
74 grew in complexity they yielded new insights, such as the role of sea ice's heat capacity in the
75 timing of ice melt (Zhang et al., 2004). Advances in computational power have led to realistic
76 simulations spanning a decade or more covering limited areas, such as the Canadian Arctic
77 Archipelago and Davis Strait (Lu et al., 2014) or the Labrador and Newfoundland Shelves (Ma et
78 al., 2016). Other ocean-ice models of areas within the NWA include that of the Gulf of St.
79 Lawrence and surrounding waters (Urrego-Blanco and Sheng, 2014; Wang et al., 2020), Hudson
80 Bay (Saucier et al., 2004), and the Labrador Sea (Pennelly and Myers, 2020). Canadian
81 government agencies have developed coupled ocean-ice or atmosphere-ocean-ice models to
82 support activities such as hazard management, with domains ranging from the regional (e.g.,
83 Smith et al., 2013 for the Gulf of St. Lawrence) to basin-wide (Dupont et al., 2015; Wang et al.,
84 2018). Other modelling studies have focused on hydrodynamics in coastal and shelf waters of the
85 NWA, such as Han et al. (1997) for the Scotian Shelf, Wu et al. (2012) for the area between the
86 Gulf of Maine and Baffin Bay, and Chen and He (2015) for the Mid-Atlantic Bight and the Gulf
87 of Maine.

88 As for coupled physical-BGC modelling studies, three-dimensional models with high resolutions
89 have generally focused on the shelf and slope areas of the NWA. Pei (2022) used a simple
90 oxygen model to study seasonal changes in dissolved oxygen over the Scotian Shelf, while more
91 complex models have been used to study the biogeochemistry and plankton dynamics of the
92 Scotian Shelf and surrounding waters (Laurent et al., 2021, Rutherford and Fennel, 2022) and the
93 Gulf of St. Lawrence (LeFouest et al., 2010; Lavoie et al., 2021). Ross et al. (2023) developed a
94 coupled physical-BGC model for the North Atlantic Ocean from the Caribbean Sea to the
95 southern Labrador Sea, designed primarily for marine resource management.

96 As coupled simulations that include more processes and cover larger extents of space and time
97 become feasible, they are expected to enhance our understanding of how the ocean functions as
98 an integrated system, as well as how this system might change under various scenarios of the
99 future climate. In this study, we present and assess a coupled ocean circulation-sea ice-BGC
100 model that has been developed recently with the primary goal of studying the interactions
101 between physical and BGC processes in the NWA, including the BCP. Advantages of this
102 model's configuration include: (a) a domain that spans the area from the Mid-Atlantic Bight to
103 Baffin Bay, allowing for a wide range of oceanographic processes that can be examined; (b) a
104 horizontal grid size of $O(1 \text{ km})$ that decreases with latitude, such that the first baroclinic Rossby
105 radius of deformation (Chelton et al., 1998) is spanned by about four grid boxes everywhere; (c)
106 the use of a terrain-following vertical coordinate system, which can produce more realistic near-
107 bottom vertical mixing and bottom boundary layer structures than the step-wise bottom
108 topography of z-level grids (Ezer and Mellor, 2004); (d) the inclusion of tides (as one of the
109 model inputs) and sea ice (through coupling between the circulation and sea ice modules), both
110 of which are important elements of the ocean system in this region, and (e) the inclusion of a
111 BGC module, which enables the study of how processes such as the BCP are driven by the
112 coupled ocean circulation-sea ice system. This paper provides an assessment of the coupled
113 model's performance as well as sensitivity studies designed to elucidate the role of two physical
114 processes, tides and sea ice. The components of the coupled model and the simulations are
115 described in the next section. In Sect. 3, the results of two simulations, with and without nudging
116 of the temperature and salinity towards a blend of observations and reanalysis (referred to
117 respectively as the control and prognostic simulations), are described and quantitatively
118 compared to observations or reanalysis. In addition, depth vs. time plots of simulated
119 temperature are used to qualitatively assess the model's performance in reproducing the effects
120 of winter convection in the Labrador Sea. In Sect. 4, the roles of tides and sea ice in the physical
121 fields of the NWA are examined by comparing the results of two additional simulations, one
122 without tidal forcing and the other without the simulation of sea ice, to results of the prognostic
123 simulation described in Sect. 3. A summary of our findings is presented in the concluding
124 section.

125 **2 Model setup and forcing**

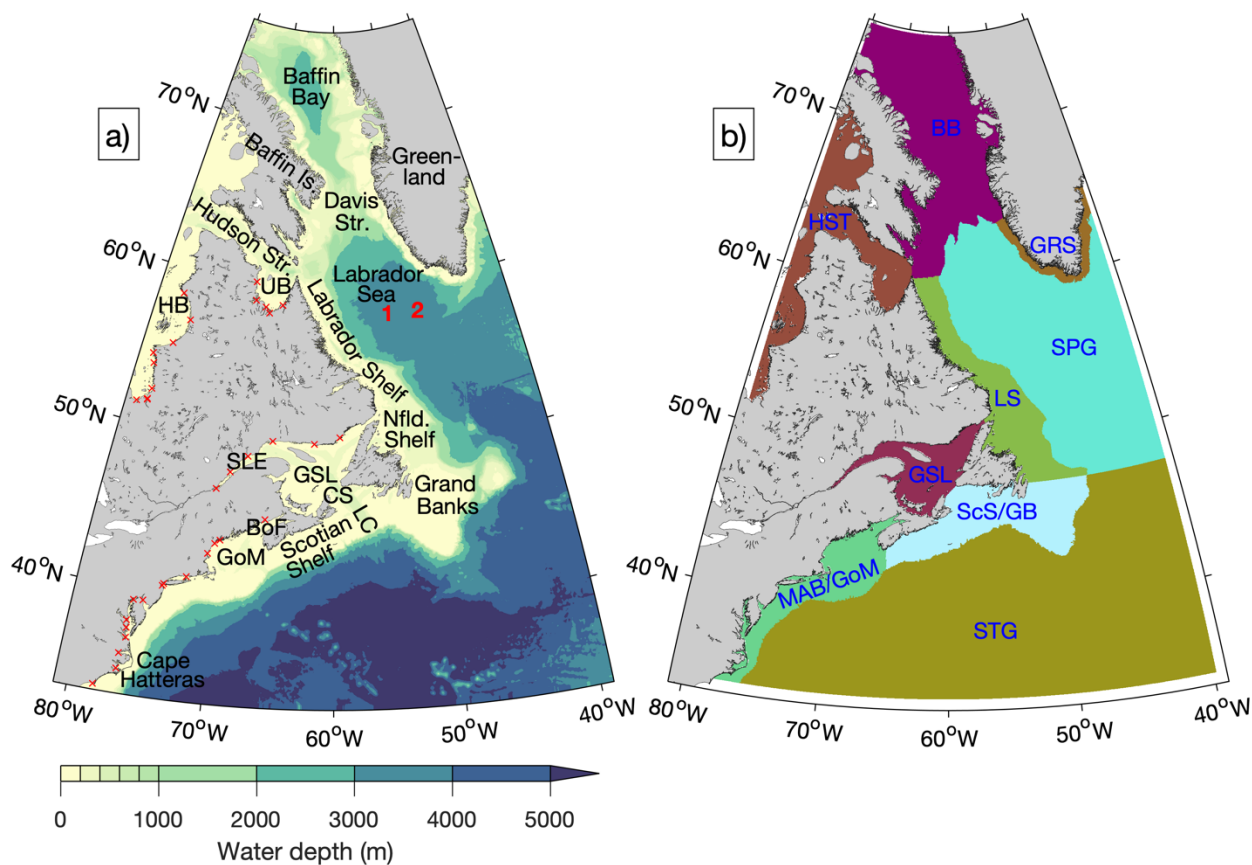
126 The coupled circulation-sea ice-BGC modelling system used in this study consists of three
127 modules: an ocean circulation module based on ROMS (Regional Ocean Modeling System,
128 version 3.9; Haidvogel et al., 2008), a sea ice module based on CICE (Community Ice Code,
129 version 5.1; Hunke et al., 2015), and a BGC module within ROMS based on the work of Fennel
130 et al. (2006, 2008) with updates as described by Laurent et al. (2021). The circulation and sea ice
131 modules are coupled using the software MCT (Model Coupling Toolkit, version 2.10; Jacob et
132 al., 2005; Larson et al., 2005) in a manner similar to Kristensen et al. (2017). Yang et al. (2023)
133 found good agreement between simulated and observed values of tides and storm surges
134 simulated by a barotropic version of the ocean circulation module.

135 ROMS is a three-dimensional (3D) numerical circulation model with a free surface and the
136 terrain-following S-coordinate system (originally developed by Song and Haidvogel (1994)) in
137 the vertical. The vertical layers are placed more densely near the surface and bottom in deep
138 waters, and more uniformly in shallow waters. In this study ROMS has 40 vertical S-layers,
139 whose configuration is described in Appendix A. ROMS and CICE use the same horizontal grid
140 and bathymetry, with the domain covering the area between $\sim 81^\circ$ W and $\sim 39^\circ$ W and between
141 $\sim 33.5^\circ$ N and $\sim 76^\circ$ N (Fig. 1a). The grid resolution in the east-west direction is $1/12^\circ$, resulting
142 in grid box dimensions of ~ 8 km on each side near the grid's southern boundary and ~ 2 km on
143 each side near the northern boundary.

144 The model bathymetry is derived from the $1/240^\circ$ -resolution data set GEBSCO_2019 (GEBSCO
145 Compilation Group, 2019). After the GEBSCO data were linearly interpolated onto the model
146 grid, the Shapiro filter (Shapiro, 1975) was applied to seamounts in deep waters from $\sim 67.5^\circ$ W
147 to $\sim 42^\circ$ W and from $\sim 34^\circ$ N to $\sim 48^\circ$ N to reduce currents caused by spurious pressure gradients.
148 No other smoothing was applied to the bathymetry. To avoid model instability caused by strong
149 currents entering the model domain at an angle, the model bathymetry and land-sea mask in the
150 first four grid boxes from each lateral boundary were set to the same values as in the fifth grid
151 box from the boundary.

152 The advection schemes used in ROMS for physical fields are: (a) the third-order upstream
153 scheme for horizontal advection of physical tracers and 3D momentum and (b) the fourth-order

154 centered scheme for horizontal advection of two-dimensional momentum and for vertical
 155 advection of physical tracers and 3D momentum. The horizontal eddy viscosity and diffusivity in
 156 ROMS are set to zero because the third-order upstream scheme generates some numerical
 157 diffusion which is large enough to eliminate small-scale features associated with numerical
 158 noise. Vertical mixing is parameterized using the “2.5-level” scheme of Mellor and Yamada
 159 (1982) with modifications as described by Allen et al. (1995). The time step is 6 seconds for the
 160 external (barotropic) mode and 120 seconds for the internal (baroclinic) mode.



161
 162 **Figure 1. (a)** Model domain and bathymetry. Locations of river mouths are indicated by red X marks. Locations for
 163 which depth profiles of simulated temperature are shown in Fig. 16 are indicated by numbers in red. Abbreviations
 164 are used for: Island (Is.), Strait (Str.), Hudson Bay (HB), Ungava Bay (UB), Newfoundland (Nfld.), St. Lawrence
 165 Estuary (SLE), Gulf of St. Lawrence (GSL), Cabot Strait (CS), Laurentian Channel (LC), Bay of Fundy (BoF), and
 166 Gulf of Maine (GoM). **(b)** Regions in which metrics of model performance are calculated. The regions are: GRS
 167 (Greenland Shelf), HST (Hudson Strait), BB (Baffin Bay), LS (Labrador Shelf), SPG (Subpolar Gyre), GSL (Gulf of
 168 St. Lawrence), ScS/GB (Scotian Shelf/Grand Banks), MAB/GoM (Mid-Atlantic Bight/Gulf of Maine), and STG
 169 (Subtropical Gyre). Areas within 10 grid points of lateral boundaries are excluded from the error metric calculations.

170 Atmospheric fields used to drive the coupled model are derived from the hourly reanalysis data
171 set known as ECMWF Reanalysis v5 (ERA5; Hersbach et al., 2018) which has a horizontal grid
172 spacing of $1/4^\circ$. Within ROMS, the bulk flux scheme of Fairall et al. (1996a, 1996b) is used to
173 calculate the surface fluxes of heat and fresh water. Lateral open boundary conditions are
174 specified using the explicit scheme of Chapman (1985) for sea surface elevation, the Shchepetkin
175 scheme (Mason et al., 2010) for the normal component and the implicit scheme of Chapman
176 (1985) for the tangential component of depth-averaged currents, and the adaptive scheme of
177 Marchesiello et al. (2001) for the normal and tangential components of depth-varying currents as
178 well as all tracers. In the adaptive boundary condition, the nudging time scale is three days for
179 inflow and 360 days for outflow. The values of currents, temperature, salinity, and sea surface
180 elevation specified at the lateral boundaries are derived from the daily fields of Copernicus
181 global $1/12^\circ$ oceanic and sea ice reanalysis (GLORYS12V1, hereafter GLORYS; Lellouche et
182 al., 2021) for the simulation period. In order to ensure that the simulated ocean states near lateral
183 open boundaries are as realistic as possible, the lateral boundary conditions of currents,
184 temperature, and salinity are supplemented by nudging the simulated values near boundaries
185 towards GLORYS values. The nudging time scale is three days at the grid point closest to a
186 lateral boundary and decreases linearly to zero over ten grid points moving away from the
187 boundary. Tidal elevation and currents are specified at the lateral boundaries from the global tidal
188 model solution TPXO9v2a (an updated version of the model by Egbert and Erofeeva (2002)),
189 with a horizontal grid size of $1/6^\circ$ and 15 tidal constituents.

190 Riverine freshwater input from 35 rivers (Table 1) is specified as volume flux through the bottom
191 of a model grid cell (www.myroms.org/forum/viewtopic.php?t=5156). Each river is represented
192 by a channel normal to the model's coastline, at the head of which the surface elevation, vertical
193 velocity, and tracer values are adjusted according to the river discharge. The river water has a
194 salinity of 0.4 psu (salinity in the Practical Salinity Scale is dimensionless but we use the unit
195 "psu" for clarity) and a temperature equal to that of the GLORYS sea surface temperature at the
196 grid point closest to the river mouth. For the St. Lawrence River, we use the monthly-mean
197 discharge at Quebec City estimated by the St. Lawrence Global Observatory (2023) using the
198 regression model of Bourgault and Koutitonsky (1999). For all other rivers, we use the monthly-
199 mean data set of Dai (2017) that was updated in May 2019, substituting climatological values

200 calculated over the period 1900–2018 for months with no data. Freshwater flux across coastlines
 201 due to the melting of ice and snow over land is specified as an addition to the sea surface height
 202 and the surface freshwater flux at the appropriate model grid boxes. This freshwater flux is
 203 derived from the monthly data set of Bamber et al. (2018), who combined satellite observations
 204 of glaciers with the output of a regional climate model. A monthly climatology of this data set,
 205 which covers the period 1958–2016, is used in simulations of the period after December 2016.
 206 Both the riverine and continental freshwater fluxes are converted to “pseudo-means” (monthly

207 **Table 1.** Names and discharge locations of rivers in the coupled model.

River	Lon. (° W)	Lat. (° N)	River	Lon. (° W)	Lat. (° N)
Innuksuac	78.06	58.42	Saguenay	69.72	48.06
Nastapoca	76.56	56.91	St. Lawrence	70.81	46.94
Great Whale	77.81	55.28	Saint John	66.14	45.32
Roggan	79.56	54.37	Androscoggin	69.89	43.78
La Grande + Sakami	79.22	53.78	Saco	70.31	43.54
Eastmain	78.72	52.23	Merrimack +	70.81	42.87
Rupert	78.89	51.56	Pemigewasset		
Nottaway	78.89	51.51	Connecticut	72.31	41.26
Harricana	79.89	51.30	Hudson	74.06	40.63
Arnaud	69.64	60.04	Passaic (Ramapo)	74.14	40.50
Leaf	69.39	58.90	Delaware + Beaver Kill	75.47	39.42
Koksoak (Caniapiscau + Mélézes)	68.14	58.55	Susquehanna	76.22	39.35
False + Whale	67.64	58.20	Potomac	76.47	38.05
George	66.14	58.77	Rapidan +	76.39	37.59
Petit Mécatina	59.39	50.62	Rappahannock		
Natashquan	61.89	50.19	James	76.31	36.99
Moisie	65.97	50.24	Roanoke	76.64	35.99
Manicouagan +	68.22	49.17	Neuse (Contentnea)	76.64	35.04
Outardes			Cape Fear	78.14	33.87

208 means that are adjusted such that daily-mean values temporally interpolated from them, when
209 summed over a month, results in the true monthly means) following Killworth (1996). Another
210 source of salt/freshwater flux at the sea surface is sea ice, which is a source of salt through brine
211 rejection at the time of freezing and a source of fresh water at the time of melting. Lateral
212 movement of sea ice results in these two surface fluxes occurring at different locations.

213 The sea ice model CICE consists of four main components: (a) a thermodynamic component that
214 calculates local growth or decay of sea ice due to snowfall and heat fluxes (Bitz and Lipscomb,
215 1999; Briegleb and Light, 2007); (b) a dynamic component that calculates the material properties
216 of the ice (Hunke and Dukowicz, 1997; Bouillon et al., 2013); (c) a transport component that
217 calculates the horizontal advection of the ice (Lipscomb and Hunke, 2004); and (d) a component
218 that calculates the distribution of ice among thickness categories due to ridging and mechanical
219 processes (Hunke et al., 2015). There are seven ice layers and five ice thickness categories. We
220 implemented the clamped boundary condition, in which GLORYS-derived values of sea ice
221 concentration (as a fraction of the model grid box area) and thickness are specified at the model's
222 lateral open boundaries. The sea ice specified at the lateral boundaries is uniformly covered with
223 snow of 0.2-m thickness. The time step in CICE is 1200 seconds.

224 Coupling between ROMS and CICE via MCT occurs every 1200 seconds, equivalent to every 10
225 internal time steps in ROMS and every time step in CICE. At each coupling step, ROMS sends
226 CICE the ERA5-derived atmospheric fields that drive both modules, as well as ROMS-simulated
227 values of currents, sea surface tilt, and sea-surface values of temperature and salinity. CICE
228 sends ROMS the ice-attenuated value of shortwave radiation and ice-ocean fluxes of stress, heat,
229 and salt or freshwater.

230 The BGC module includes the nitrogen cycle (Fennel et al., 2006), the carbonate system (Fennel
231 et al., 2008), and oxygen (Fennel et al., 2013). Particulate organic matter variables
232 (phytoplankton, zooplankton, and detritus) are split into small and large size classes, and rates of
233 biological processes are temperature-dependent (Laurent et al., 2021). The HSIMT advection
234 scheme (Wu and Zhu, 2010), which ensures no spurious negative values occur, is used for both
235 horizontal and vertical advection of BGC tracers. Initial and boundary conditions for nitrate,
236 phosphate, dissolved inorganic carbon, alkalinity, and oxygen are interpolated from the

237 climatology of GLODAP (Global Ocean Data Analysis Project; Lauvset et al., 2021) and set to a
238 small constant value for all other biogeochemical variables.

239 Four simulations will be examined in this paper. In the control simulation (hereafter Ctrl), the
240 ocean temperature and salinity at all grid points are nudged with a restoring time scale of 60 days
241 toward the monthly data set of in situ observations known as CORA (COriolis dataset for Re-
242 Analysis; Cabanes et al., 2013) above the 2000-m depth and GLORYS below 2000 m (where
243 CORA data are not available). The control simulation includes biogeochemistry. The second
244 simulation is a prognostic one (hereafter Prog), i.e., without any nudging of the simulation. There
245 are three reasons for presenting these simulations: 1) the ways in which either simulation
246 outperforms the other can shed light on potential ways in which the model can be improved; 2)
247 Ctrl, by including nudging of the temperature and salinity, produces a physical state of the ocean
248 that is generally realistic and acts as a foundation for the biogeochemical simulation; and 3) this
249 modelling system is being used in regional climate simulations (Renkl et al., in prep.), and the
250 lack of an option to nudge simulations of future conditions necessitates assessment of a
251 prognostic simulation. The performances of Ctrl and Prog will be evaluated in the next section.
252 Two more simulations are carried out for the sensitivity studies discussed in Sect. 4. Both are
253 identical to Prog but one is made without the specification of tidal elevation and currents at the
254 lateral boundaries (hereafter NoTides) and the other is made without coupling of ROMS to CICE
255 (hereafter NoIce). Configurations of the simulations are summarized in Table 2. All simulations
256 are made from 1 September 2013 to 31 December 2018 and are initialized with an ice-free ocean
257 in which the ocean's state consists of GLORYS fields for 1 September 2013 interpolated to the
258 model grid. The simulation results of January 2015 onwards (December 2014 onwards in the
259 case of seasonal averages) will be discussed in the following sections.

260 **Table 2.** Descriptions of the simulations discussed in this study.

Simulation name	Description	Temperature & salinity nudging	Tidal forcing at lateral boundaries	Coupling to sea ice model
Ctrl	Control	On	On	On
Prog	Prognostic	Off	On	On
NoTides	No tidal forcing	Off	Off	On
NoIce	No sea ice simulation	Off	On	Off

261 **3 Model results and evaluation**

262 **3.1 Simulated currents, temperature, and salinity**

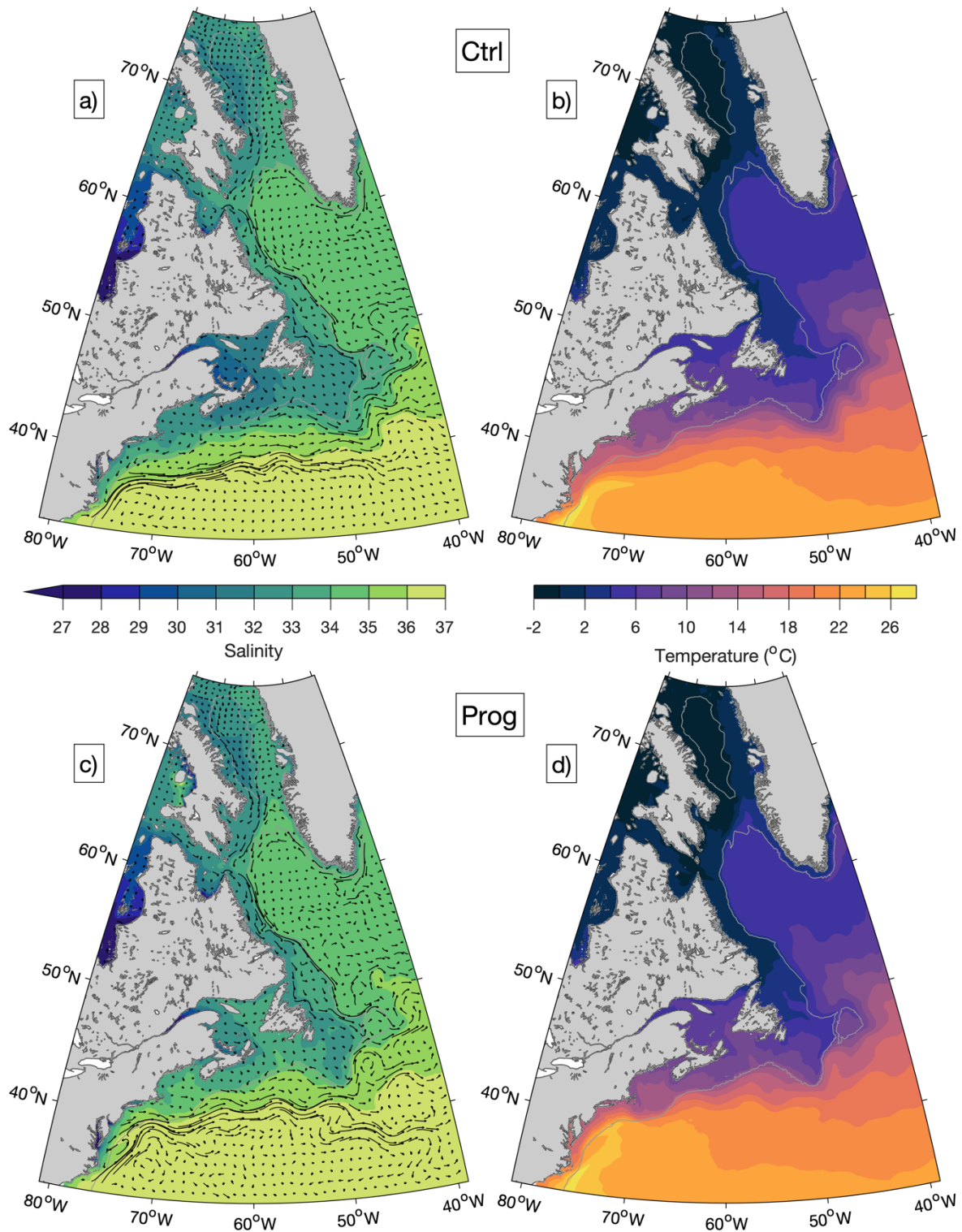
263 We first examine four-year (1 January 2015–31 December 2018) averages of currents, salinity,
 264 and temperature produced by DalROMS-NWA12 v1.0 in runs Ctrl and Prog (Figs. 2 and 3
 265 respectively). Both model runs reproduce the major features of the circulation in this region.
 266 They include: (a) the East and West Greenland Currents forming a clockwise flow around the
 267 southern tip of Greenland; (b) bifurcation of the West Greenland Current, with one branch
 268 continuing northward along the west coast of Greenland and the other flowing westward across
 269 the Labrador Sea; and (c) the westward flow across the Labrador Sea merging with the
 270 southward Baffin Island Current out of Baffin Bay and southeastward flow out of Hudson Strait
 271 to form the Labrador Current, the equatorward limb of the North Atlantic Subpolar Gyre. This
 272 current has branches along the Labrador coast and the shelf break. Near the Grand Banks, the
 273 Labrador Current meets the poleward Gulf Stream, the poleward limb of the North Atlantic
 274 Subtropical Gyre. Both simulations also reproduce the relatively cold and fresh water over
 275 continental shelves, with especially low values of salinity in Hudson Bay and the St. Lawrence
 276 Estuary. The three major differences between the simulations are that: (a) the bifurcation of the
 277 West Greenland Current has a stronger northward branch in Prog; (b) the Gulf Stream in Prog is
 278 closer to the continental shelf; and (c) the Gulf of St. Lawrence is warmer and saltier in Prog,
 279 both at the surface and in model results interpolated to the 100-m depth. As discussed below,
 280 comparison of model results to observations or reanalysis suggests the results of Ctrl are more
 281 realistic than those from Prog. Seasonal-means of these simulated fields, shown in Appendix B,
 282 indicate that differences between the simulations are more prominent in summer than in winter.

283 3.2 Model performance for currents, temperature, and salinity

284 To assess the model's performance in simulating currents, temperature, and salinity, we divide
285 the model domain into nine regions (Fig. 1b) and calculate metrics in each region for model
286 results at the sea surface and interpolated to the 100-m depth. Within a given region, each model
287 grid point is weighted by its horizontal area when regional averages are calculated. The areas
288 along the model's lateral boundaries in which the simulated tracers and currents are nudged
289 towards GLORYS are not included in the calculations.

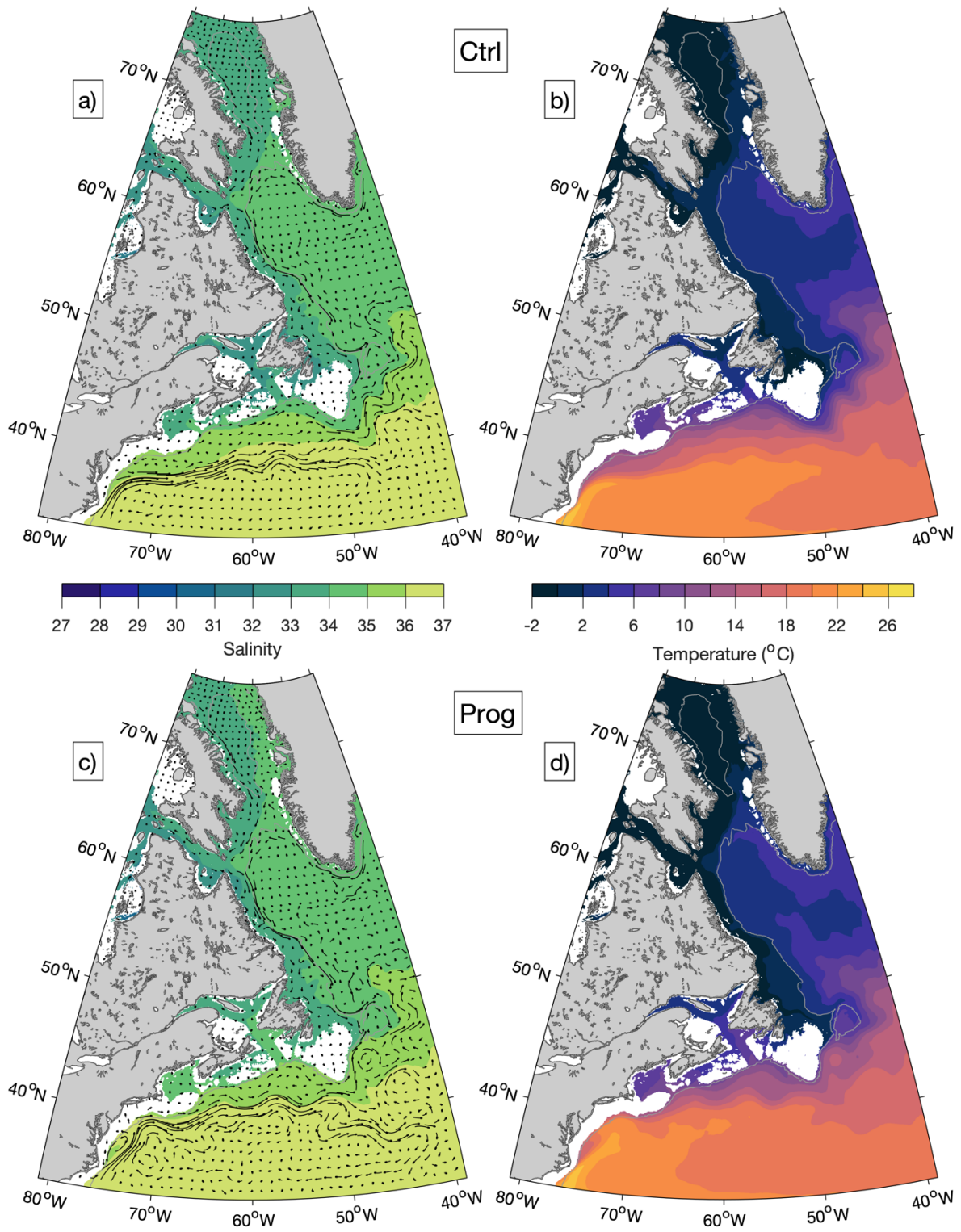
290 To quantify model performance for temperature and salinity at the sea surface, root-mean-square
291 errors (RMSE) of monthly-mean model results are calculated with respect to monthly means of
292 observations that are linearly interpolated to the model grid. Temperature and salinity at the
293 surface are compared to 1/4°-grid analysed data sets that combine satellite and in situ
294 observations: the daily data set OISST (Optimum Interpolation Sea Surface Temperature, v2.0
295 for 2015–2017 and v2.1 for 2018; Huang et al., 2021) for temperature and the weekly data set
296 SMOS (Soil Moisture Ocean Salinity; Buongiorno Nardelli et al., 2016) for salinity. For model
297 results interpolated to the 100-m depth, where gridded observational data sets are not available,
298 root-mean-square differences (RMSD) of temperature and salinity are calculated with respect to
299 their respective GLORYS values. It should be noted that GLORYS is based on simulations that
300 do not include tides (Lellouche et al., 2018), which may affect the accuracy of its temperature
301 and salinity distributions in addition to that of its currents, particularly over areas with strong
302 tidal currents. It should also be noted that the oceanographic observations used in generating
303 GLORYS are highly sparse in both time and space. As a result, data assimilation cannot
304 eliminate biases associated with the exclusion of tidal forcing in the monthly mean fields of
305 GLORYS.

306 The RMSE and RMSD of temperature from the two simulations (Figs. 4–5) are similar over the
307 northern part of the model domain in that the largest errors tend to occur at the surface in GRS
308 (Greenland Shelf) throughout the year, and in HST (Hudson Strait) and BB (Baffin Bay) during
309 the summer. Within these three areas, the largest values of RMSE/RMSD occur in HST at the
310 surface (about 3.5°C in Ctrl and 2.9°C in Prog, both in July). The corresponding biases of surface
311 temperatures (not shown) indicate a tendency for overestimation (+0.3°C–+2.2°C in GRS, and -
312 0.4°C–+1.9°C and -0.5°C–+1.0°C during summer in HST and BB respectively for Prog). Thus,



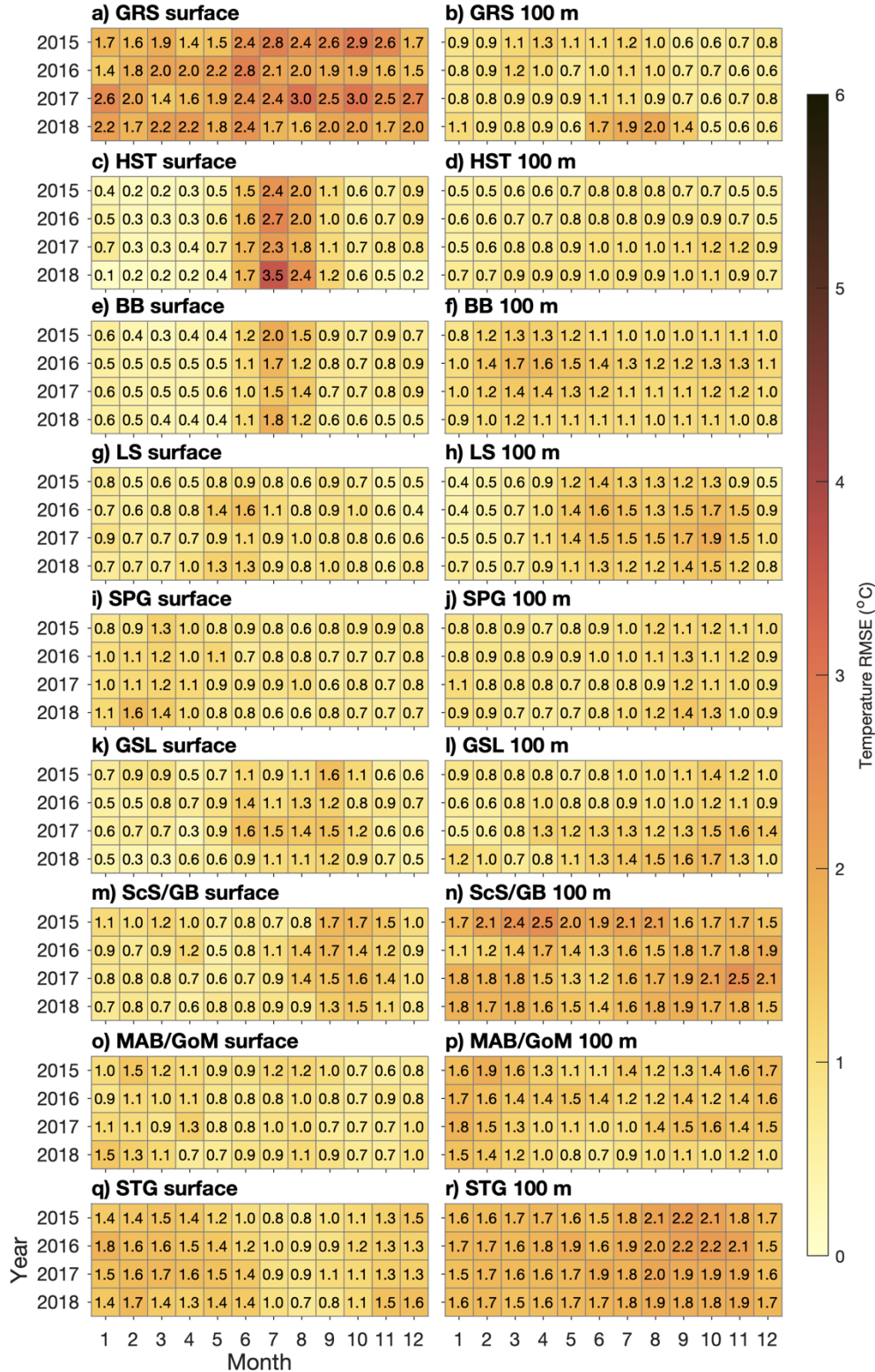
313
 314
 315
 316
 317
 318

Figure 2. Temporal-mean salinity (a, c) and temperature (b, d) at the sea surface, averaged over 2015–2018, from runs Ctrl (a, b) and Prog (c, d). Also shown in panels (a) and (c) are trajectories representing displacement over five days due to currents at the sea surface averaged over 2015–2018, shown at every 24 model grid points. The gray contour line represents the 1000-m water depth.



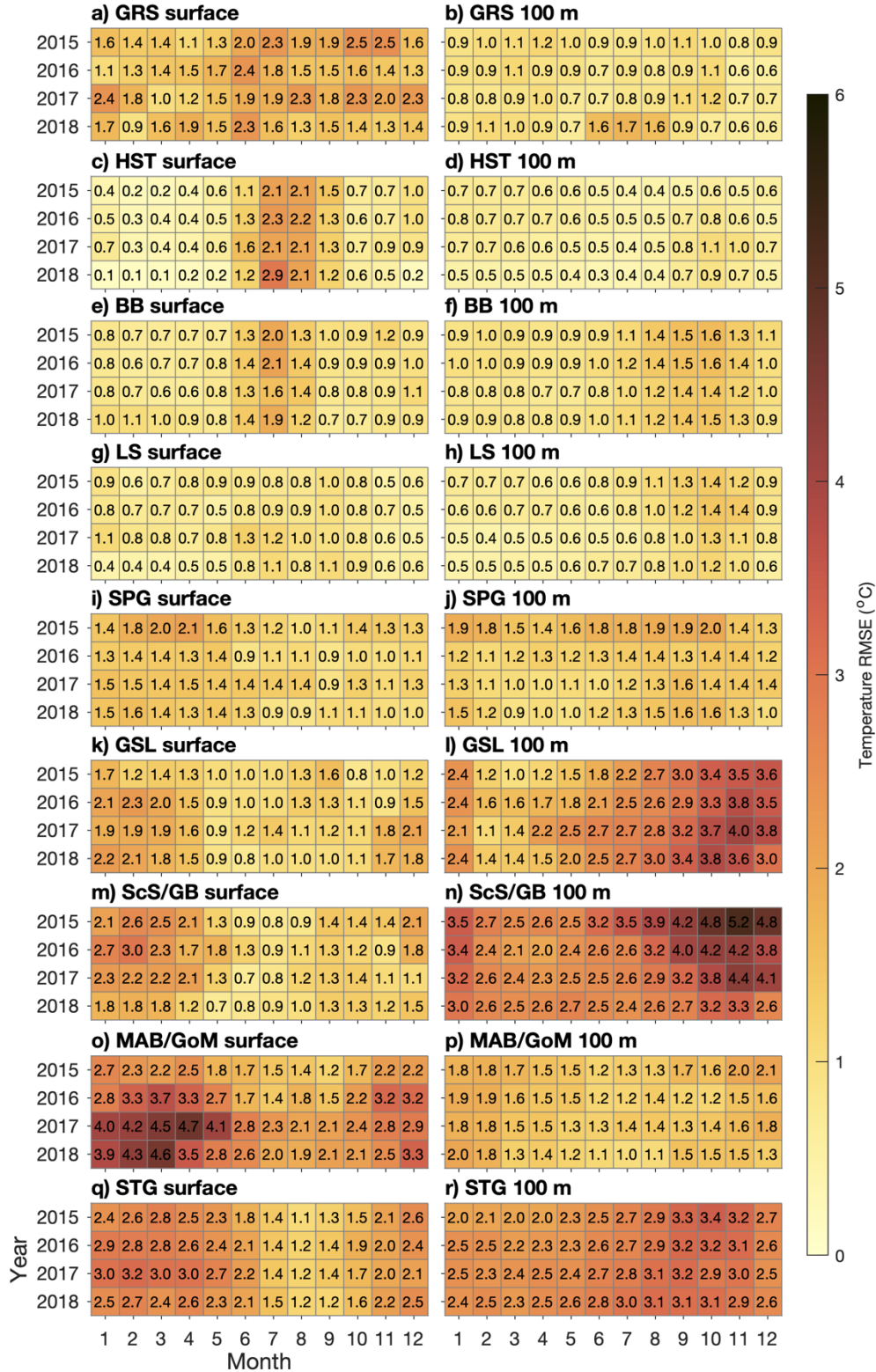
319
320
321

Figure 3. Similar to Fig. 2 but for model results interpolated to the 100-m depth.



322
323
324
325
326

Figure 4. Root-mean-square-errors/differences of temperatures (°C) simulated in Ctrl, calculated for the regions shown in Fig. 1b with respect to the observation-derived OISST data set at the surface and GLORYS reanalysis for model results interpolated to the 100-m depth.



327
328
329
330

Figure 5. Similar to Fig. 4 but for temperatures simulated in Prog.

331 the largest errors occur near the model's lateral open boundaries, during periods when sea ice
332 (which would tend to keep the temperature near freezing) is less in HST and BB, and at the
333 surface where the performance metrics are calculated with respect to an independent
334 observational data set instead of GLORYS which is also used as lateral boundary input. This
335 suggests GLORYS as a possible source of model errors, although a detailed examination is
336 beyond the scope of this study. The slightly larger RMSE of the simulated surface temperature in
337 Ctrl than in Prog over these areas may be related to the larger underestimation of sea ice in Ctrl,
338 which will be discussed in Sect. 3.3.

339 Further south, in SPG (Subpolar Gyre), the RMSE/RMSD are smaller in Ctrl than in Prog. The
340 RMSE at the surface has the range of 0.6–1.6°C in Ctrl and 0.9–2.1°C in Prog, and the RMSD for
341 model results interpolated to the 100-m depth has the range of 0.7–1.4°C in Ctrl and 0.9–2.0°C in
342 Prog. This suggests the West Greenland Current simulated in Ctrl, in which the branch of the
343 current that separates from the Greenland coast dominates, and its associated temperature
344 distribution are more realistic. The RMSE/RMSD in LS (Labrador Shelf) are similar between the
345 simulations, ranging from 0.4 to 1.9°C in Ctrl and from 0.4 to 1.4°C in Prog.

346 The results of Ctrl clearly outperform those of Prog over the southern part of the model domain,
347 with a maximum RMSE/RMSD of ~2.5°C in the former and ~5.2°C in the latter, both occurring
348 in ScS/GB (Scotian Shelf/Grand Banks) for model results interpolated to the 100-m depth. This
349 indicates the Gulf Stream simulated in Ctrl, flowing further from the coast than in Prog (Figs. 2–
350 3), is more realistic. In addition to STG (Subtropical Gyre) where the Gulf Stream itself flows,
351 the RMSE/RMSD in Ctrl are smaller both at the surface and the 100-m depth in ScS/GB,
352 MAB/GoM (Mid-Atlantic Bight/Gulf of Maine), and GSL (Gulf of St. Lawrence), all of which
353 are influenced by the warm and salty slope water of which the Gulf Stream water is one
354 component (Gatien, 1976). The influence of the slope water extending into the GSL at the 100-m
355 depth (which can also be seen in Fig. 3) is consistent with the observed (e.g., Richaud et al.,
356 2016) intrusion of slope water into the Gulf of St. Lawrence along the Laurentian Channel.

357 The RMSE and RMSD of salinity for both simulations (Figs. 6–7) in the northern part of the
358 domain are similar to those of temperature in that they tend to be largest at the surface in
359 summer, especially in HST where the RMSE has maximum values of ~2.7 psu in Ctrl and ~3.7

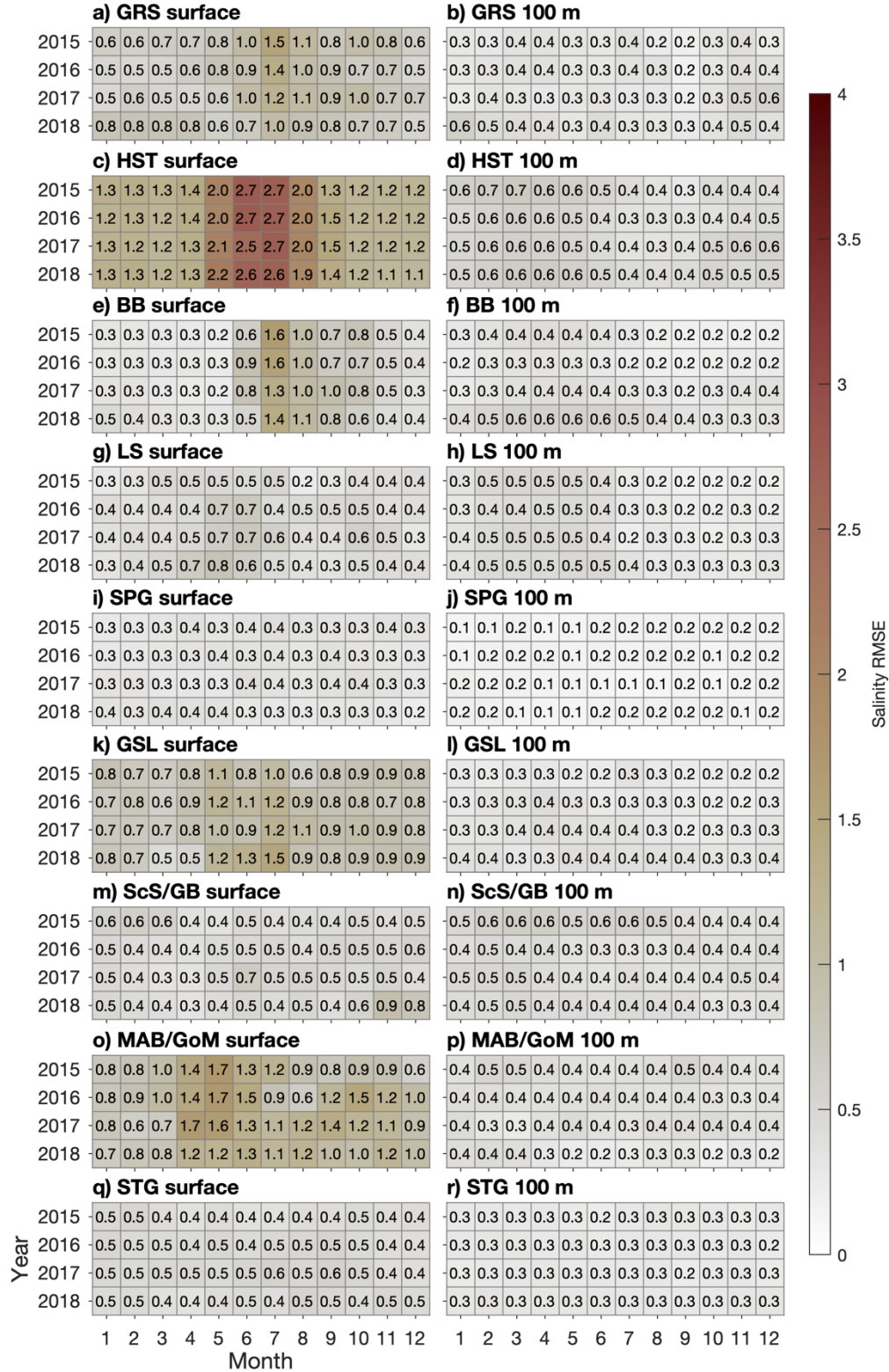
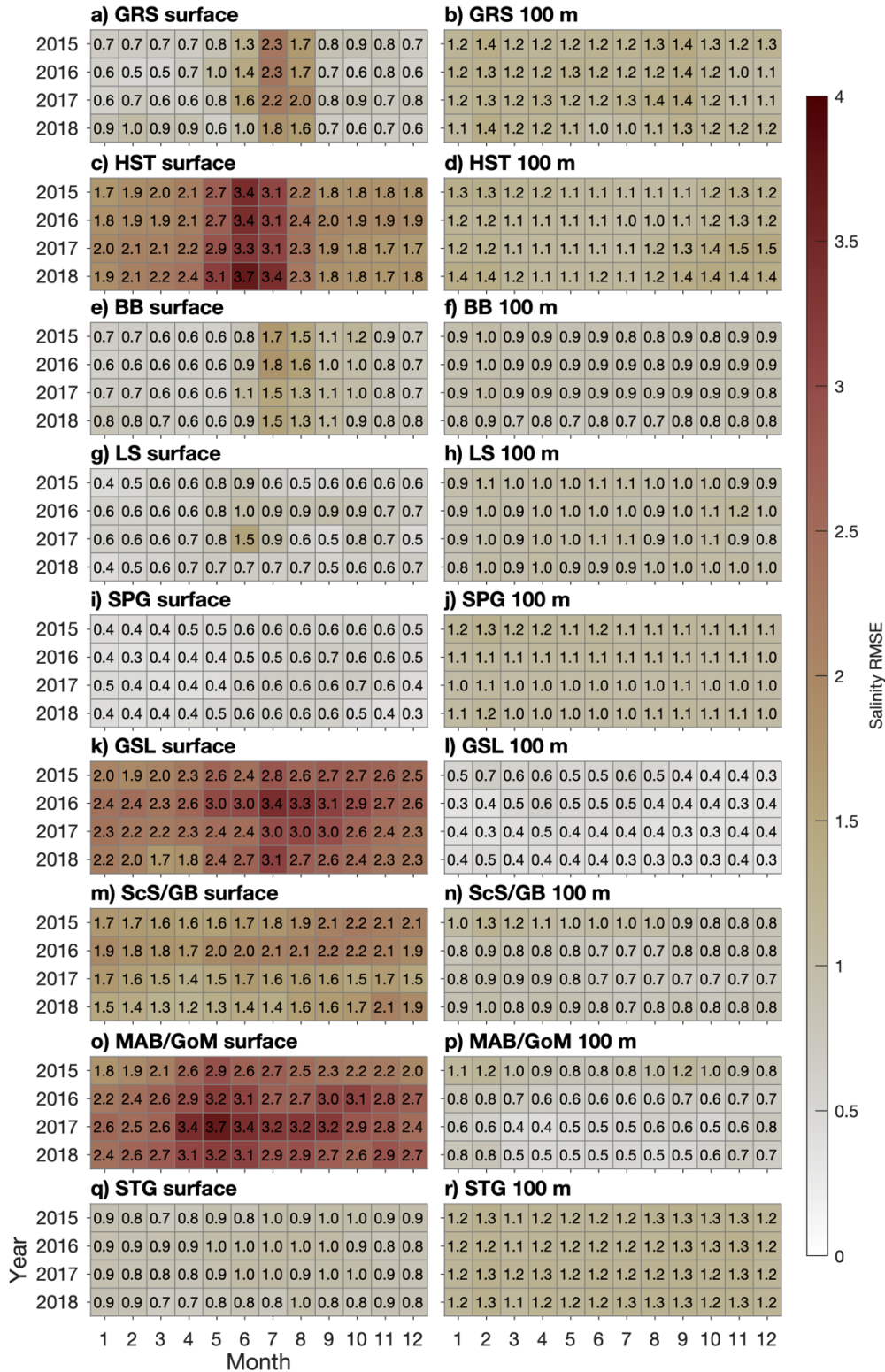


Figure 6. Root-mean-square-errors/differences of salinity (psu) simulated in Ctrl, calculated for the regions shown in Fig. 1b with respect to the observation-derived SMOS data set at the surface and GLORYS reanalysis for model results interpolated to the 100-m depth.



365
366
367
368

Figure 7. Similar to Figure 6 but for salinity simulated in Prog.

369 psu in Prog. In contrast to the temperature metrics, the surface salinity metrics in GRS undergo
370 an annual cycle similar to those in HST and BB, being larger during summer and fall than during
371 the rest of the year. During the months when the RMSE are largest, the surface salinity biases for
372 Prog are negative in GRS and BB (~ -1.0 psu) and positive in HST (up to $\sim +1.5$ psu). In SPG and
373 LS the RMSE/RMSD are generally smaller in Ctrl than in Prog (0.1–0.8 psu for Ctrl and 0.4–1.5
374 psu in Prog for the two regions combined), which is consistent with the metrics for temperatures
375 discussed above.

376 In the southern part of the domain, Ctrl has much smaller RMSE than Prog in GSL, ScS/GB, and
377 MAB/GoM (e.g., the maximum value is ~ 1.7 psu for Ctrl and ~ 3.7 psu for Prog in MAB/GoM).
378 The corresponding biases for Prog in these areas are consistently positive (up to $\sim +3.3$ psu in
379 GSL), indicating overestimation. However, within GSL, the 2015–2018 mean of summer surface
380 salinity simulated by Prog is lower than its counterpart from Ctrl by up to ~ 3.5 psu in the St.
381 Lawrence Estuary, but higher by ~ 2.0 psu further downstream in the Gulf of St. Lawrence (not
382 shown). This suggests the model is not able to fully reproduce the propagation of low-salinity
383 water from the St. Lawrence Estuary (where the salinity is underestimated) to areas downstream
384 of it (where the salinity is overestimated).

385 A possible cause of this discrepancy between observed and simulated salinity values in the St.
386 Lawrence Estuary-Gulf system is spurious diapycnal mixing generated by the third-order
387 upstream advection scheme used for tracers in this study (Marchesiello et al., 2009). We found
388 that switching to the fourth-order Akima scheme (with a horizontal eddy diffusivity of $5 \text{ m}^2 \text{ s}^{-1}$)
389 leads to more realistic simulations of three-dimensional salinity distributions and sea ice
390 distributions in the Gulf, but this option was not pursued further because the scheme is prone to
391 over- or under-shooting, which resulted in patches of unrealistic tracer values in areas such as the
392 Grand Banks where strong horizontal gradients occur. The same problem was reported by
393 Naughten et al. (2017) in simulating circulation in the Southern Ocean using ROMS and CICE.
394 A potential solution is a fourth-order advection scheme with a flux limiter to eliminate the
395 spurious over- and under-shooting, as demonstrated by Sheng (2002) for a z-level ocean model.

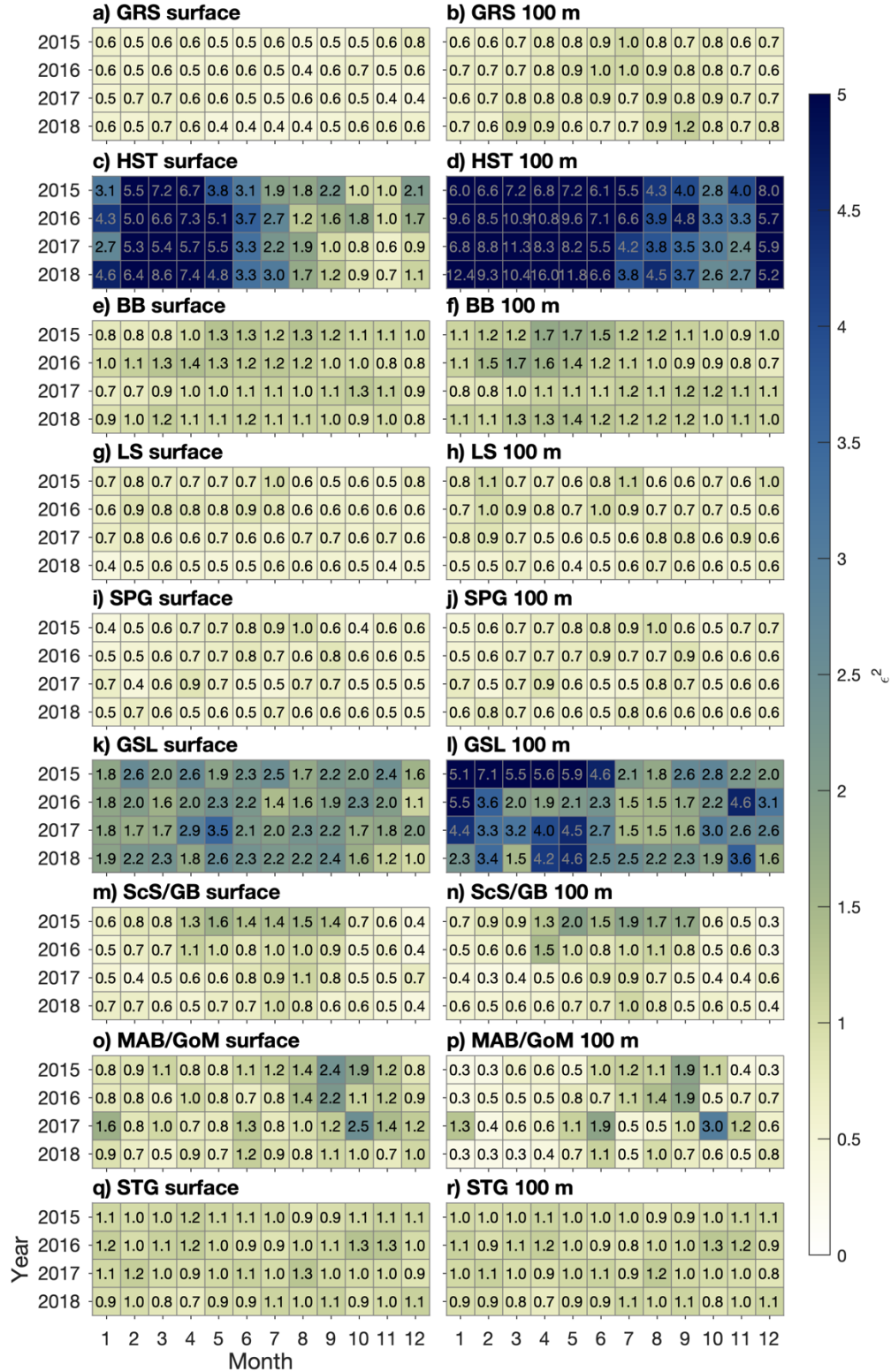
396 For currents, the model performance is evaluated using a metric known as ε^2 (Schwab et al.,
397 1989; Urrego-Blanco and Sheng, 2014):

$$\varepsilon^2 = \frac{\sum_{i=1}^N [(u_i^O - \bar{u}_i^O - u_i^M + \bar{u}_i^M)^2 + (v_i^O - \bar{v}_i^O - v_i^M + \bar{v}_i^M)^2]}{\sum_{i=1}^N [(u_i^O - \bar{u}_i^O)^2 + (v_i^O - \bar{v}_i^O)^2]}, \quad (1)$$

399 where the superscripts *O* and *M* denote observed and simulated values respectively, overbars
 400 denote spatial averaging over each validation region, and the summation is made over the
 401 validation region. Thus, this metric combines errors for the zonal and meridional current
 402 components and assesses model performance in terms of spatial averages as well as at individual
 403 points, with a value of zero corresponding to perfect agreement between model results and
 404 observations. The metric is calculated with respect to GLORYS both at the surface and for model
 405 results interpolated to the 100-m depth.

406 For both simulations, values of ε^2 (Figs. 8–9) in the southern part of the model domain are
 407 generally smaller in Ctrl than in Prog (e.g., about 0.7–1.3 for Ctrl vs. 1.0–2.2 for Prog in STG),
 408 consistent with the more realistic simulation of the Gulf Stream due to the nudging of salinity
 409 and temperature in Ctrl. In SPG and LS, values of ε^2 are similar between the regions and smaller
 410 in Ctrl than in Prog (about 0.4–1.1 in Ctrl and 0.5–1.6 in Prog for the two regions combined).
 411 This suggests the Labrador Current is more realistic in Ctrl than in Prog, which is consistent with
 412 the conclusion drawn from the temperature metrics that the separation of the West Greenland
 413 Current from the Greenland coast is simulated more accurately in Ctrl.

414 The model errors for both runs are largest in HST, mostly due to the southeastward flow along
 415 the south side of Hudson Strait being stronger in the model than in GLORYS (not shown).
 416 Taking as an example the 2015–2018 mean of monthly-mean currents produced by Prog in
 417 September, the southeastward flow is stronger than that in GLORYS by $\sim 0.25 \text{ m s}^{-1}$ at the surface
 418 and $\sim 0.15 \text{ m s}^{-1}$ at the 100-m depth. One possible reason for this large discrepancy is that the
 419 model is likely to be unable to accurately simulate the circulation in Hudson Bay, which is the
 420 source of the southeastward flow through Hudson Strait. Circulation in the Bay consists of
 421 several gyres and is sensitive to river discharge (Ridenour et al., 2019). Our model domain
 422 includes only the eastern part of the Bay (Fig. 1a) and, due to a lack of observations, we use
 423 climatological discharge (mostly calculated from observations in the 1960s or 1970s) for all but
 424 one of the ten rivers emptying into the eastern Bay; these factors cast doubt on the model’s
 425 ability to realistically simulate the flow within and out of the Bay.

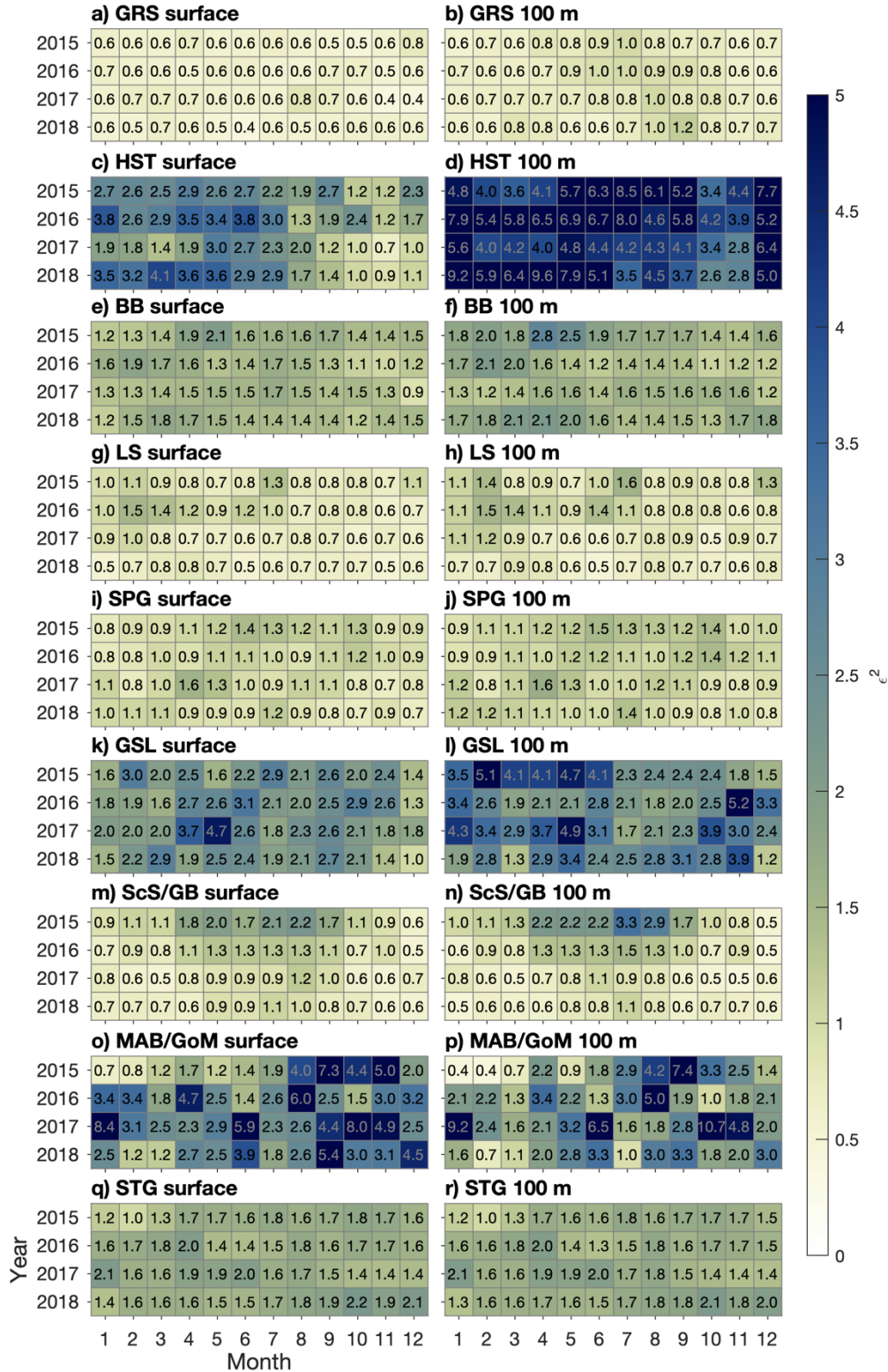


426

427

428 **Figure 8.** ϵ^2 of currents simulated in Ctrl, calculated for the regions shown in Fig. 1b with respect to GLORYS

429 reanalysis. See Equation 1 for the definition of ϵ^2 .



430
431
432
433

Figure 9. Similar to Fig. 8 but for currents simulated in Prog.

434 It should also be noted that Hudson Strait is characterized by tides of typically 3–6 m in
435 amplitude (Drinkwater, 1988). While our model includes tidal forcing, GLORYS, as stated
436 above, does not. This raises questions about how appropriate GLORYS is as a basis of evaluating
437 simulated currents in this area. Drinkwater (1988) deployed an array of current meters across
438 Hudson Strait between August and October of 1982. While exact coordinates of this array are not
439 available, the grid point in our model closest to the southwestern end of the array (station HS1)
440 can be approximated as (69.47° W, 61.15° N), with a water depth of 272 m, from Figs. 1–2 of
441 Drinkwater (1988). The eight-week average of residual current speeds at this location was
442 observed to be about 0.29 m s⁻¹ and 0.12 m s⁻¹ at the 30-m and 100-m depths respectively. The
443 2015–2018 average of September-mean current speeds simulated by Prog and from GLORYS at
444 the corresponding model grid point are similar to each other and somewhat less than the
445 observed value at the 30-m depth (about 0.24 m s⁻¹ and 0.23 m s⁻¹ respectively vs. 0.29 m s⁻¹).
446 However, at the 100-m depth, the simulated mean current speed (0.10 m s⁻¹) is more similar to
447 the observation (0.12 m s⁻¹) than the GLORYS value (0.03 m s⁻¹). Although we need to keep in
448 mind the existence of interannual variability and long-term trends which limit the conclusions we
449 can derive, these comparisons point to the possibility that the inclusion of tides in our model may
450 result in a more realistic vertical structure of currents in areas where both tides and baroclinity
451 play significant roles. The role of tides in the NWA is explored further in Sect. 4.1.

452 The temperature and salinity simulated in Prog have also been compared to observations made
453 along transects from the Atlantic Zone Monitoring Program and its off-shelf counterpart (not
454 shown). RMSE along the AR7W transect, which spans the Labrador Sea between southern
455 Labrador and southern Greenland, are largest near the surface, reaching ~2°C for temperature
456 and ~0.5 for salinity. The errors are larger in transects across Cabot Strait and across the Scotian
457 Shelf (up to ~4°C for temperature and ~3 for salinity), reflecting the difficulty Prog has in
458 reproducing the estuarine circulation in the Gulf of St. Lawrence and the positions of the Gulf
459 Stream and slope waters.

460 The preceding description and evaluation of the simulated circulation and hydrography have
461 highlighted two features in which the nudging of temperature and salinity in Ctrl leads to
462 improved model performance: (a) the separation of currents (the Gulf Stream and West
463 Greenland Current) from their respective coasts and (b) propagation of the low-salinity plume

464 from the St. Lawrence Estuary. Chassignet and Xu (2017) and Pennelly and Myers (2020)
465 showed respectively that increasing the horizontal resolution of their model grids from $1/12^\circ$ to
466 $1/50^\circ$ or $1/60^\circ$ resulted in more realistic representations of the Gulf Stream or the West Greenland
467 Current. Given the computational costs of making coupled physical-biogeochemical simulations
468 with a finer horizontal grid than what we currently use, a possible way to improve our modelling
469 system's performance in prognostic simulations would be to nest a finer-resolution grid covering
470 an area of particular interest (e.g., the Labrador Sea) within the existing $1/12^\circ$ grid. As discussed
471 earlier, a fourth-order horizontal advection scheme with a flux limiter is a possible way to
472 improve our model's simulation of estuarine plumes in prognostic simulations.

473 **3.3 Sea ice**

474 February-mean values of sea ice cover and effective sea ice thickness (sea ice cover multiplied
475 by thickness), averaged over 2015–2018, are shown in Fig. 10. Model results from Ctrl and Prog
476 are similar in that the ice cover spans Hudson Strait and adjoining areas to its west as well as
477 most of Baffin Bay, and the thickest ice (thickness $>\sim 3.0$ m) occurs along the coasts of those
478 areas. The two runs are different in that Ctrl produces more ice along the west coast of Greenland
479 and in the northwest Gulf of St. Lawrence, while Prog produces more ice along the north side of
480 Hudson Strait and on the Labrador Shelf. The larger sea ice production by Ctrl for the west coast
481 of Greenland and the northwest GSL is consistent with the lower sea-surface salinity and
482 temperature in this simulation due to the nudging (Fig. 2). For northern Hudson Strait and the
483 Labrador Shelf, a possible factor in the larger sea ice production by Prog is the fact that, in these
484 areas, offshore winds tend to cause ice divergence, which in turn leads to new ice formation
485 (Babb et al., 2021; Prinsenbergh and Peterson, 1992). The cycle of open water formation,
486 freezing, and ice divergence implies changes in the surface temperature and salinity over
487 relatively small spatiotemporal scales, which could be dampened by the nudging of Ctrl to the
488 monthly CORA data set which has a horizontal resolution of 0.2° – 0.5° in our study area
489 (Szekely, 2023). The role of sea ice on the physical oceanography of our study area is studied
490 further in Sect. 4.2.

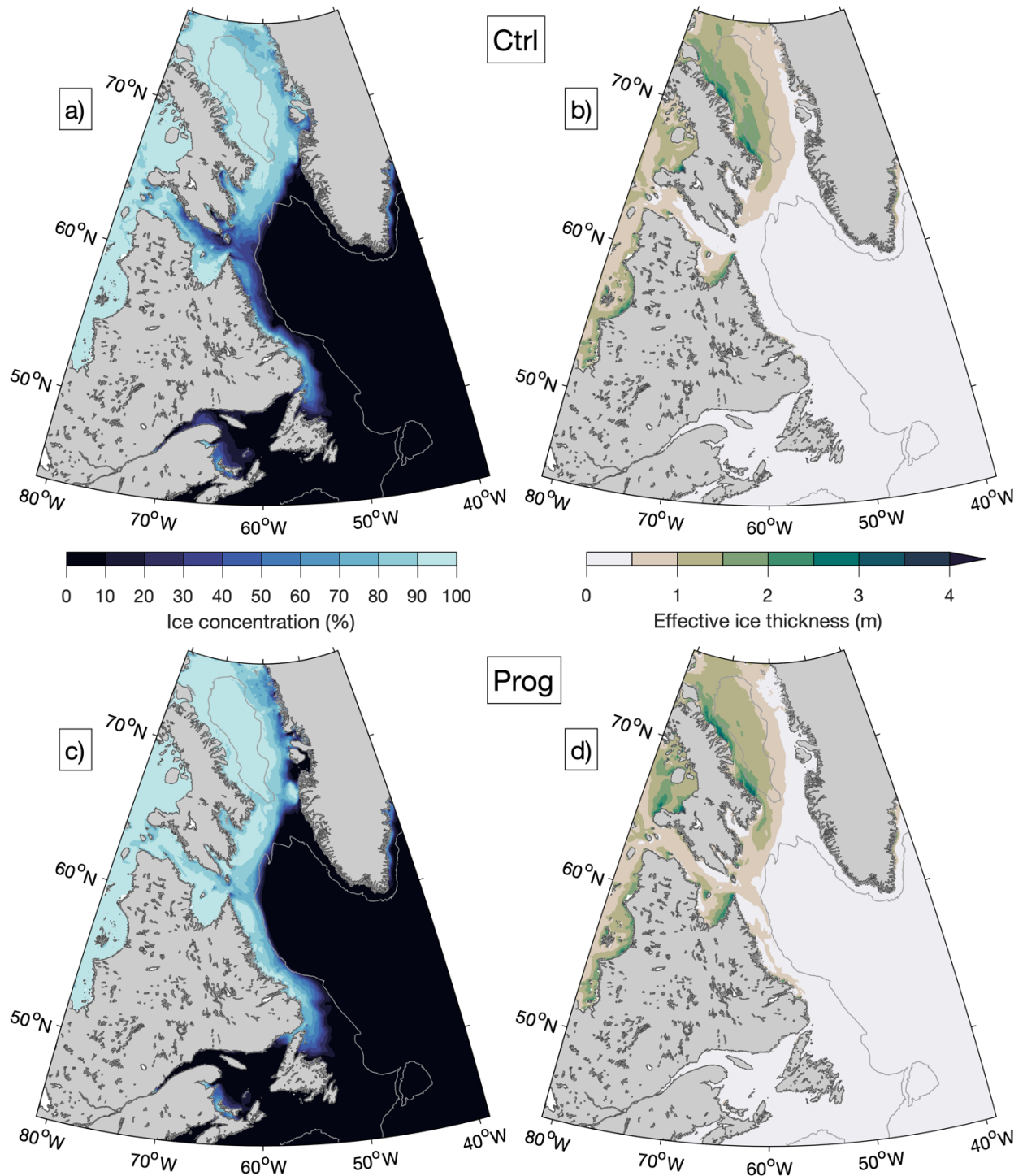
491 The ice model's performance is evaluated in terms of RMSE with respect to daily AMSR2
492 (Advanced Microwave Satellite Radiometer) observations, available on a 6.5-km grid

493 (Melsheimer and Spreen, 2019). The model errors in HST, BB, and LS are generally larger in
494 Ctrl (Fig. 11) than in Prog (Fig. 12), consistent with the smaller sea ice production in these areas
495 by the former. In HST, the increase in model error during May for both runs is mostly due to
496 underestimation, indicating a too-early melting of the ice. Given that this seasonal increase in
497 model error occurs in both runs, the cause of the underestimation may be related to ice advection
498 instead of thermodynamics. Examination of sea ice budgets for areas within the NWA is a
499 possible topic of future studies.

500 **3.4 Biogeochemistry**

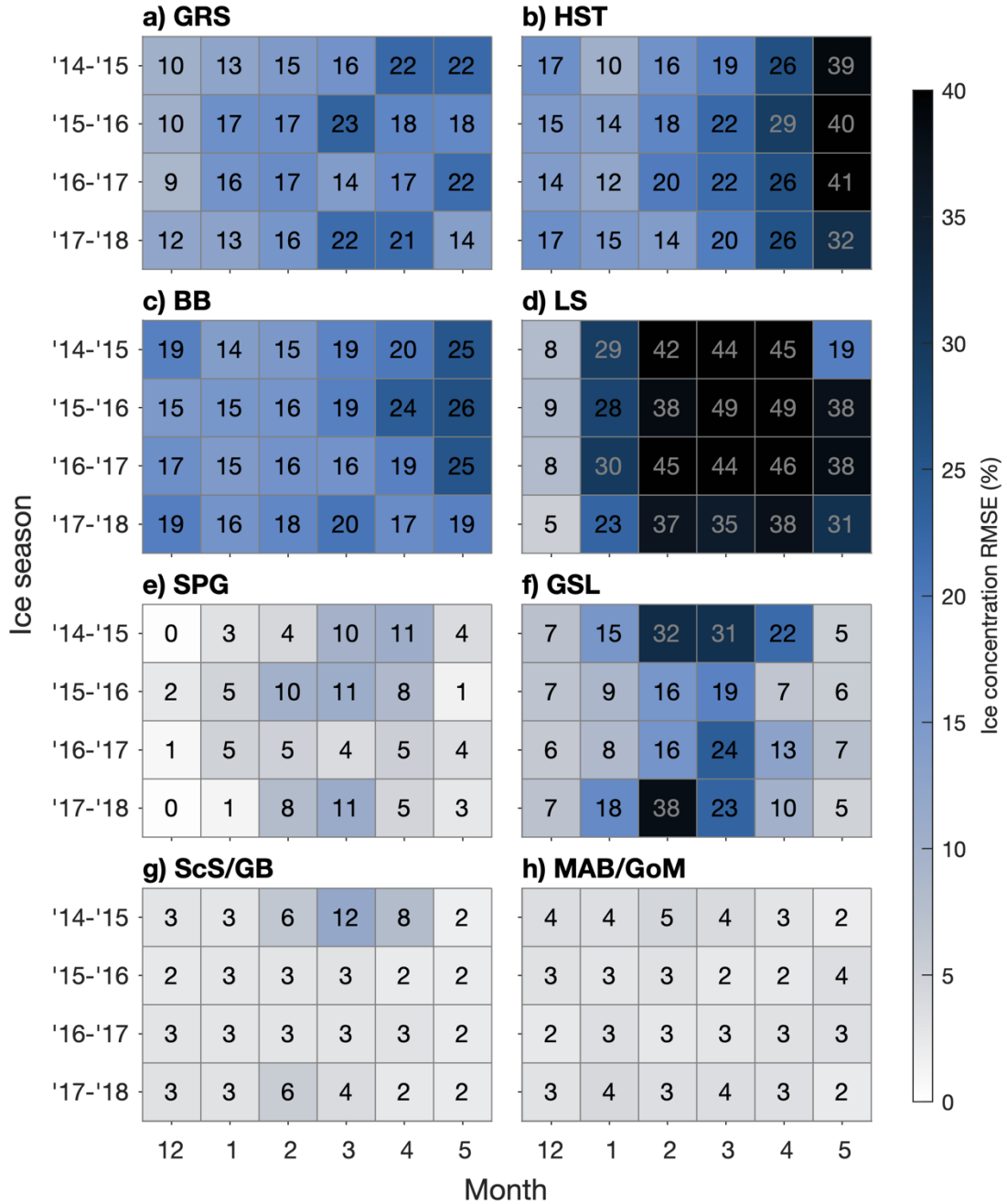
501 Snapshots of surface nitrate and subsurface oxygen in the Labrador Sea and surrounding areas at
502 the time of the Atlantic Zone Off-Shelf Monitoring Program (AZOMP) cruise in May 2015 are
503 shown in Fig. 13. The simulation indicates that nitrate starts to be depleted in the northern
504 Labrador Sea and along the Labrador shelf at this time but remains high in the deep central
505 Labrador Sea. Surface and shelf waters are well oxygenated and subsurface conditions along the
506 AR7W transect are characteristic of the water masses: oxygenated Labrador Sea Water
507 (depth < 2000 m), lower-oxygen Northeast Atlantic Deep Water (2000–3000 m), and the more
508 oxygenated Denmark Strait Overflow Water (>3000 m), which is in line with the observations
509 along the AR7W transect (Fig. 14a). Simulated nitrate is also characteristic of the three water
510 masses (Fig. 14b). As also shown in Fig. 13, surface nitrate remains high in the central Labrador
511 Sea but is low or depleted on the West Greenland and Labrador Shelves, respectively. These
512 patterns agree with the observations. The spatial variability in alkalinity (Fig. 14c) and total
513 inorganic carbon (TIC; Figure 14d) along the AR7W transect is also well represented. The largest
514 mismatch occurs for TIC which is underestimated in the subsurface layers (depths > 200 m).

515 Comparison of simulated oxygen, nitrate, alkalinity, and TIC to AZMP/AZOMP in situ
516 observations, at locations ranging from the Gulf of Maine to the Labrador Shelf, was carried out
517 for the period 2014–2018 (Fig. 15). The model simulates reasonably well the spatial and
518 temporal variability in biogeochemical variables ($0.65 < r^2 < 0.81$). Simulated oxygen has a small
519 positive bias (10.8 mmol m^{-3} , Fig. 15a) but otherwise agrees with observations. Nitrate has the
520 best match with observations ($r^2 = 0.81$) but with a small positive bias (Fig. 15b), possibly driven
521 by excess vertical mixing or by a delay in the seasonal uptake. The small bias at low TIC (i.e.,
522 surface) is likely to have the same source (Fig. 15d).



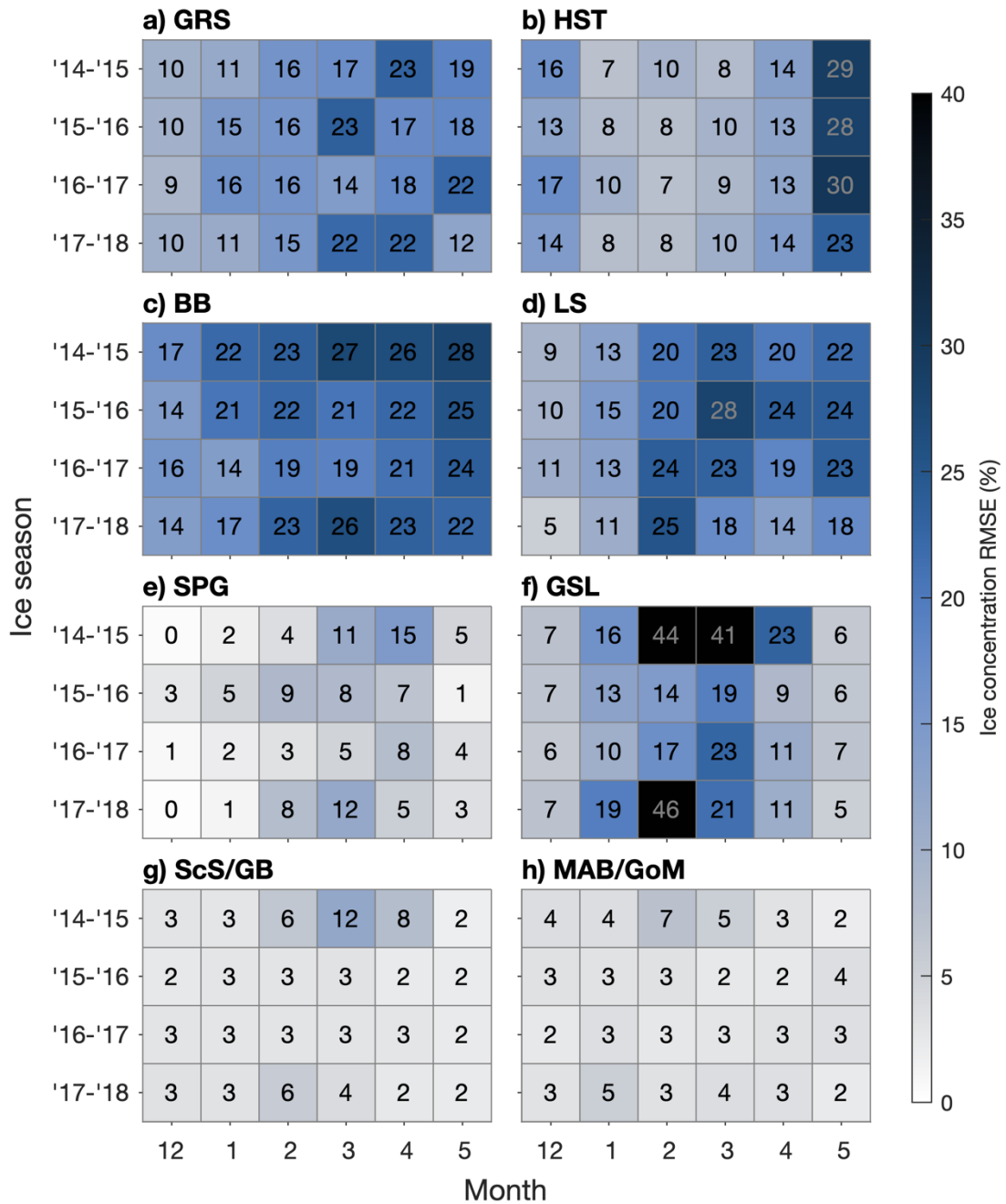
523
 524
 525
 526
 527
 528

Figure 10. Monthly-mean simulated sea ice concentration (a, c) and effective sea ice thickness (sea ice cover multiplied by thickness) (b, d) for February, averaged over 2015–2018, from Ctrl (a, b) and Prog (c, d). The gray contour line represents the 1000-m water depth.



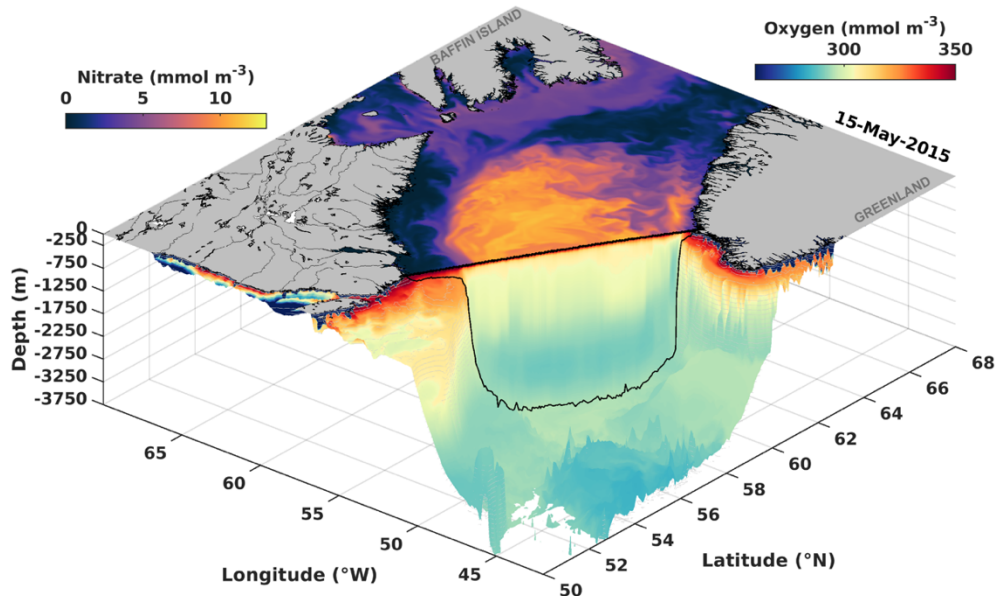
529
530
531
532

Figure 11. Root-mean-square-errors of ice concentration simulated in Ctrl, calculated for the regions shown in Fig. 1b with respect to AMSR2 satellite observations.

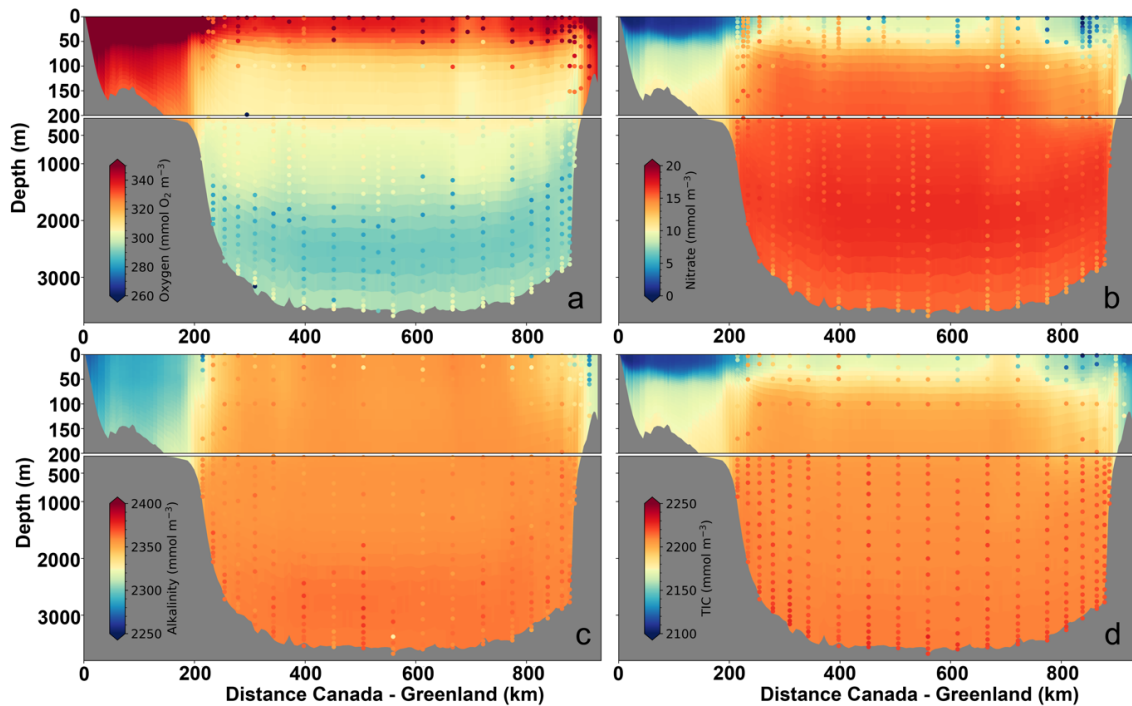


533
534
535
536

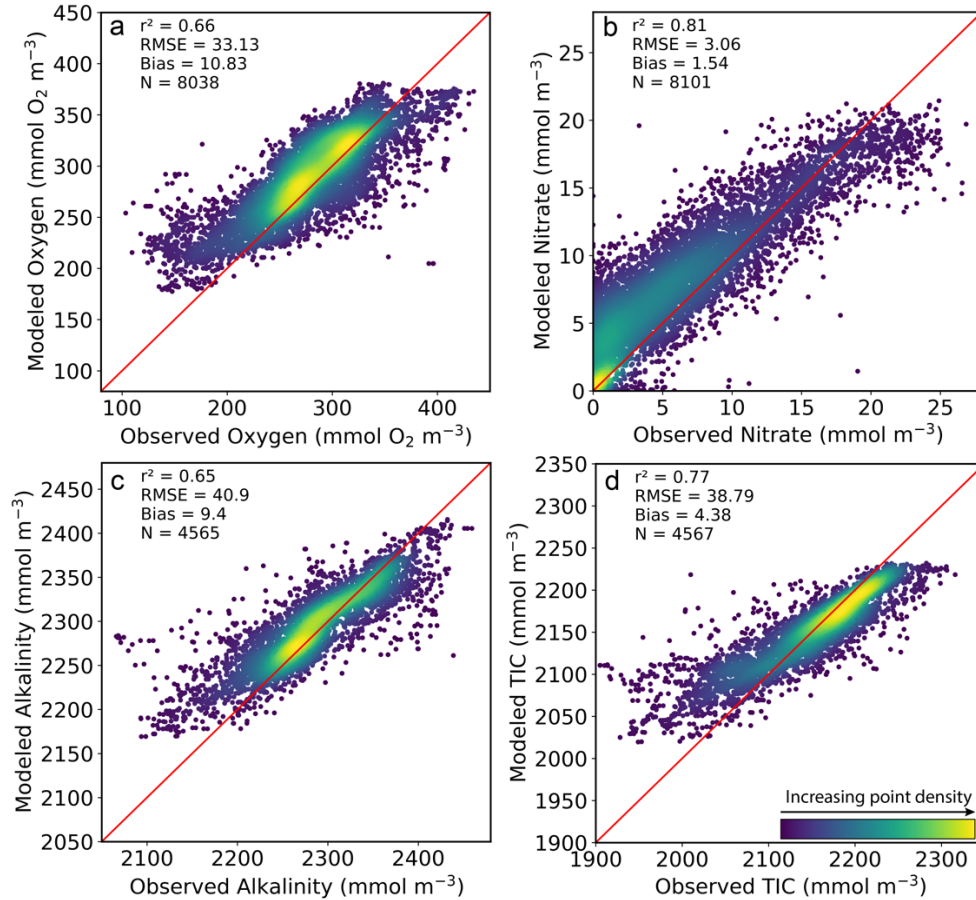
Figure 12. Similar to Fig. 11 but for ice concentration simulated in Prog.



537
 538
 539 **Figure 13.** Three-dimensional view of simulated surface nitrate and subsurface oxygen for May 15, 2015. The thick
 540 black line at the sea surface denotes the position of the AR7W transect, and the thin black line represents the model's
 541 bottom topography along the transect.
 542



543
 544
 545 **Figure 14.** Comparison of simulated (background) versus observed (dots) for: oxygen (a), nitrate (b), alkalinity (c),
 546 and total inorganic carbon (d) during the AR7W transect in May 2015. Note: the y-axis has higher resolution in the
 547 upper 200 m.



548
549
550
551
552
553

Figure 15. Comparison between simulated values and AZMP/AZOMP bottle observations during 2014–2018 for: oxygen (a), nitrate (b), alkalinity (c), and total inorganic carbon (d). N is the number of observations used for the comparison.

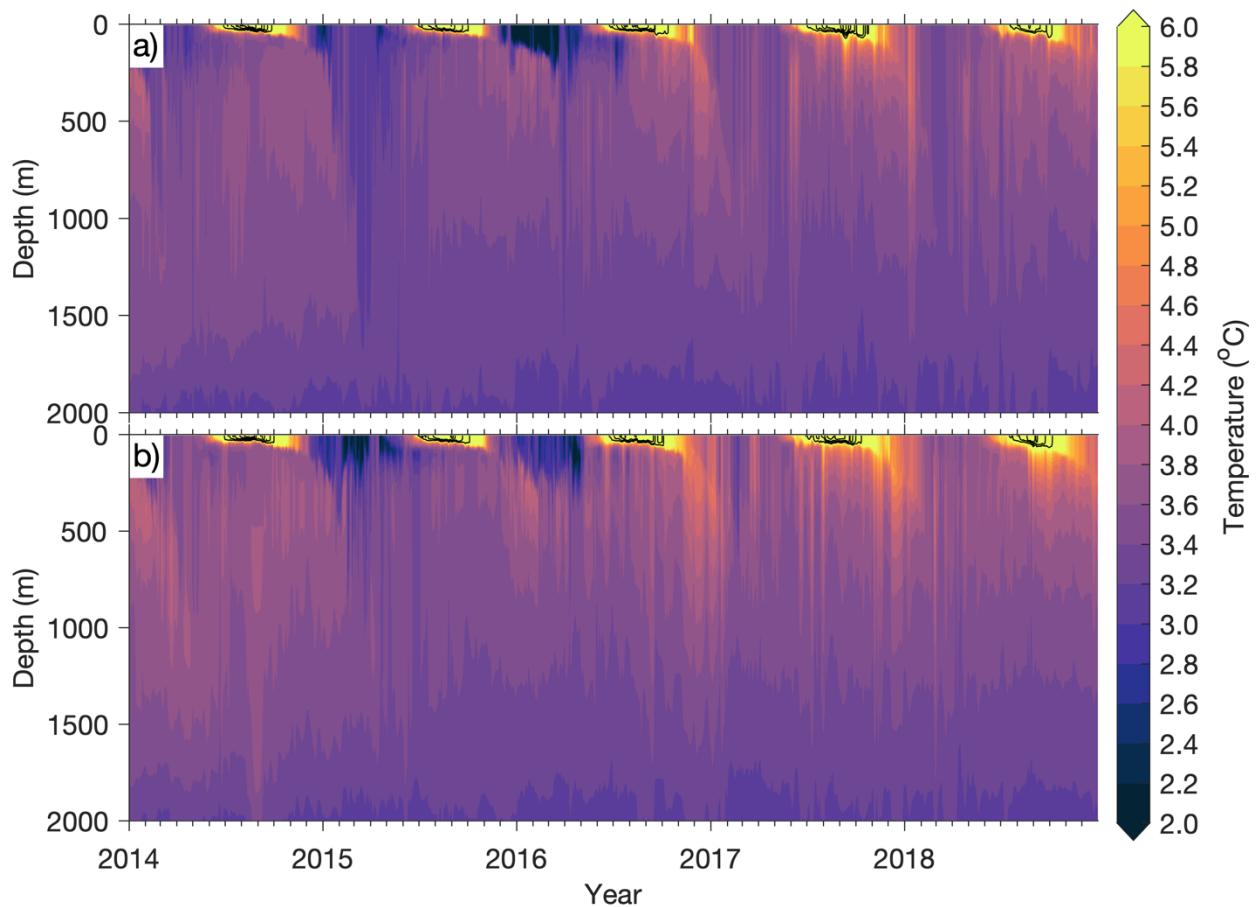
554 3.5 Simulation of deep convection in the Labrador Sea

555 One of the important hydrodynamic features of the NWA is the occurrence of deep winter
556 convection (DWC) in the Labrador Sea and a few other areas. DWC ventilates the deep ocean,
557 contributes to the removal of anthropogenic carbon from near-surface waters, and is thought to
558 influence the larger-scale Atlantic Meridional Overturning Circulation (e.g., Rhein et al., 2011).
559 In this section, we assess the model performance in reproducing the effects of DWC at two
560 locations (indicated by numbers in Fig. 1): location 1 (54.31° W, 58.29° N) which is near the
561 centre of the “convective region” identified by Luo et al. (2014), and location 2 (50.72° W,
562 58.29° N) which is on the AR7W transect and is within the area (“Central Labrador Sea”) for

563 which Yashayaev (2024, hereafter Y24) composited the available observations to form time
564 series of ocean properties from the surface to the 2000-m depth. (Location 1 is near the western
565 edge of the Central Labrador Sea as defined by Y24.) The output of Prog will be used here so
566 that the model's response to the conditions that trigger DWC can be assessed. Because the time
567 series of Y24 indicated that conditions in 2014 were markedly different from those of subsequent
568 years, the model results of 2014 will be included here even though they were excluded from the
569 preceding discussions of model performance.

570 Time series of temperature profiles at the two locations are shown in Fig. 16. The time series at
571 location 1 is generally more similar to the observation-based, area-composite time series of Y24
572 (his Fig. 3) than at location 2. This is consistent with the fact that location 1 is at the centre of the
573 area where DWC occurred in the modelling study of Luo et al. (2014), which they found to agree
574 with areas of convection observed by, e.g., Lavender et al. (2000). The time series of simulated
575 temperature profiles at location 1 includes several features that appear in Y24, such as: 1) the
576 turbulent vertical mixing/convection being much stronger in 2015 than in 2014, with the 3.4°C
577 contour of simulated temperatures extending down to the ~1600-m depth in 2015 but just to the
578 ~1000-m depth in 2014; 2) temperatures below 3°C occurring from the surface to the ~200-m
579 depth from late 2015 to early 2016; and 3) temperatures above 6°C extending to a maximum of
580 ~100 m below the surface during the summer. Given that: 1) our model does not directly
581 simulate or parameterize deep convection and 2) we are comparing the temporal evolution of
582 simulated temperatures at one location against a composite of observations over an area with a
583 diameter of $O(100\text{ km})$ in Y24, we find these similarities encouraging.

584 It should be noted that the horizontal grid size of our model is $O(1\text{ km})$, which is much coarser
585 than the typical horizontal scale of $O(100\text{ m})$ for the convective plumes (e.g., The Lab Sea
586 Group, 1998). Furthermore, our circulation model does not use an explicit winter advection
587 scheme, instead it uses large vertical mixing coefficients produced by the modified "2.5-level"
588 scheme of Mellor and Yamada (1982) to mimic the intense convective mixing associated with
589 DWC. A fine-resolution model with a horizontal grid size of $O(100\text{ m})$ nested within
590 DALROMS-NWA12 v1.0 will be used in our future research to develop better parameterizations
591 of DWC over the NWA and to examine how the model simulates deep ocean ventilation and
592 near-surface carbon removal due to DWC.



593

594 **Figure 16.** Daily-mean simulated temperatures from Prog, vertically interpolated to 5-m depth intervals between the
 595 0- and 2000-m depths, at location 1 (54.31° W, 58.29° N) **(a)** and location 2 (50.72° W, 58.29° N) **(b)**, indicated as
 596 “1” and “2” respectively in Fig. 1. Major tick marks correspond to 1 January of each year and minor tick marks
 597 correspond to the first days of February–November. Temperature values between 6°C and 11°C are shown with
 598 black contour lines at 1°C intervals.

599

600 **4 Sensitivity studies**

601 The ocean circulation and sea ice modules of DalROMS-NWA12 v1.0 are used in this section to
 602 examine the roles of tides and sea ice in the hydrodynamics of the NWA. This is done by
 603 comparing the model results from Prog to those from two additional simulations that are
 604 identical to Prog but with the tidal forcing absent from one (NoTides) and sea ice absent from the
 605 other (NoIce). In NoIce, the net surface heat flux is set to zero if it would cool the ocean and the
 606 sea surface temperature is already at or below the local freezing temperature. The difference

607 between surface temperatures simulated in Prog and in NoTides (Prog minus NoTides) will be
 608 denoted ΔT_{sfc}^{P-NT} and the difference in bottom temperatures will be denoted ΔT_{btm}^{P-NT} . Similar
 609 notations will be used for differences in salinity (e.g., ΔS_{sfc}^{P-NT}) and current speed (e.g.,
 610 $\Delta |\vec{V}|_{sfc}^{P-NT}$) and for differences between model results from Prog and NoIce (e.g., ΔT_{sfc}^{P-NI}).

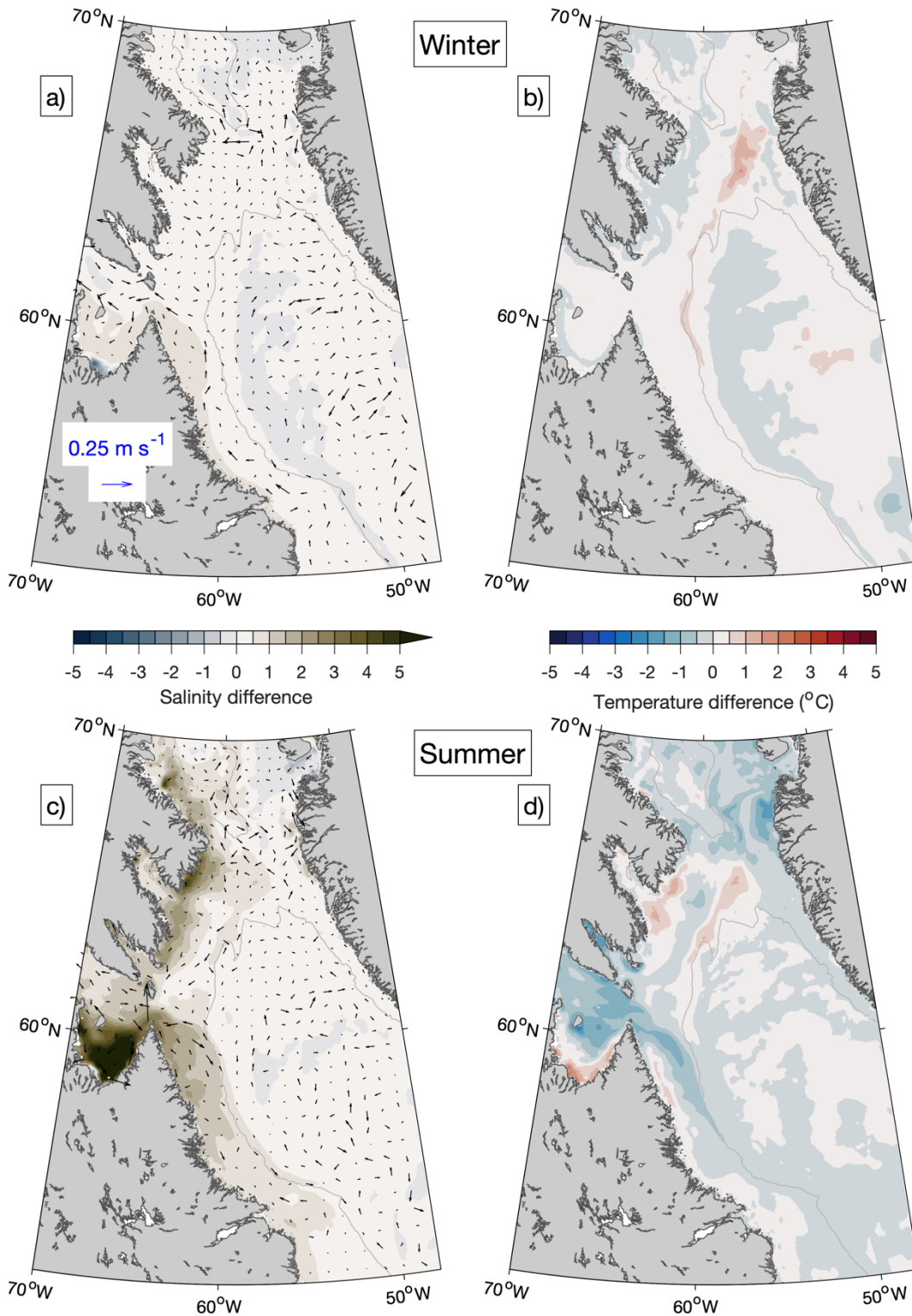
611 4.1 The effect of tides

612 Differences between Prog and NoTides (Prog minus NoTides) in sea surface salinity, currents,
 613 and temperature over Baffin Bay and the Labrador Sea, averaged over the winters (December–
 614 February) and summers (June–August) of December 2014–August 2018, are shown in Fig. 17. In
 615 winter (Fig. 17a–b), differences between the simulations of temperature and salinity over this
 616 area are relatively small – generally within ± 1 for salinity, and up to $\sim +1.5^\circ\text{C}$ for temperature. In
 617 summer (Fig. 17c–d), ΔS_{sfc}^{P-NT} is positive along most of the Baffin Island coast, in Ungava Bay,
 618 and on the northern Labrador Shelf (up to ~ 7 in Ungava Bay) while ΔT_{sfc}^{P-NT} is mostly negative
 619 throughout the area but especially over shelves ($\sim -1.0^\circ\text{C}$). These differences between Prog and
 620 NoTides are consistent with the presence of sea ice over large portions of this area during winter,
 621 given that sea ice can modulate tidal mixing and thus tend to reduce the differences between the
 622 ocean states simulated with and without tides. In summer, the presence of tidal mixing in Prog
 623 contributes to vertical mixing over shelf areas, resulting in surface waters that are saltier and
 624 colder than if there were no tides and the water column were more highly stratified. There are,
 625 however, areas in which the inclusion of tides results in positive ΔT_{sfc}^{P-NT} during the summer,
 626 notably along the coast of Ungava Bay. Given that ΔS_{sfc}^{P-NT} is positive throughout the Bay, the
 627 contrast between positive ΔT_{sfc}^{P-NT} along the coast and negative ΔT_{sfc}^{P-NT} near the Bay’s mouth
 628 suggests air-sea fluxes might differ between the two parts of the Bay.

629 The effect of tides on water temperature within Ungava Bay is explored in Figs. 18 and 19. In
 630 winter, the models results from Prog and NoTides are similar not only in terms of the surface
 631 temperature (Fig. 18a), but also in terms of bottom temperature ($|\Delta T_{btm}^{P-NT}| < \sim 1.0^\circ\text{C}$, Fig. 18b)
 632 and current speeds at both the surface and bottom ($\Delta |\vec{V}|_{sfc}^{P-NT}$ and $\Delta |\vec{V}|_{btm}^{P-NT} < \sim 0.1 \text{ m s}^{-1}$, Fig.
 633 18a–b). In summer at the sea surface (Fig. 18c), both $\Delta |\vec{V}|_{sfc}^{P-NT}$ and ΔT_{sfc}^{P-NT} are positive along

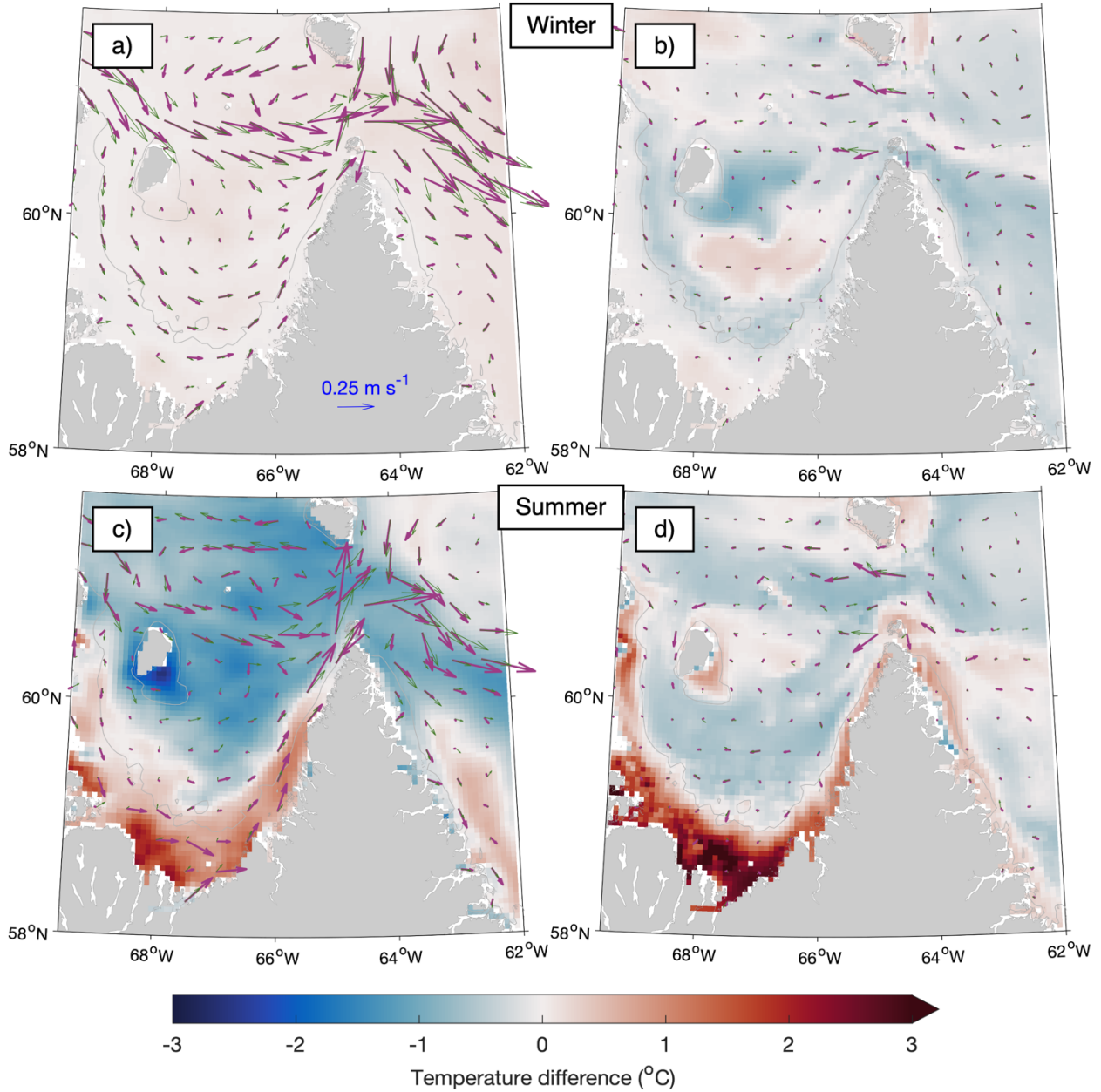
634 the coast but generally negative in the outer bay. Along the bottom in summer (Fig. 18d),
635 ΔT_{btm}^{P-NT} is positive and as large as $\sim +4^\circ\text{C}$ along the coast, while in the outer bay ΔT_{btm}^{P-NT} is small
636 ($|\Delta T_{btm}^{P-NT}| < \sim 1.0^\circ\text{C}$) and the currents are generally weak in both simulations. The patterns of
637 mean summer sea ice concentration are also different between the two simulations, with the ice
638 cover produced in Prog (Fig. 19a) being highest over the outer bay (up to $\sim 40\%$) and low near
639 the coast, while NoTides (Fig. 19b) produces a wide area of high ice cover along the coast (up to
640 $\sim 90\%$). The patterns of mean summer sea surface temperature from the two simulations (Fig.
641 19c–d) correspond to those of the sea ice cover, with areas of higher (lower) ice cover
642 corresponding to lower (higher) temperatures. Given that the only difference between the Prog
643 and NoTides simulations is the inclusion of tides in the former, these results suggest that tides
644 along the coast of Ungava Bay promotes an earlier disappearance of ice there during the summer,
645 and this in turn leads to a larger flux of solar radiation into the ocean and a less impeded flow.

646 The effect of tides is also evident in the region surrounding two other areas with large tidal
647 ranges, the St. Lawrence Estuary and the Bay of Fundy. In both winter and summer, ΔS_{sfc}^{P-NT} in
648 the St. Lawrence Estuary (Fig. 20a,c) is positive (up to ~ 6.0 in most of the Estuary but > 10 in
649 parts of the Upper Estuary during the summer), suggesting that tidal mixing brings higher-
650 salinity subsurface water towards the surface. In summer (Fig. 20c), the influence of this higher
651 salinity due to tidal mixing spreads into the northwest Gulf of St. Lawrence due to the
652 propagation of the estuarine plume. In the Bay of Fundy, the salinity difference is also positive in
653 both seasons. In winter, ΔS_{sfc}^{P-NT} ranges from ~ 0.4 in most of the Bay to ~ 2.4 near the Saint John
654 River's mouth and in summer, it ranges from ~ 1.2 in the upper Bay to ~ 3.6 near the Saint John
655 River's mouth. The role of tidal mixing is also evident in the patterns of sea surface temperatures
656 (Fig. 20b,d), with ΔT_{sfc}^{P-NT} positive in winter (up to $\sim 1.5^\circ\text{C}$ in both the St. Lawrence Estuary and
657 the Bay of Fundy) and negative in summer (as low as $\sim -4.5^\circ\text{C}$ in both areas). Differences
658 between the simulations are also visible over the open ocean for all three fields. As Wang et al.
659 (2020) have suggested, this may be caused by internal tides that are generated near the shelf
660 break and propagate offshore.



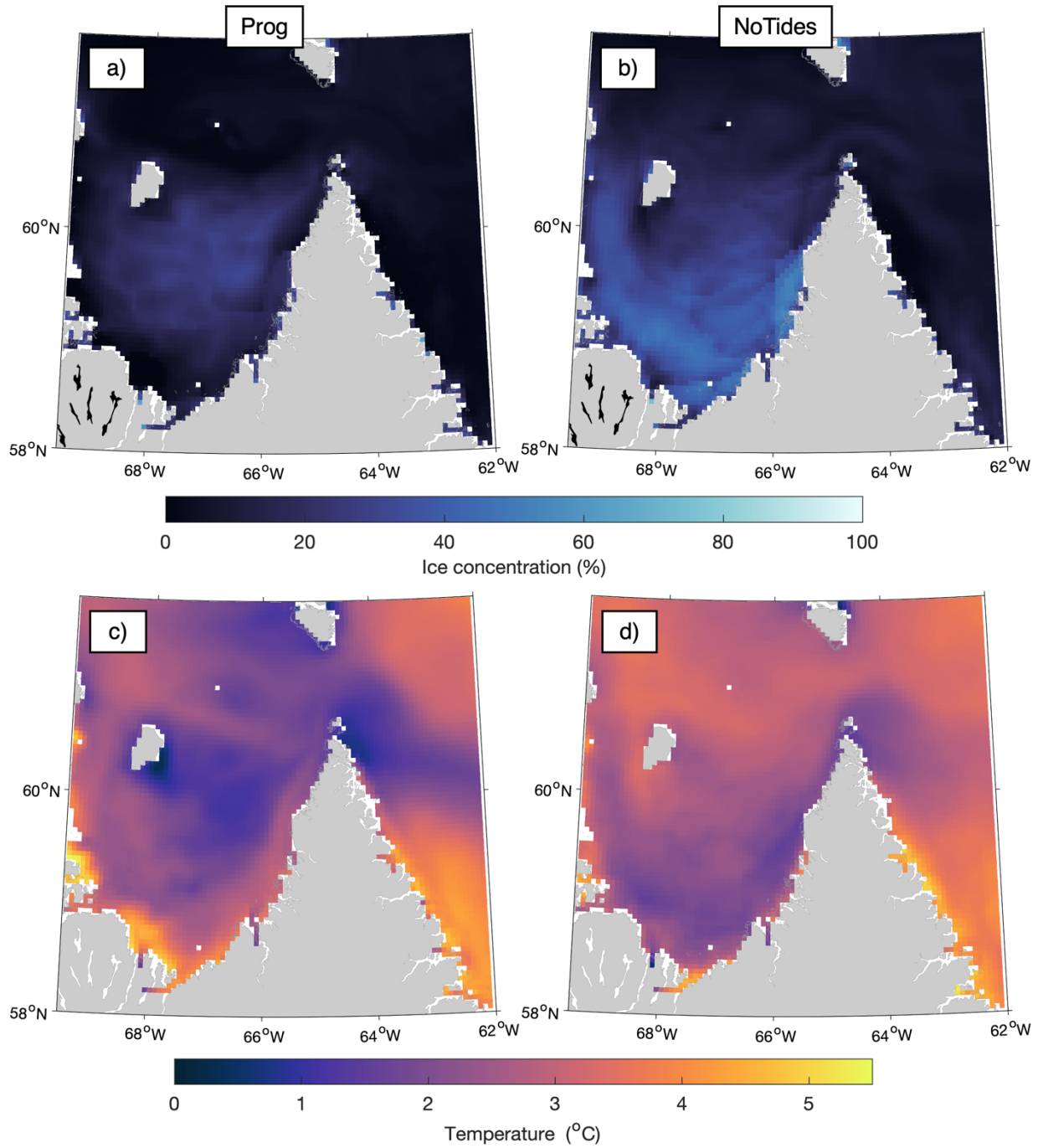
661
 662
 663
 664
 665
 666

Figure 17. Differences in seasonal-mean simulated sea surface salinity and currents (a, c) and temperature (b, d) over Baffin Bay and the Labrador Sea when model results from NoTides are subtracted from those from Prog, averaged over winters (a, b) and summers (c, d) of 2015–2018. Difference vectors are shown at every 12th model grid point. The gray contour line represents the 1000-m water depth.



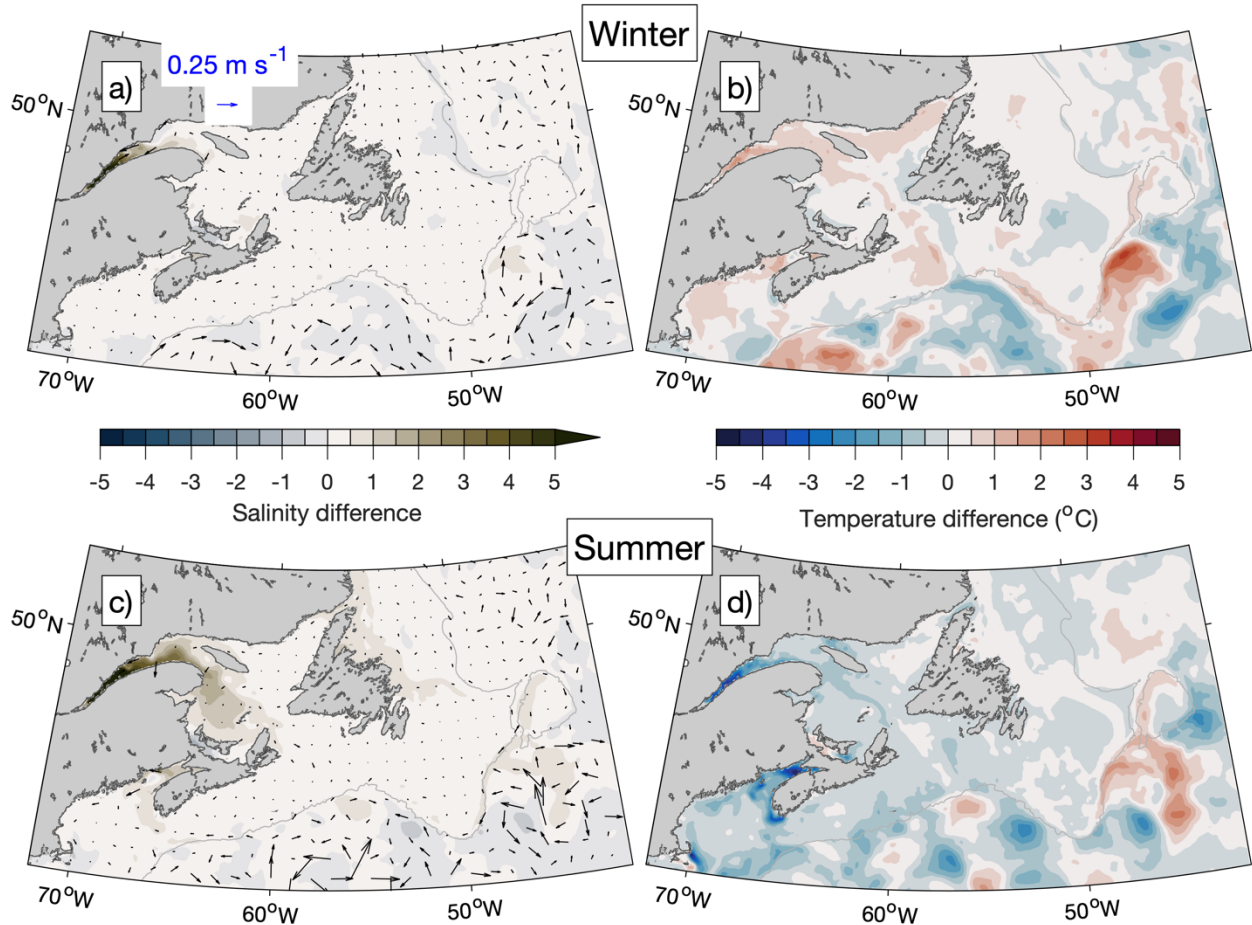
667
 668
 669
 670
 671
 672

Figure 18. Differences between Prog and NoTides over Ungava Bay: 2015–2018 averages of seasonal-mean simulated currents (thick magenta arrows: Prog, thin green arrows: NoTides) and temperature difference (Prog minus NoTides) at the sea surface (a, c) and bottom layer (b, d) in winter (a–b) and summer (c–d). Current vectors are shown at every sixth model grid point. The gray contour line represents the 100-m water depth.



673
 674
 675
 676
 677
 678

Figure 19. 2015–2018 averages of seasonal-mean sea ice concentrations in Ungava Bay during summer simulated in runs Prog (a) and NoTides (b); seasonal-mean sea surface temperature for summer simulated by runs Prog (c) and NoTides (d).



679
 680
 681 **Figure 20.** Similar to Fig. 18, but for the area between the Gulf of Maine and the southern Labrador Sea.

682 **4.2 The effect of sea ice**

683 The effect of sea ice is examined next by comparing simulated surface fields from Prog to those
 684 from the simulation in which ROMS is run without coupling to CICE (NoIce). A prominent
 685 feature in winter is the horizontal gradient in ΔS_{sfc}^{P-NI} , approximately aligned with the 1000-m
 686 isobath, in western Baffin Bay (Fig. 21a). ΔS_{sfc}^{P-NI} is positive on the shelf (~ -0.2) but negative
 687 offshore of the shelf break (~ -0.3). In the zone where ΔS_{sfc}^{P-NI} changes signs, $\Delta |\vec{V}|_{sfc}^{P-NI}$ is positive
 688 (up to $\sim 0.3 \text{ m s}^{-1}$). The area on the shelf where ΔS_{sfc}^{P-NI} is positive coincides with the highest
 689 average sea ice thickness in the domain (Fig. 10d), which makes the higher salinity in Prog
 690 consistent with brine rejection at the time of sea ice formation. Values of $|\Delta T_{sfc}^{P-NI}|$ in winter (Fig.
 691 21b) tend to be largest over the parts of Baffin Bay and the northern Labrador Shelf where the

692 ice edge occurs in Prog (Fig. 10c). ΔT_{sfc}^{P-NI} in these areas are negative (as low as $\sim -1.9^\circ$). Surface
693 heat flux is expected to result in positive ΔT_{sfc}^{P-NI} , given that in winter it is expected to cool the
694 ocean surface while sea ice can insulate the ocean surface below from cold air. Another possible
695 factor in ΔT_{sfc}^{P-NI} is vertical mixing, which is examined later.

696 In summer, ΔS_{sfc}^{P-NI} and ΔT_{sfc}^{P-NI} (Fig. 21c and 21d respectively) are lowest in western Baffin Bay,
697 with the former as low as ~ -4.0 psu (reflecting the input of freshwater due to melting sea ice) and
698 the latter as low as $\sim -4.7^\circ\text{C}$ (reflecting the blocking of shortwave radiation by the sea ice that
699 remains in summer). These results suggest that, as sea ice in areas such as Baffin Bay and the
700 Labrador Shelf decline in a warming climate, areas downstream from them such as the Scotian
701 Shelf and the Gulf of Maine will experience changes in the temperature and salinity of the water
702 that is brought there by the Labrador Current. The effect of changes in water masses advected
703 into a given area, in combination with changes that occur in situ due to climate change, is
704 another possible topic of future research.

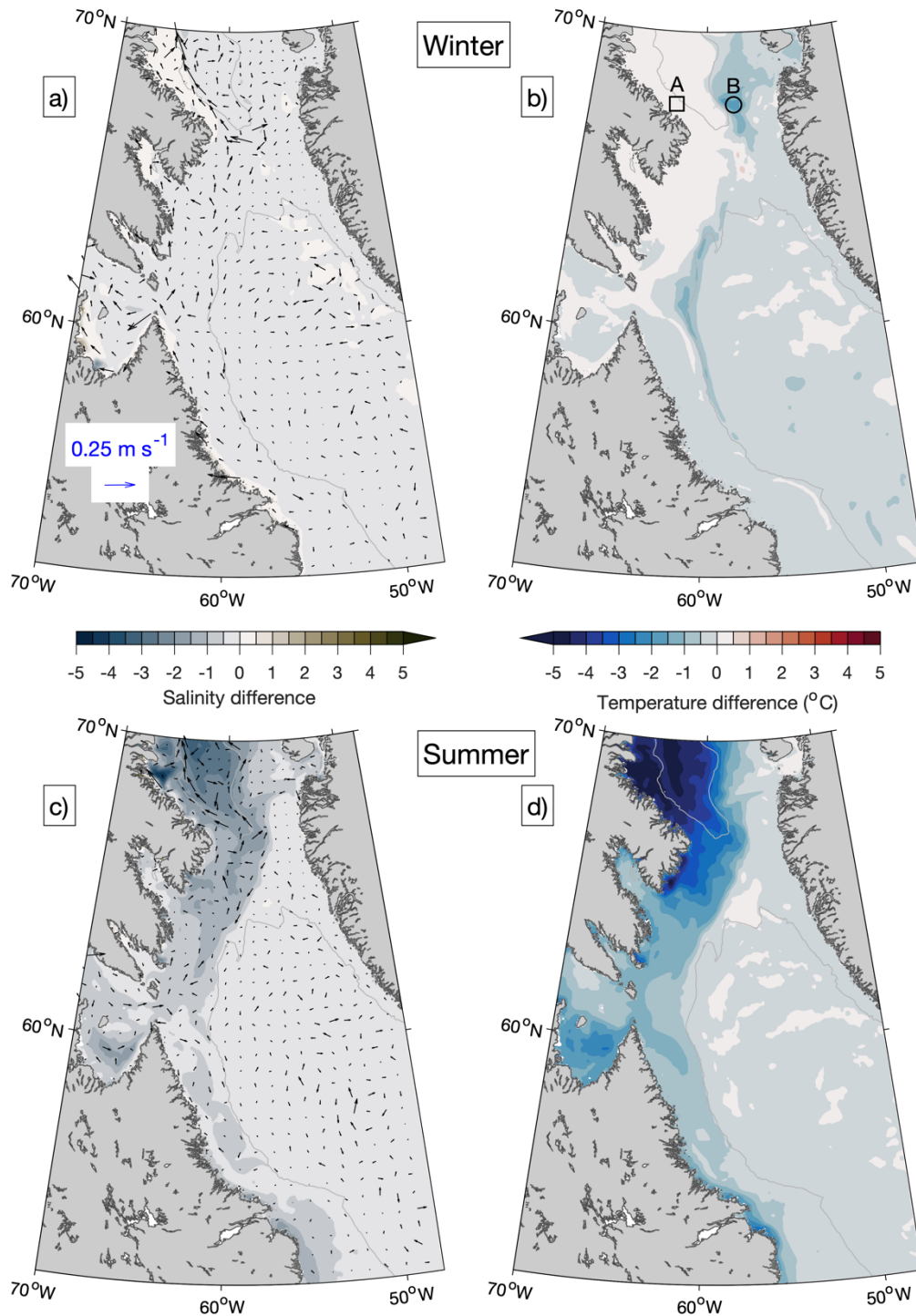
705 Differences in the wintertime vertical stratification and vertical mixing between Prog and NoIce
706 are examined further using vertical profiles of four-year mean wintertime temperature, salinity,
707 and vertical eddy viscosity produced by the two runs, as well as the squared buoyancy frequency
708 (N^2) calculated from the mean wintertime temperature and salinity using the Gibbs-SeaWater
709 Oceanographic Toolbox (McDougall and Barker, 2011). The profiles represent temporal averages
710 over the same period as in Figs. 21a–b (winters of 2015–2018) and are calculated at 1-m depth
711 intervals for two locations: location A (62.56° W, 67.60° N), indicated by the square in Fig. 21b,
712 where ΔT_{sfc}^{P-NI} is small and the 2015–2018 mean of the February-mean sea ice cover is $\sim 95\%$
713 (Fig. 10c), and location B (57.64° W, 67.60° N), indicated by the circle in Fig. 21b, where
714 ΔT_{sfc}^{P-NI} has a large magnitude ($\sim -1.9^\circ\text{C}$) and the four-year mean of the February-mean sea ice
715 cover is $\sim 84\%$. The model's water depths at the two locations are similar (231 m and 218 m).

716 The vertical profiles of mean wintertime temperature (Fig. 22a) and salinity (Fig. 22b) at location
717 A are similar between runs Prog and NoIce, with a vertical range of $<1.4^\circ\text{C}$ for temperature and
718 <0.8 for salinity in both runs. The profiles of N^2 (Fig. 22c) are thus also similar between the runs,
719 with maximum values of $\sim 6 \times 10^{-5} \text{ s}^{-2}$ about 40 m below the sea surface. Negative values of N^2 ,
720 indicating instability, are limited to the top few metres of the water column. Values of the

721 Richardson number (not shown) below 0.25, including negative values, are limited to the top 5 m
722 of the water column, again indicating a mostly stable water column and weak convection in both
723 Prog and NoIce. The mean wintertime vertical mixing below the surface is very weak in both
724 runs (Fig. 22d), with the vertical eddy diffusivity from both runs having maximum values of
725 $\sim 0.02 \text{ m}^2 \text{ s}^{-1}$ about 10 m below the surface and having values $< 0.002 \text{ m}^2 \text{ s}^{-1}$ in $\sim 80\%$ of the water
726 column. It should be noted that the mean wintertime stress exerted on the sea surface (by winds
727 and/or sea ice in Prog and by winds in NoIce) differs significantly between the two runs (Fig.
728 22d). The surface stress has a much smaller magnitude in Prog (0.02 N m^{-2}) than in NoIce (1.0 N
729 m^{-2}), which can be explained by the buffering effect of sea ice on the wind stress in Prog. Due to
730 this buffering effect of sea ice, the wind-induced vertical mixing in the surface layer (Fig. 22d) is
731 weaker in Prog than in NoIce, as expected.

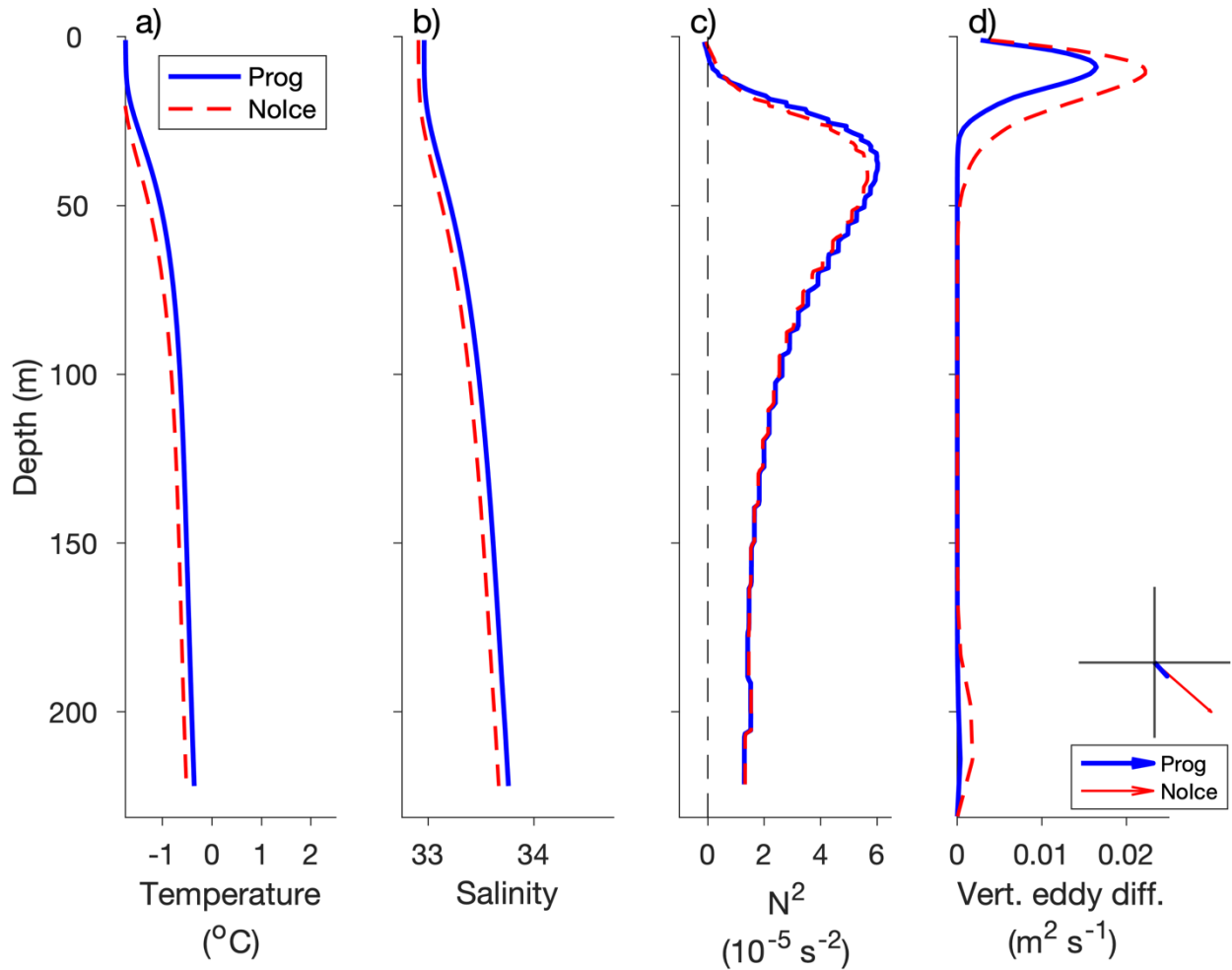
732 In contrast to location A, the vertical profiles of mean wintertime model results at location B
733 differ significantly between runs Prog and NoIce. The mean wintertime temperature (Fig. 23a)
734 has a vertical range of $> 3^\circ\text{C}$ in Prog (about -0.9°C near the surface and 2.4°C near the bottom)
735 but $< 1.0^\circ\text{C}$ in NoIce (about 1.1°C near the surface and 1.7°C near the bottom). The mean
736 wintertime salinity (Fig. 23b) has a vertical range of ~ 0.5 in Prog (about 34.0 near the surface
737 and 34.5 near the bottom) but just ~ 0.1 in NoIce (about 34.5 near the surface and 34.6 near the
738 bottom). Values of N^2 (Fig. 23c) from both runs are lower than at location A; with a maximum of
739 $\sim 1.9 \times 10^{-5} \text{ s}^{-2}$ in Prog and $\sim 2.1 \times 10^{-6} \text{ s}^{-2}$ in NoIce. In addition, the N^2 in NoIce is negative in the
740 top ~ 20 m of the water column and between depths of ~ 40 and ~ 50 m, indicating unstable
741 stratification and unrealistically strong convection. The Richardson number is < 0.25 in the top ~ 5
742 m of the water column in Prog, and at approximately the same depths as the negative values of
743 N^2 in NoIce. The maximum vertical eddy diffusivity coefficient is $\sim 0.3 \text{ m}^2 \text{ s}^{-1}$ in NoIce, which is
744 much larger than the maximum values of $\sim 0.06 \text{ m}^2 \text{ s}^{-1}$ in Prog, while the surface stress is similar
745 at $\sim 0.1 \text{ N m}^{-2}$ in both runs.

746 A possible explanation for the relatively warm ($> 2.0^\circ\text{C}$) and salty (> 34.0 psu) subsurface water
747 in the lower water column at location B in Prog (solid blue lines in Fig. 23a,b) is the horizontal
748 advection of relatively warm and salty waters from the south to this location. In Prog, the ocean-
749 to-air heat flux in winter results in cooling of the near-surface water as well as sea ice formation,
750 and subsurface ablation of the sea ice can be a source of fresh water that contributes to vertical



751
752
753
754
755
756
757

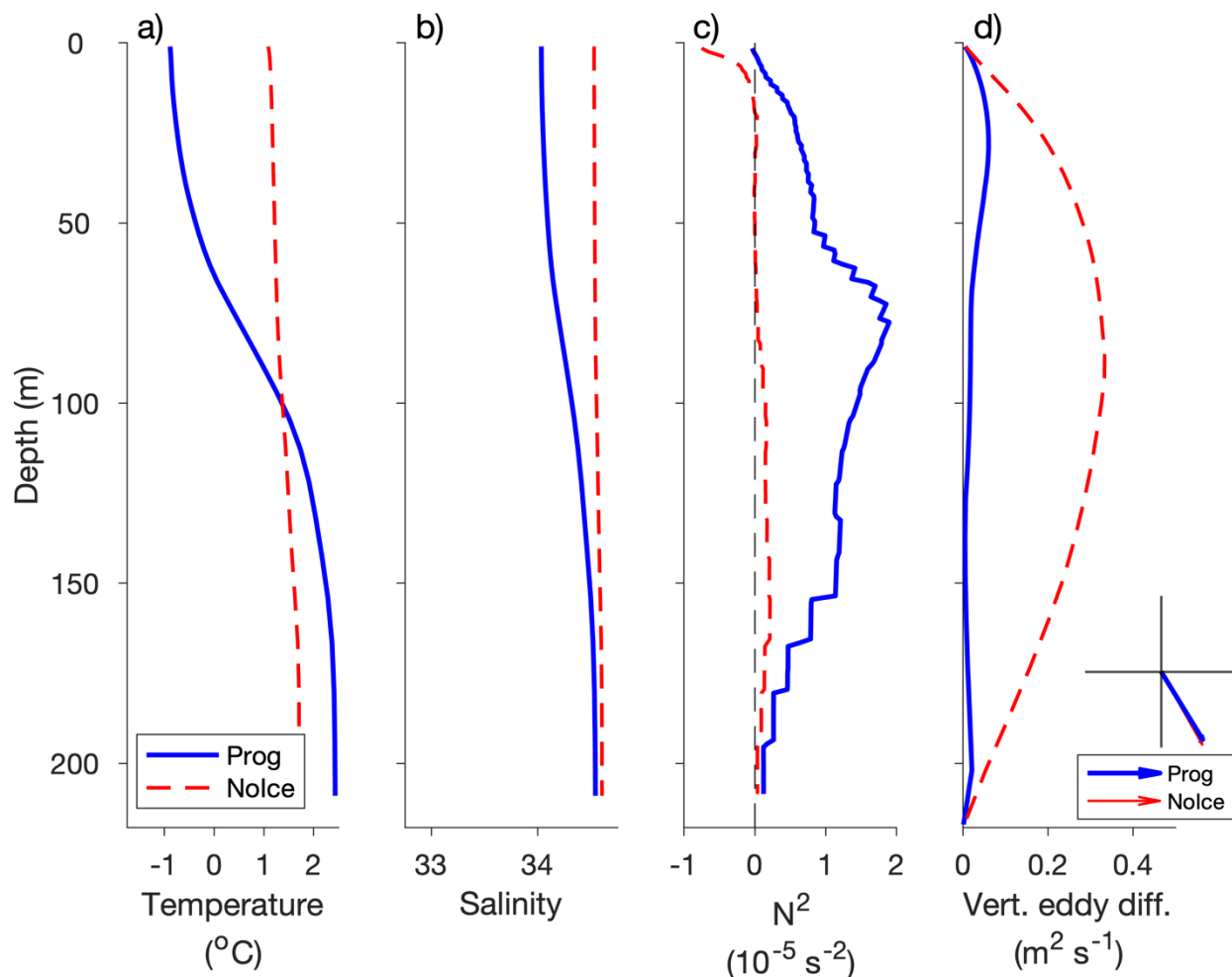
Figure 21. Differences in seasonal-mean simulated sea surface salinity and currents (**a, c**) and temperature (**b, d**) over Baffin Bay and the Labrador Sea when results of NoIce are subtracted from those of Prog, averaged over winters (**a, b**) and summers (**c, d**) of 2015–2018. Difference vectors are shown at every 12th model grid point. The gray contour line represents the 1000-m water depth. Locations A and B, for which the vertical profiles of model variables are shown in Figs. 22 and 23, are indicated in panel (**b**) with a square and a circle respectively.



758
 759
 760
 761
 762
 763
 764
 765

Figure 22. Vertical profiles of wintertime temperature (a), salinity (b), squared buoyancy frequency (c), and vertical eddy diffusivity (d) simulated by the model in Prog (blue solid line) and NoIce (red dashed line), averaged over 2015–2018, interpolated to 1-m depth intervals, at location A, indicated by the square in Fig. 21b (62.56° W, 67.60° N). Also shown in panel (d) is the stress exerted on the sea surface by sea ice and/or winds in the Prog (thick arrow) and NoIce (thin arrow) runs, averaged over the same period as the other fields. The x- and y-axes for the surface stress range from -0.1 to 0.1 N m^{-2} .

766



767

768

769 **Figure 23.** Similar to Fig. 22 but for location B, indicated by the circle in Fig. 21b (57.64° W , 67.60° N). Note the
770 change from Fig. 22 in the x-axis limits for the squared buoyancy frequency (c) and the vertical eddy diffusivity (d).

771 stability. The advection of relatively warm, salty subsurface waters from the south would also
772 occur in NoIce, but in this case the near-surface water would be cooled to the freezing point
773 without an accompanying reduction in salinity, which may explain the very large vertical mixing
774 and nearly uniform vertical profiles of temperature and salinity in this run.

775 5 Conclusions

776 In this study, a newly-developed, fully-coupled modelling system for simulating the ocean
777 circulation, sea ice, and biogeochemistry of the northwest North Atlantic Ocean (DalROMS-

778 NWA12 v1.0) was described. The model domain covers the area from Cape Hatteras to Baffin
779 Bay with a horizontal resolution of ~2 to ~8 km, making this modelling system highly suitable
780 for a range of research topics, including study of the biological carbon pump and quantification
781 of the major physical and biogeochemical (BGC) processes influencing the ocean carbon cycle
782 over the region. The results of two simulations using this modelling system, with and without
783 nudging of the simulated temperature and salinity towards a blend of observations and
784 reanalysis, were compared to observations and reanalysis. We found that results of the control
785 run, which included the nudging, are more realistic than results of the prognostic (un-nudged)
786 simulation for several important physical features observed in this region, such as separation of
787 the Gulf Stream and the West Greenland Current from their respective coasts, as well as
788 propagation of low-salinity waters from the St. Lawrence Estuary. These results demonstrate the
789 utility of simple data assimilation in reducing the systematic model errors that can be attributed
790 to model configuration (such as horizontal grid resolution in the case of currents' separation from
791 coasts and the choice of tracer advection scheme in the case of estuarine plume propagation) and
792 unresolved or parameterized physical and BGC processes. The prognostic simulation, while
793 having difficulties with the above-mentioned features, was able to reproduce the general
794 spatiotemporal patterns of the physical fields and outperformed the control run in terms of the
795 sea ice concentration. The major differences between the simulations in the sea ice extent
796 highlight the complex nature of interactions among the atmosphere, ocean, and sea ice.

797 The modelling system was able to reproduce the general patterns of BGC variables over the
798 northwest Atlantic shelves and in the Labrador Sea. Further validation will include comparisons
799 with observations made by BGC Argo floats (Johnson and Claustre, 2016). Future work will use
800 this modelling system to investigate the biological carbon pump in the Labrador Sea including
801 vertical flux estimates derived from BGC Argo (Wang and Fennel, 2022 and 2023). The addition
802 of silicate as a state variable will also be tested.

803 As an example of application of this modelling system, sensitivity studies were made in which
804 results of the prognostic simulation were compared to those from similar simulations from which
805 either the tides or simulation of sea ice were excluded. The comparisons suggest that tides and
806 sea ice strongly affect the physical oceanography of the NWA in several ways. These include the

807 combined effects of tides and sea ice (in Ungava Bay) as well as individual effects (e.g., higher
808 surface salinity in summer when sea ice is not simulated).

809 In addition to studies of the biological carbon pump and of the downstream effects of changes in
810 the water transported by the Labrador Current, another possible direction of future research is to
811 explore further the effects of model configuration, such as parameterization of deep convection
812 or the choice of advection schemes (including the use of non-zero horizontal eddy diffusivity and
813 viscosity with the third-order upstream scheme). In addition, we can use the ocean state
814 simulated by this model as input for numerical particle-tracking experiments to investigate
815 connectivity among different areas of the NWA. The resulting metrics of connectivity under
816 current and projected future climate conditions can support decision-making processes
817 concerning conservation measures. The model will also be used to compare approaches to
818 reducing bias in long-term simulations (Renkl et al., in prep.).

819 The high air-to-sea flux of CO₂ and the subsequent downward export of fixed carbon make the
820 NWA a key component in the global climate system, but it is a remote region where seasonal
821 transitions can take place in just a few weeks (e.g., in terms of pCO₂; Körtzinger et al., 2008) and
822 details of the interactions between physical and biogeochemical processes are still unknown or
823 remain poorly integrated into models (e.g., the sea-ice carbon pump; Richaud et al., 2023). The
824 four-dimensional ocean states produced by numerical models can aid in the interpretation of
825 observations as well as enable experiments that elucidate the roles of various processes in the
826 ocean and how those processes might change under future climate scenarios. As part of our
827 future studies, this advanced coupled modelling system will be run for longer simulation periods
828 to examine the effects of climate change on the marine conditions over the NWA. The modelling
829 system will also be used to predict the temporal and spatial variability of future marine
830 conditions over the region under different climate scenarios.

831 **Appendix A: The vertical coordinate system in ROMS**

832 ROMS uses a generalized terrain-following vertical coordinate system with several options
833 for vertical transformation equations and vertical stretching functions. In this study the default
834 configuration is used, with the vertical coordinate S defined as (Hedstrom, 2018):

$$835 \quad z(x, y, \sigma, t) = \zeta(x, y, t) + [\zeta(x, y, t) + h(x, y)]S(x, y, \sigma) \quad (\text{A1})$$

836
$$S(x, y, \sigma) = \frac{h_c + h(x, y)C(\sigma)}{h_c + h(x, y)} \quad (\text{A2})$$

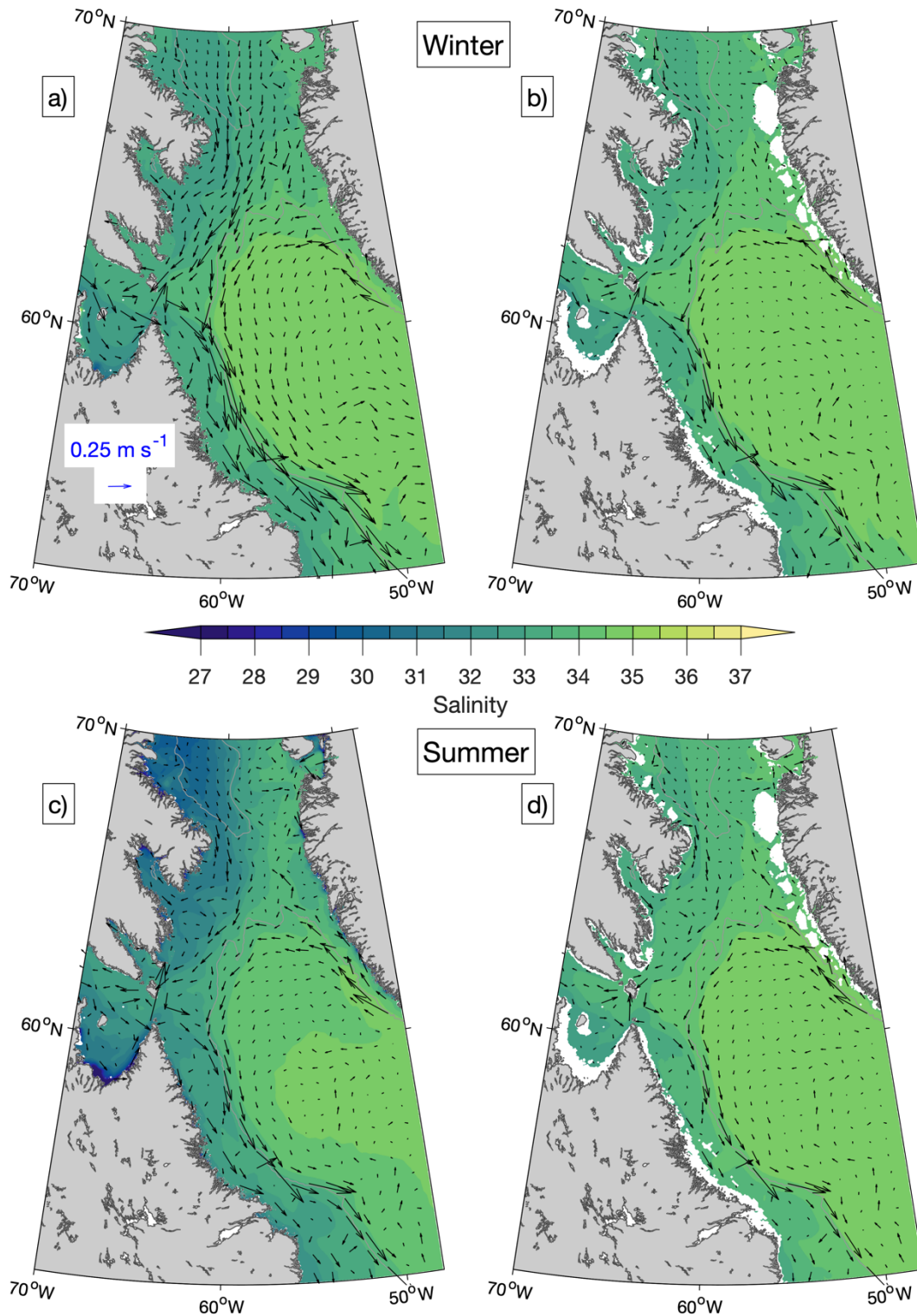
837
$$C(\sigma) = \frac{\exp(\theta_B C'(\sigma)) - 1}{1 - \exp(-\theta_B)} \quad (\text{A3})$$

838
$$C'(\sigma) = \frac{1 - \cosh(\theta_S \sigma)}{\cosh(\theta_S) - 1} \quad (\text{A4})$$

839 where σ ranges from 0 at the free surface to -1 at the ocean bottom, ζ is the free surface, h is the
 840 undisturbed water column thickness, h_c is the value of h below which the vertical layers are more
 841 uniformly spaced, and θ_s and θ_b are parameters that control the vertical resolution near the
 842 surface and the bottom respectively. In this study ROMS has 40 layers and the parameters h_c , θ_s ,
 843 and θ_b are set to 100 m, 5.0, and 0.5 respectively.

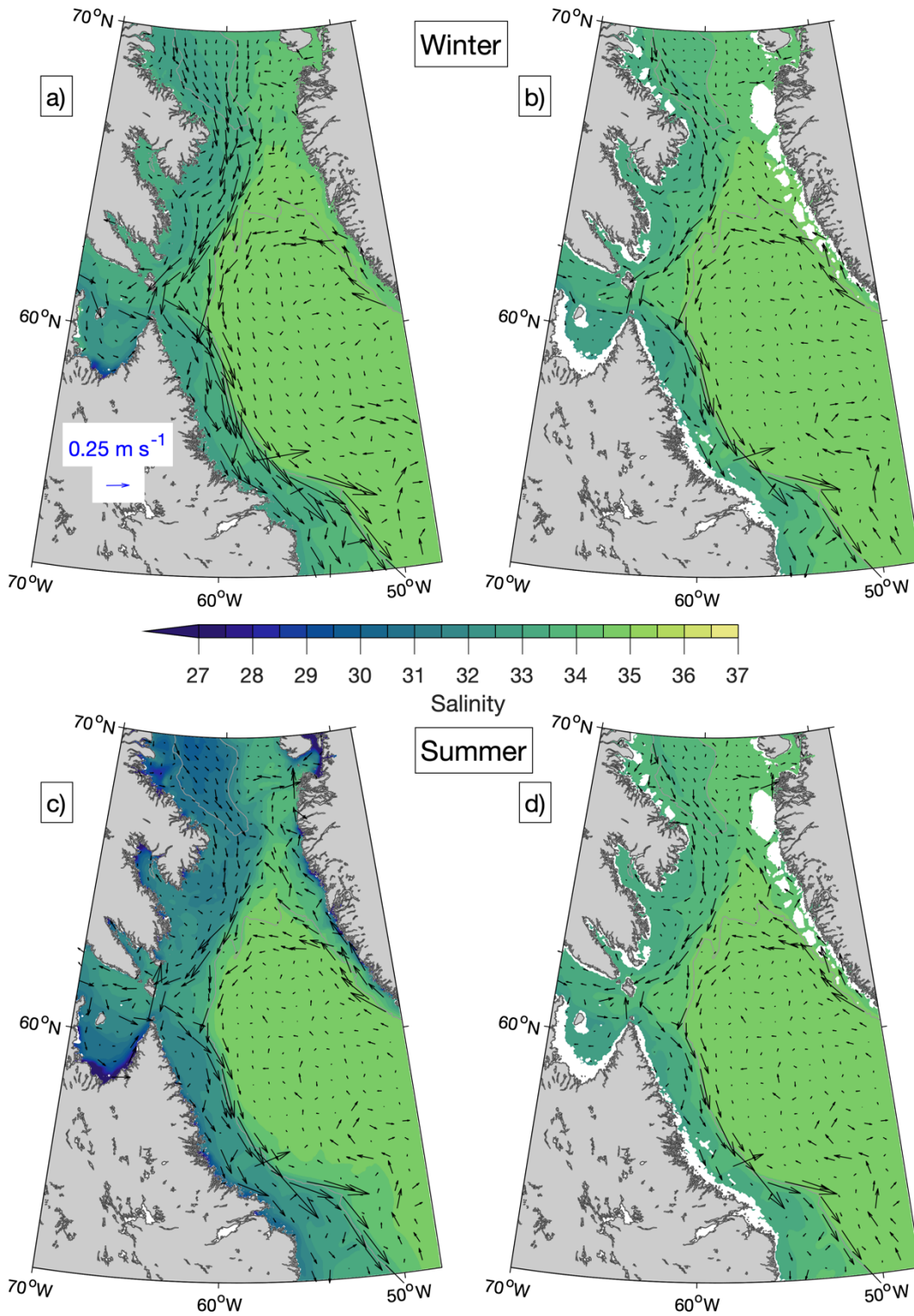
844 **Appendix B: Seasonal-mean simulated fields**

845 Seasonal means of salinity and currents in Baffin Bay and the northern Labrador Sea
 846 simulated in Ctrl and Prog, averaged over the period December 2014–December 2018, are
 847 shown in Figs. B1 and B2. Differences between the simulations are more evident in summer
 848 (June–August; Figs. B1c–d and B2c–d than in winter (December–February; Figs. B1a–b and
 849 B2a–b). The northward branch of the West Greenland Current and the Baffin Island Current are
 850 stronger in Prog by up to $\sim 0.25 \text{ m s}^{-1}$ at the surface and $\sim 0.15 \text{ m s}^{-1}$ for model results interpolated
 851 to the 100-m depth. In the area between the southern Labrador Sea and the Gulf of Maine (Figs.
 852 B3 and B4), the difference in salinity between the simulations is more prominent in summer,
 853 following the annual peak in freshwater discharges from the St. Lawrence and other rivers. In the
 854 St. Lawrence Estuary, the 2015–2018 mean of summer surface salinity simulated in Prog is
 855 lower than that from Ctrl by up to ~ 3.5 , but further downstream in the Gulf of St. Lawrence, the
 856 salinity from Prog is higher by ~ 2 .



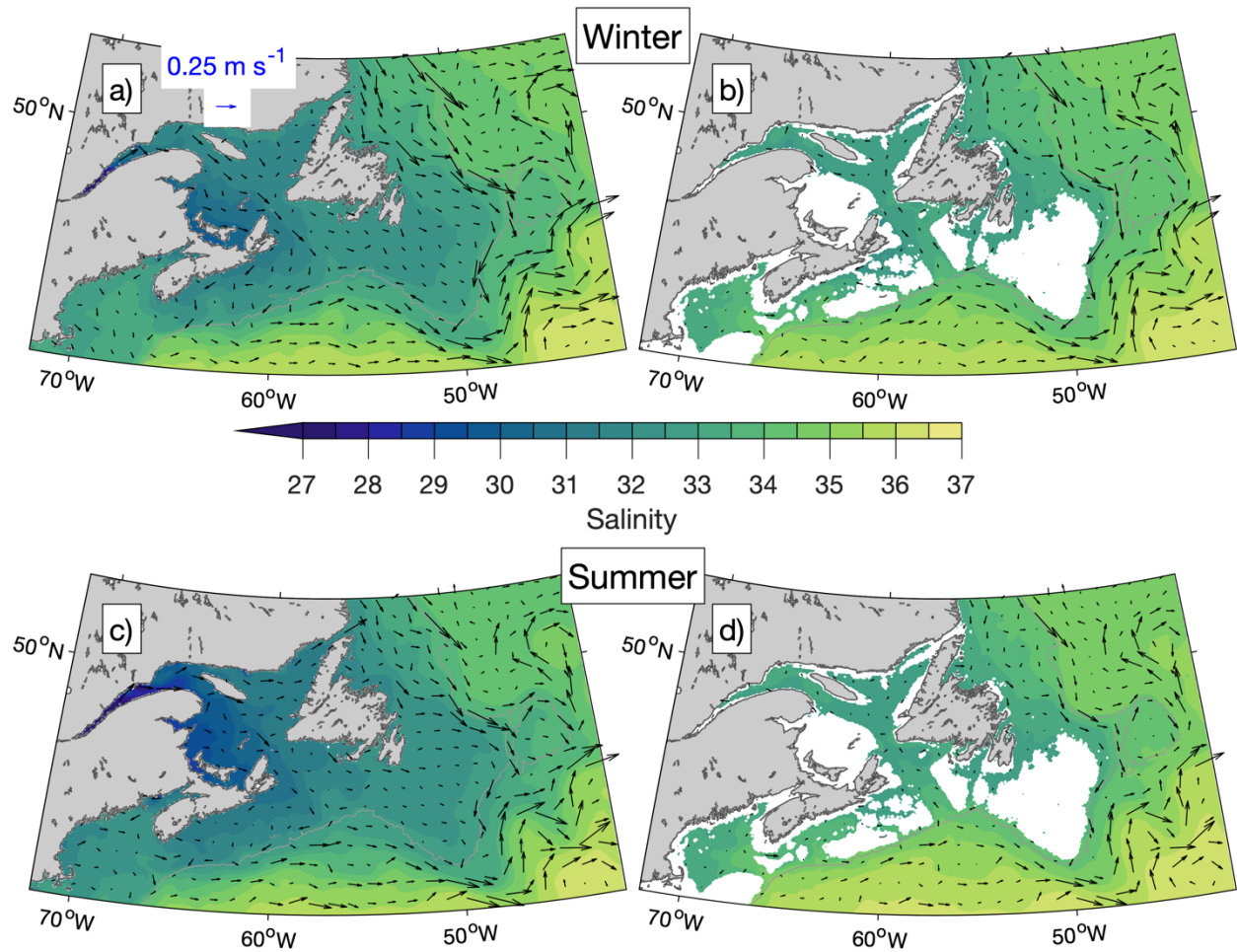
857
858
859
860
861
862

Figure B1. Seasonal-mean simulated salinity and currents at the sea surface (a, c) and interpolated to the 100-m depth (b, d) from Ctrl averaged over the winters (a, b) and summers (c, d) of 2015–2018 in Baffin Bay and the Labrador Sea. Winters are defined as December of the previous year to February of that year. Summers are defined as June to August. Current vectors are shown at every 12th grid point. The 1000-m depth contour is shown in gray.



863
864
865

Figure B2. Similar to Figure B1 but for Prog.



866

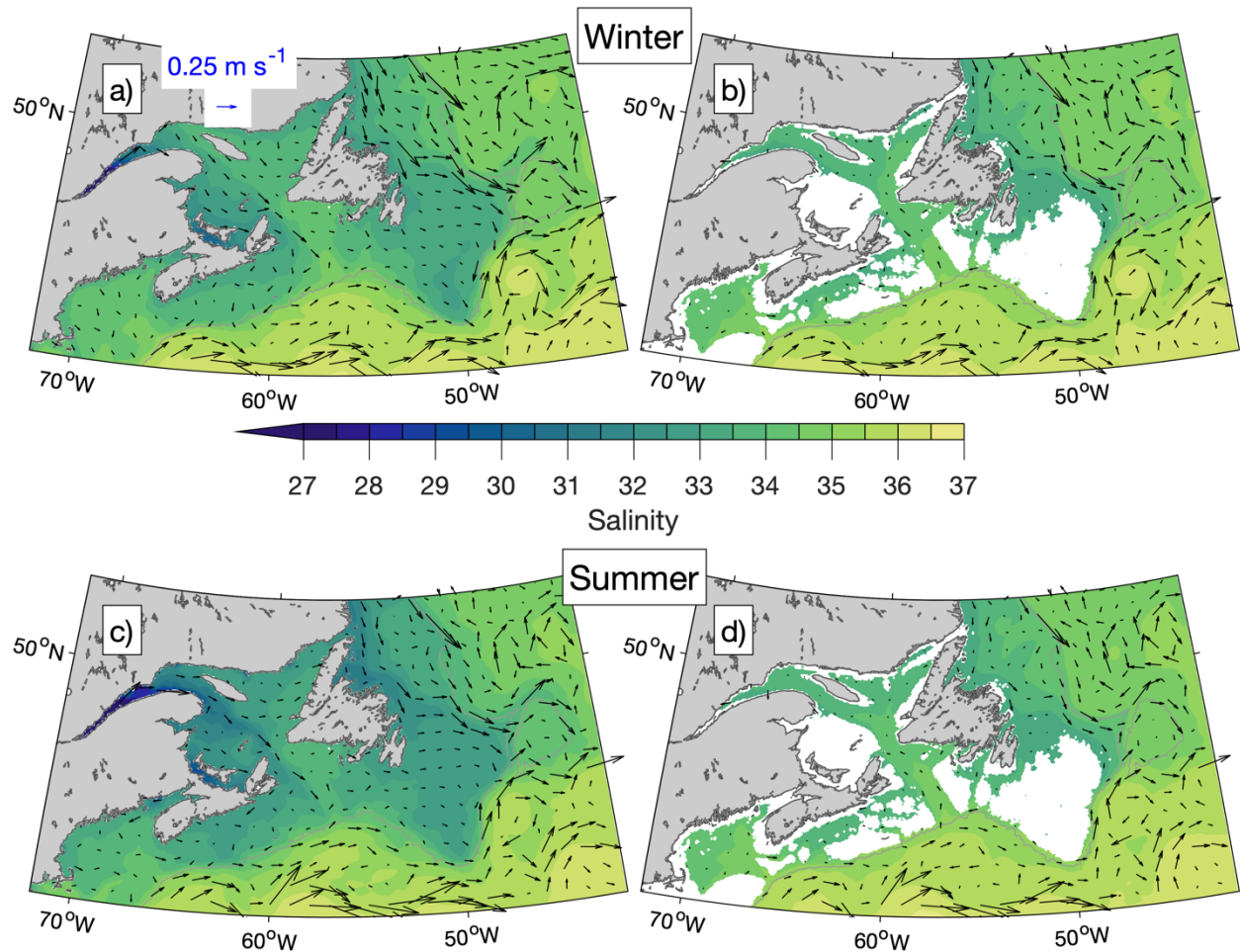
867

868

869

870

Figure B3. Seasonal-mean simulated salinity and currents at the sea surface (**a, c**) and interpolated to the 100-m depth (**b, d**) from Ctrl averaged over the winters (**a, b**) and summers (**c, d**) of 2015–2018 over the area between the Gulf of Maine and the southern Labrador Sea. Current vectors are shown at every 12th grid point. The 1000-m depth contour is shown in gray.



871
872
873

Figure B4. Similar to Fig. B3 but for Prog.

874 **Appendix C: Datasets used in model performance assessment**

875 Online sources of the datasets used to assess the model performance are listed below in the order
876 they are discussed in Section 3.

- 877 1. Sea surface temperature: OISST v2.1 (Huang et al., 2021), a daily dataset on a 1/4° grid that
878 incorporates satellite and in situ observations. A combination of v2.0 and v2.1 was used in this
879 study; v2.0 is now retired. <https://www.ncei.noaa.gov/products/optimum-interpolation-sst>
- 880 2. Sea surface salinity: MULTI_OBS_GLO_PHY_S_SURFACE_MYNRT_015_013 (Buongiorno
881 Nardelli et al., 2016), a dataset that incorporates satellite and in situ observations. At the time
882 of this study, it was a weekly dataset on a 1/4° grid; now it is a daily dataset on a 1/8° grid.
883 https://data.marine.copernicus.eu/product/MULTI_OBS_GLO_PHY_S_SURFACE_MYNRT_015_013/description
884

- 885 3. Currents: GLOBAL_MULTIYEAR_PHY_001_030, also known as GLORYS12V1
886 (Lellouche et al., 2021), a daily reanalysis dataset on a 1/12° grid.
887 https://data.marine.copernicus.eu/product/GLOBAL_MULTIYEAR_PHY_001_030/description
888 [on](https://data.marine.copernicus.eu/product/GLOBAL_MULTIYEAR_PHY_001_030/description)
- 889 4. Shipboard observations of physical and biogeochemical variables: Atlantic Zone Monitoring
890 Program (Pepin et al., 2005) cruises take place seasonally and Atlantic Zone Off-Shelf
891 Monitoring Program (e.g., Yashayaev and Loder, 2017) cruises take place annually.
892 https://catalogue.cioosatlantic.ca/dataset/ca-cioos_9a4bd73f-12a2-40ff-a7c7-b961a1d11311
893 https://catalogue.cioosatlantic.ca/dataset/ca-cioos_15f90eab-21ed-447d-aea7-8fe98ea27fe5
- 894 5. Sea ice: AMSR2 ASI sea ice concentration data for the Arctic, v5.4 (Melsheimer and Spreen,
895 2019), a daily dataset on a 6.5-km grid derived from satellite observations.
896 <https://doi.pangaea.de/10.1594/PANGAEA.898399>

897 **Code and Data Availability**

898 The model codes, scripts for compiling the model, and sample CPP header and runtime
899 parameter files for physics-only simulations are available at
900 <https://doi.org/10.5281/zenodo.12752091> (Ohashi et al., 2024a). Input files used by the ocean
901 circulation and sea ice modules in a simulation of September – December 2013 are available at
902 <https://doi.org/10.5281/zenodo.12752190> (Ohashi et al., 2024b),
903 <https://doi.org/10.5281/zenodo.12734049> (Ohashi et al., 2024c), and
904 <https://doi.org/10.5281/zenodo.12735153> (Ohashi et al., 2024d). Daily-mean output files from
905 the ocean circulation, sea ice, and biogeochemistry modules are available for September 2013
906 (beginning of simulation period) at <https://doi.org/10.5281/zenodo.12744506> (Ohashi et al.,
907 2024e) and for January 2015 (beginning of model validation period) at
908 <https://doi.org/10.5281/zenodo.12746262> (Ohashi et al., 2024f). Input and output files for the
909 remainder of the simulation period, as well as CPP header, runtime parameter, and input files for
910 the biogeochemistry module, are available from the corresponding author KO upon request.

911 **Author contributions**

912 KO configured the ocean circulation model; prepared the model bathymetry, freshwater input
913 files, atmospheric forcing files, and some of the lateral boundary input files; and carried out the
914 Prog, NoTides, and NoIce runs. AL prepared input files for and configured the biogeochemical
915 module; and carried out the Ctrl run. CR configured the sea ice model and its coupling to the
916 ocean circulation model; prepared some of the lateral boundary input files and the pseudo-mean
917 versions of freshwater input files; configured the regions used to evaluate model performance;
918 processed the observations used in model evaluation; and calculated the model errors with
919 respect to AZMP observations. AL carried out the analyses for and prepared Figs. 13–15; and
920 wrote the text describing the biogeochemical module, the Ctrl run, and Figs.13–15. KO prepared
921 the rest of the manuscript with advice from JS. JS, KF, and EO provided advice throughout
922 development and evaluation of the model and provided funding to KO, AL, and CR respectively.

923 **Competing interests**

924 The authors declare that they have no conflicts of interest.

925 **Acknowledgements**

926 This study is part of the Ocean Frontier Institute’s research project “The Northwest Atlantic
927 Biological Carbon Pump”. Simulations were carried out on computing resources maintained by
928 the Digital Research Alliance of Canada. JS, KF, and EO acknowledge support from the National
929 Science and Engineering Research Council of Canada’s Discovery Grant program. JS and KO
930 were supported by funding from Fisheries and Oceans Canada (for the project “Modelling
931 ecological connectivity among Canada’s Atlantic Marine Protected Areas during the
932 Anthropocene”) during preparation of this manuscript. CR was supported by a postdoctoral
933 fellowship from the Marine Environmental Observation, Prediction and Response network
934 (MEOPAR). The authors thank Fehmi Dilmahamod, Xianmin Hu, Bin Wang, and Shengmu Yang
935 for their suggestions and assistance during development of the model. We are also grateful for
936 the constructive comments provided by two anonymous reviewers, which led to the addition of
937 section 3.5 and many other enhancements to the manuscript. Maps in this study were generated

938 using the package M_Map (Pawlowicz, 2020). The colour maps used in this study are by Thyng
939 et al. (2016) and Cramer (2018).

940 References

- 941 Allen, J. S., Newberger, N. A., and Federiuk, J.: Upwelling circulation on the Oregon continental shelf. Part I:
942 Response to idealized forcing, *J. Phys. Oceanogr.*, 25(8), 1843–1866, [https://doi.org/0.1175/1520-0485\(1995\)025%3C1843:UCOTOC%3E2.0.CO;2](https://doi.org/0.1175/1520-0485(1995)025%3C1843:UCOTOC%3E2.0.CO;2), 1995.
- 943
944
- 945 Babb, D. G., Kirillov, S., Galley, R. J., Straneo, F., Ehn, J. K., Howell, S. E. L., Brady, M., Ridenour, N. A., and
946 Barber, D. G.: Sea ice dynamics in Hudson Strait and its impact on winter shipping operations, *J. Geophys. Res.-*
947 *Oceans*, 126, e2021JC018024, <https://doi.org/10.1029/2021JC018024>, 2021.
- 948
- 949 Bamber, J. L., Tedstone, A. J., King, M. D., Howat, I. M., Enderlin, E. M., van den Broeke, M. R., and Noel, B.:
950 Land ice freshwater budget of the Arctic and North Atlantic Oceans: 1. Data, methods, and results, *J. Geophys.*
951 *Res.-Oceans*, 123, <https://doi.org/10.1002/2017JC013605>, 2018.
- 952
- 953 Bitz, C. M. and Lipscomb, W. H.: An energy-conserving thermodynamic model of sea ice, *J. Geophys. Res.*,
954 104(C7), 15669–15677, <https://doi.org/10.1029/1999JC900100>, 1999.
- 955
- 956 Bouillon, S., Fichefet, T., Legat, V., and Madec, G.: The elastic-viscous-plastic method revisited, *Ocean Model.*, 71,
957 2–12, <https://doi.org/10.1016/j.ocemod.2013.05.013>, 2013.
- 958
- 959 Bourgault, D. and Koutitonsky, V. G.: Real-time monitoring of the freshwater discharge at the head of the St.
960 Lawrence Estuary, *Atmos.-Ocean*, 37(2), 203–220, <https://doi.org/10.1080/07055900.1999.9649626>, 1999.
- 961
- 962 Briegleb, B. P. and Light, B.: A Delta-Eddington multiple scattering parameterization for solar radiation in the sea
963 ice component of the Community Climate System Model, National Center for Atmospheric Research,
964 <https://doi.org/10.5065/D6B27S71>, 2007.
- 965
- 966 Buongiorno Nardelli, B., Droghei, R., and Santoleri, R.: Multi-dimensional interpolation of SMOS sea surface
967 salinity with surface temperature and in situ salinity, *Remote Sens. Environ.*, 180, 392–402,
968 <https://doi.org/10.1016/j.rse.2015.12.052>, 2016.
- 969
- 970 Cabanes, C., Grouazel, A., von Schuckmann, K., Hamon, M., Turpin, V., Coatanoan, C., Paris, F., Guinehut, S.,
971 Boone, C., Ferry, N., de Boyer Montégut, C., Carval, T., Reverdin, G., Pouliquen, S., and Le Traon, P.-Y.: The
972 CORA dataset: validation and diagnostics of in-situ ocean temperature and salinity measurements, *Ocean Sci.*, 9,
973 1–18, <https://doi.org/10.5194/os-9-1-2013>, 2013.
- 974
- 975 Chapman, D. C.: Numerical treatment of cross-shelf open boundaries in a barotropic coastal ocean model, *J. Phys.*
976 *Oceanogr.*, 15, 1060–1075, [https://doi.org/10.1175/1520-0485\(1985\)015%3C1060:NTOCSO%3E2.0.CO;2](https://doi.org/10.1175/1520-0485(1985)015%3C1060:NTOCSO%3E2.0.CO;2), 1985.
- 977
- 978 Chassignet, E. P. and Xu, S.: Impact of horizontal resolution (1/12° to 1/50°) on Gulf Stream separation, penetration,
979 and variability, *J. Phys. Oceanogr.*, 47(8), 1999–2021, <https://doi.org/10.1175/JPO-D-17-0031.1>, 2017.
- 980
- 981 Chelton, D., DeSzoeke, R. A., Schlax, M. G., El Naggar, K., and Siwertz, N.: Geographical variability of the first
982 baroclinic Rossby radius of deformation. *J. Phys. Oceanogr.*, 28(3), 433–460, [https://doi.org/10.1175/1520-0485\(1998\)028%3C0433:GVOTFB%3E2.0.CO;2](https://doi.org/10.1175/1520-0485(1998)028%3C0433:GVOTFB%3E2.0.CO;2), 1998.
- 983
- 984
- 985 Chen, K. and He, R.: Mean circulation in the coastal ocean off northeastern North America from a regional-scale
986 ocean model. *Ocean Sci.*, 11, 503–517, <https://doi.org/10.5194/os-11-503-2015>, 2015.
- 987
- 988 Cramer, F.: Scientific colour maps [software], Zenodo, <https://doi.org/10.5281/zenodo.1243862>, 2018.

989
990 Dai, A.: Dai and Trenberth Global River Flow and Continental Discharge Dataset [data set],
991 <https://doi.org/10.5065/D6V69H1T>, 2017.
992
993 Drinkwater, K.: On the mean and tidal currents in Hudson Strait, *Atmos.-Ocean*, 26(2), 252–266,
994 <https://doi.org/10.1080/07055900.1988.9649302>, 1988.
995
996 Dupont, F., Higginson, S., Bourdalle-Badie, R., Lu, Y., Roy, F., Smith, G. C., Lemieux, J.-F., Garric, G., and
997 Davidson, F.: A high-resolution ocean and sea-ice modelling system for the Arctic and North Atlantic oceans,
998 *Geosci. Model Dev.*, 8, 1577–1594, <https://doi.org/10.5194/gmd-8-1577-2015>, 2015.
999
1000 Egbert, G. D. and Erofeeva, S. Y.: Efficient inverse modeling of barotropic ocean tides, *J. Atmos. Ocean Tech.*, 19,
1001 183–204, [https://doi.org/10.1175/1520-0426\(2002\)019%3C0183:EIMOBO%3E2.0.CO;2](https://doi.org/10.1175/1520-0426(2002)019%3C0183:EIMOBO%3E2.0.CO;2), 2002.
1002
1003 Ezer, T. and Mellor, G. L.: A generalized coordinate ocean model and a comparison of the bottom boundary layer
1004 dynamics in terrain-following and in *z*-level grids, *Ocean Model.*, 6, 379–403, [https://doi.org/10.1016/S1463-](https://doi.org/10.1016/S1463-5003(03)00026-X)
1005 [5003\(03\)00026-X](https://doi.org/10.1016/S1463-5003(03)00026-X), 2004.
1006
1007 Fairall, C. W., Bradley, E. F., Godfrey, J. S., Wick, G. A., Edson, J. B., and Young, G. S.: Cool-skin and warm-layer
1008 effects on sea surface temperature, *J. Geophys. Res.*, 101(C1), 1295–1308, <https://doi.org/10.1029/95JC03190>,
1009 1996a.
1010
1011 Fairall, C. W., Bradley, E. F., Rogers, D. P., Edson, J. B., and Young, G. S.: Bulk parameterization of air-sea fluxes
1012 for Tropical-Ocean Global Atmosphere Coupled-Ocean Atmosphere Ocean Experiment, *J. Geophys. Res.*,
1013 101(C2), 3747–3764, <https://doi.org/10.1029/95JC03205>, 1996b.
1014
1015 Fennel, K., Mattern, J. P., Doney, S., Bopp, L., Moore, A., Wang, B., Yu, L., Ocean biogeochemical modelling, *Nat.*
1016 *Rev. Methods Primers*, 2, 76, <https://doi.org/10.1038/s43586-022-00154-2>, 2022.
1017
1018 Fennel, K., Wilkin, J., Levin, J., Moisan, J., O'Reilly, J., and Haidvogel, D.: Nitrogen cycling in the Middle Atlantic
1019 Bight: Results from a three-dimensional model and implications for the North Atlantic nitrogen budget, *Global*
1020 *Biogeochem. Cy.*, 20, GB3007, <https://doi.org/10.1029/2005GB002456>, 2006.
1021
1022 Fennel, K., Wilkin, J., Previdi, M., and Najjar, R.: Denitrification effects on air-sea CO₂ flux in the coastal ocean:
1023 Simulations for the northwest North Atlantic, *Geophys. Res. Lett.*, 35, L24608,
1024 <https://doi.org/10.1029/2008GL36147>, 2008.
1025
1026 Fennel, K., Hu, J., Laurent, A., Marta-Almeida, M., and Hetland, R.: Sensitivity of hypoxia predictions for the
1027 north- ern Gulf of Mexico to sediment oxygen consumption and model nesting, *J. Geophys. Res.-Oceans*, 118,
1028 990–1002, <https://doi.org/10.1002/jgrc.20077>, 2013.
1029
1030 Frajka-Williams, E. and Rhines, P. B.: Physical controls and interannual variability of the Labrador Sea spring
1031 phytoplankton bloom in distinct regions, *Deep-Sea Res. Pt. I*, 57, 541–552,
1032 <https://doi.org/10.1016/j.dsr.2010.01.003>, 2010. Garçon, V. C., Oschlies, A., Doney, S. C., McGillicuddy, D.,
1033 Waniek, J.: The role of mesoscale variability on plankton dynamics in the North Atlantic, *Deep-Sea Res. Pt. II*, 48,
1034 2199–2226, [https://doi.org/10.1016/S0967-0645\(00\)00183-1](https://doi.org/10.1016/S0967-0645(00)00183-1), 2001.
1035
1036 Gatien, M. G.: A study in the slope water region south of Halifax, *J. Fish. Res. Board Can.*, 33(10), 2213–2217,
1037 <https://doi.org/10.1139/f76-270>, 1976.
1038
1039 GEBCO Compilation Group: GEBCO 2019 Grid [data set], [https://doi.org/10.5285/836f016a-33be-6ddc-e053-](https://doi.org/10.5285/836f016a-33be-6ddc-e053-6c86abc0788e)
1040 [6c86abc0788e](https://doi.org/10.5285/836f016a-33be-6ddc-e053-6c86abc0788e), 2019.
1041
1042 Haidvogel, D. B., Arango, H., Budgell, W. P., Cornuelle, B. D., Curchister, E., Di Lorenzo, E., Fennel, K., Geyer, W.
1043 R., Hermann, A. J., Lanerolle, L., Levin, J., McWilliams, J. C., Miller, A. J., Moore, A. M., Powell, T. M.,
1044 Shchepetkin, A. F., Sherwood, C. R., Signell, R. P., Warner, and Wilkin, J.: Ocean forecasting in terrain-following

1045 coordinates: Formulation and skill assessment of the Regional Ocean Modeling System, *J. Comput. Phys.*, 227,
 1046 3595–3624, <https://doi.org/10.1016/j.jcp.2007/06.016>, 2008.
 1047
 1048 Han, G., Hannah, C. G., Loder, J. W., and Smith, P. C.: Seasonal variation of the three-dimensional mean circulation
 1049 over the Scotian Shelf, *J. Geophys. Res.*, 102(C1), 1011–1025, <https://doi.org/10.1029/96JC03285>, 1997.
 1050
 1051 Hedstrom, K. S.: Technical manual for a coupled sea-ice/ocean circulation model (Version 5), U.S. Dept. of the
 1052 Interior, Bureau of Ocean Energy Management, Alaska OCS Region, 2018.
 1053
 1054 Hersbach, H., Bell, B., Berrisford, P., Biavati, G., Horányi, A., Muñoz Sabater, J., Nicolas, J., Peubey, C., Radu, R.,
 1055 Rozum, I., Schepers, D., Simmons, A., Soci, C., Dee, D., Thépaut, J.-N.: ERA5 hourly data on single levels from
 1056 1979 to present [data set], Copernicus Climate Change Service Climate Data Store,
 1057 <https://doi.org/10.24381/cds.adbb2d47>, 2018.
 1058
 1059 Huang, B., Liu, C., Banzon, V., Freeman, E., Graham, G., Hankins, B., Smith, T., and Zhang, H.-M.: Improvements
 1060 of the Daily Optimum Interpolation Sea Surface Temperature (DOISST) Version 2.1, *J. Climate*, 34, 2923–2939,
 1061 <https://doi.org/10.1175/JCLI-D-20-0166.1>, 2021.
 1062
 1063 Hunke, E. C. and Dukowicz, J. K.: An elastic-viscous-plastic model for sea ice dynamics, *J. Phys. Oceanogr.*, 27,
 1064 1849–1867, [https://doi.org/10.1175/1520-0485\(1997\)027%3C1849:AEVPMF%3E2.0.CO;2](https://doi.org/10.1175/1520-0485(1997)027%3C1849:AEVPMF%3E2.0.CO;2), 1997.
 1065
 1066 Hunke, E. C., Lipscomb, W. H., Turner, A. K., Jeffery, N., and Elliott, S.: CICE: The Los Alamos sea ice model
 1067 documentation and software user’s manual version 5.1 LA-CC-06-012, Los Alamos National Laboratory, 2015.
 1068
 1069 Ikeda, M., Yao, T., and Yao, Q.: Seasonal evolution of sea ice cover and shelf water off Labrador simulated in a
 1070 coupled ice-ocean model, *J. Geophys. Res.*, 101(C7), 16465–16489, <https://doi.org/10.1029/96JC00716>, 1996.
 1071
 1072 Jacob, R., Larson, J., and Ong, E.: M x N communication and parallel interpolation in Community Climate System
 1073 Model version 3 using the Model Coupling Toolkit, *Int. J. High Perform. Comput. Appl.*, 19(3), 293–307,
 1074 <https://doi.org/10.1177/1094342005056116>, 2005.
 1075
 1076 Jin, M., Deal, C., Maslowski, W., Matrai, P., Roberts, A., Osinski, R., Lee, Y. J., Frants, M., Elliott, S., Jefferey, N.,
 1077 Hunke, E., and Wang, S.: Effects of model resolution and ocean mixing on forced ice-ocean physical and
 1078 biogeochemical simulations using global and regional system models, *J. Geophys. Res.-Oceans*, 123, 358–377,
 1079 <https://doi.org/10.1002/2017JC013365>, 2018.
 1080
 1081 Johnson, K. S. and Claustre, H.: Bringing biogeochemistry into the Argo age, *Eos*, 97,
 1082 <https://doi.org/10.1029/2016EO062427>, 2016.
 1083
 1084 Killworth, P. D.: Time interpolation of forcing fields in ocean models, *J. Phys. Oceanogr.*, 26(1), 136–143,
 1085 [https://doi.org/10.1175/1520-0485\(1996\)026%3C0136:TIOFFI%3E2.0.CO;2](https://doi.org/10.1175/1520-0485(1996)026%3C0136:TIOFFI%3E2.0.CO;2).
 1086
 1087 Körtzinger, A., Send, U., Wallace, D. W. R., Karstensen, J., and DeGrandpre, M.: Seasonal cycle of O₂ and PCO₂ in
 1088 the central Labrador Sea: Atmospheric, biological, and physical implications, *Global Biogeochem. Cy.*, 22,
 1089 GB1014, <https://doi.org/10.1029/2007GB003029>, 2008.
 1090
 1091 Kristensen, N. M., Debernard, J. B., Maartenson, S., Wang, K., and Hedstrom, K.: metno/metroms: Version 0.3 -
 1092 before merge (v0.3) [code], Zenodo, <https://doi.org/10.5281/zenodo.1046114>, 2017.
 1093
 1094 Larson, J., Jacob, R., Ong, E.: The Model Coupling Toolkit: A new Fortran90 toolkit for building Multiphysics
 1095 parallel coupled models, *Int. J. High Perform. Comput. Appl.*, 19(3), 277–292,
 1096 <https://doi.org/10.1177/1094342005056115>, 2005.
 1097
 1098 Laurent, A., Fennel, K., and Kuhn, A.: An observation-based evaluation and ranking of historical Earth system
 1099 model simulations in the northwest North Atlantic Ocean, *Biogeosciences*, 18, 1803–1822,
 1100 <https://doi.org/10.5194/bg-18-1803-2021>, 2021.

1101
1102 Lauvset, S. K., Lange, N., Tanhua, T., Bittig, H. C., Olsen, A., Kozyr, A., Álvarez, M., Becker, S., Brown, P. J.,
1103 Carter, B. R., Cotrim da Cunha, L., Feely, R. A., van Heuven, S., Hoppema, M., Ishii, M., Jeansson, E.,
1104 Jutterström, S., Jones, S. D., Karlsen, M. K., Lo Monaco, C., Michaelis, P., Murata, A., Pérez, F. F., Pfeil, B.,
1105 Schirnack, C., Steinfeldt, R., Suzuki, T., Tilbrook, B., Velo, A., Wanninkhov, R., Woosley, R. J., and Key, R. M.:
1106 An updated version of the global interior ocean biogeochemical data product, GLODAPv2.2021, *Earth Syst. Sci.*
1107 *Data*, 13, 5565–5589, <https://doi.org/10.5194/essd-13-5565-2021>, 2021.
1108
1109 Lavender, K. L., Davis, R. E., and Brechner, O. W.: Mid-depth recirculation observed in the interior Labrador and
1110 Irminger seas by direct velocity measurements, *Nature*, 407, 66–69, <https://doi.org/10.1038/35024048>, 2000.
1111
1112 Lavoie, D., Lambert, N., Starr, M., Chassé, J., Riche, O., Le Clainche, Y., Azetsu-Scott, K., Béjaoui, B., Christian, J.
1113 R., and Gilbert, D.: The Gulf of St. Lawrence Biogeochemical Model: A management tool for fisheries and ocean
1114 management, *Front. Mar. Sci.*, 8, 732269, <https://doi.org/10.3389/fmars.2021.732269>, 2021.
1115
1116 Le Fouest, V., Zakardjian, B., and Saucier, F. J.: Plankton ecosystem response to freshwater-associated bulk turbidity
1117 in the subarctic Gulf of St. Lawrence (Canada): A modelling study, *J. Marine Syst.*, 81, 75–85,
1118 <https://doi.org/10.1016/j.jmarsys.2009.12.003>, 2010.
1119
1120 Legendre, L., Ackley, S. F., Dieckmann, G. S., Gulliksen, B., Horner, R., Hoshiai, T., Melnikov, I. A., Reeburgh, W.
1121 S., Spindler, M., and Sullivan, C. W.: Ecology of sea ice biota: 2. Global significance, *Polar Biol.*, 12, 429–444,
1122 <https://doi.org/10.1007/bf00243114>, 1992.
1123
1124 Lellouche, J.-M., Greiner, E., Le Galloudec, O., Garric, G., Regnier, C., Drevillon, M., Benkiran, M., Testut, C.-E.,
1125 Bourdalle-Badie, R., Gasparin, F., Hernandez, O., Levier, B., Drillet, Y., Remy, E., and Le Traon, P.-Y. : Recent
1126 updates to the Copernicus Marine Service global ocean monitoring and forecasting real-time 1/12° high-resolution
1127 system, *Ocean Sci.*, 14, 1093–1126, <https://doi.org/10.5194/os-14-1093-2018>, 2018.
1128
1129 Lellouche, J.-M., Greiner, E., Bourdallé-Badie, R., Garric, G., Melet, A., Drévillon, M., Clement, B., Hamon, M., Le
1130 Galloudec, O., Regnier, C., Candela, T., Testut, C.-E., Gasparin, F., Ruggiero, G., Mounir, B., Yann, D., and Le
1131 Traon, P.-Y. : The Copernicus Global 1/12° Oceanic and Sea Ice GLORYS12 Reanalysis, *Front. Earth Sci.*, 9,
1132 698876, <https://doi.org/10.3389/feart.2021.698876>, 2021.
1133
1134 Lipscomb, W. H. and Hunke, E. C.: Modeling sea ice transport using incremental mapping, *Mon. Weather Rev.*,
1135 132(6), 1341–1354, [https://doi.org/10.1175/1520-0493\(2004\)132%3C1341:MSITUI%3E2.0.CO;2](https://doi.org/10.1175/1520-0493(2004)132%3C1341:MSITUI%3E2.0.CO;2), 2004.
1136
1137 Lu, Y., Higginson, S., Nudds, S., Prinsenberg, S., and Garric, G.: Model simulated volume fluxes through the
1138 Canadian Arctic Archipelago and Davis Strait: Linking monthly variations to forcings in different seasons, *J.*
1139 *Geophys. Res.-Oceans*, 119, 1927–1942, <https://doi.org/10.1002/2013JC009408>, 2014.
1140
1141 Luo, H., Bracco, A., and Zhang, F.: The seasonality of convective events in the Labrador Sea, *J. Clim.*, 27(17),
1142 6456–6471, <https://doi.org/10.1175/JCLI-D-14-00009.1>, 2014.
1143
1144 Ma, Z., Han, G., and Chassé, J.: Simulation of circulation and ice over the Newfoundland and Labrador Shelves:
1145 The mean and seasonal cycle, *Atmos.-Ocean*, 54(3), 248–263, <https://doi.org/10.1080/07055900.2015.1077325>,
1146 2016.
1147
1148 Marchesiello, P., McWilliams, J. C., and Shchepetkin, A.: Open boundary conditions for long-term integration of
1149 regional oceanic models, *Ocean Model.*, 3, 1–20, [https://doi.org/10.1016/S1463-5003\(00\)00013-5](https://doi.org/10.1016/S1463-5003(00)00013-5), 2001.
1150
1151 Marchesiello, P., Debreu, L., Couvelard, X.: Spurious diapycnal mixing in terrain-following coordinate models: The
1152 problem and a solution, *Ocean Model.*, 26, 156–169, <https://doi.org/10.1016/j.ocemod.2008.09.004>, 2009.
1153
1154 Martz, T. R., DeGrandpre, M. D., Strutton, P. G., McGillis, W. R., and Drennan, W. M.: Sea surface pCO₂ and
1155 carbon export during the Labrador Sea spring-summer bloom: An in situ mass balance approach, *J. Geophys. Res.*,
1156 114, C09008, <https://doi.org/10.1029/2008JC005060>, 2009.

1157
1158 Mason, E., Molemaker, J., Shchepetkin, A. F., Colas, F., McWilliams, J. C., and Sangrà, P.: Procedures for offline
1159 grid nesting in regional ocean models, *Ocean Model.*, 35, 1–15, <https://doi.org/10.1016/j.ocemod.2010.05.007>,
1160 2010.
1161
1162 McDougall, T. M. and Barker, P. M.: Getting started with TEOS-10 and the Gibbs Seawater (GSW) Oceanographic
1163 Toolbox, SCOR/IAPSO WG127, ISBN 978-0-646-55621-5, 2011.
1164
1165 Melsheimer, C. and Spreen, G.: AMSR2 ASI sea ice concentration data, Arctic, version 5.4 (NetCDF) (June 2012 -
1166 December 2018) [data set], PANGAEA, <https://doi.org/10.1594/PANGAEA.898399>, 2019.
1167
1168 Mellor, G. L. and Yamada, T.: Development of a turbulence closure model for geophysical fluid problems, *Rev.*
1169 *Geophys. and Space Phys.*, 20(4), 851–875, <https://doi.org/10.1029/RG020i004p00851>, 1982.
1170
1171 Mysak, L. A., Peng, S., and Wood, R. G.: Application of a coupled ice-ocean model to the Labrador Sea, *Atmos.-*
1172 *Ocean*, 29(2), 232–255, <https://doi.org/10.1080/07055900.1991.9649404>, 1991.
1173
1174 Naughten, K. A., Galton-Fenzi, B. K., Meissner, K. J., England, M. H., Brassington, G. B., Colberg, F., Hatterman,
1175 T., and Debernard, J. B.: Spurious sea ice formation caused by oscillatory ocean tracer advection schemes, *Ocean*
1176 *Model.*, 116, 108–117, <https://doi.org/10.1016/j.ocemod.2017.06.010>, 2017.
1177
1178 Ohashi, K., Laurent, A., Renkl, C.: Sheng, J., Fennel, K., and Oliver, E.: DALROMS-NWA12 v1.0, a coupled
1179 circulation-sea ice-biogeochemistry model for the northwest North Atlantic: codes and namelists (Version v3)
1180 [software], Zenodo, <https://doi.org/10.5281/zenodo.12752091>, 2024a.
1181
1182 Ohashi, K., Laurent, A., Renkl, C., Sheng, J., Fennel, K., and Oliver, E.: DALROMS-NWA12 v1.0, a coupled
1183 circulation-sea ice-biogeochemistry model for the northwest North Atlantic: input files (1 of 3) (Version v2) [data
1184 set], Zenodo, <https://doi.org/10.5281/zenodo.12752190>, 2024b.
1185
1186 Ohashi, K., Laurent, A., Renkl, C., Sheng, J., Fennel, K., and Oliver, E.: DALROMS-NWA12 v1.0, a coupled
1187 circulation-sea ice-biogeochemistry model for the northwest North Atlantic: input files (2 of 3) (Version v1) [data
1188 set], Zenodo, <https://doi.org/10.5281/zenodo.12734049>, 2024c.
1189
1190 Ohashi, K., Laurent, A., Renkl, C., Sheng, J., Fennel, K., and Oliver, E.: DALROMS-NWA12 v1.0, a coupled
1191 circulation-sea ice-biogeochemistry model for the northwest North Atlantic: input files (3 of 3) (Version v1) [data
1192 set], Zenodo, <https://doi.org/10.5281/zenodo.12735153>, 2024d.
1193
1194 Ohashi, K., Laurent, A., Renkl, C., Sheng, J., Fennel, K., and Oliver, E.: DALROMS-NWA12 v1.0, a coupled
1195 circulation-sea ice-biogeochemistry model for the northwest North Atlantic: output files (1 of 2) (Version v1) [data
1196 set], Zenodo, <https://doi.org/10.5281/zenodo.12744506>, 2024e.
1197
1198 Ohashi, K., Laurent, A., Renkl, C., Sheng, J., Fennel, K., and Oliver, E.: DALROMS-NWA12 v1.0, a coupled
1199 circulation-sea ice-biogeochemistry model for the northwest North Atlantic: output files (2 of 2) (Version v1) [data
1200 set], Zenodo, <https://doi.org/10.5281/zenodo.12746262>, 2024f.
1201
1202 Pawlowicz, R.: M_Map: A mapping package for MATLAB, version 1.4m [software],
1203 <https://www.eoas.ubc.ca/~rich/map.html>, 2020.
1204
1205 Pei, Q.: Study of circulation, hydrography and dissolved oxygen concentration over coastal waters of the Scotian
1206 Shelf, M.Sc. thesis, Dalhousie University, <http://hdl.handle.net/10222/81682>, 2022.
1207
1208 Pennelly, C. and Myers, P. G.: Introducing LAB60: A 1/60° NEMO 3.6 numerical simulation of the Labrador Sea,
1209 *Geosci. Model Dev.*, 13, 4959–4975, <https://doi.org/10.5194/gmd-13-4959-2020>, 2020.
1210
1211 Pepin, P., Petrie, B., Therriault, J.-C., Narayanan, S., Harrison, W. G., Frank, K. T., Chassé, J., Colbourne, E. B.,
1212 Gilbert, D., Gregory, D., Harvey, M., Maillet, G. L., Mitchell, M., and Starr, M.: The Atlantic Zone Monitoring

1213 Program (AZMP): Review of 1998–2003 (Can. Tech. Rep. Hydrogr. Ocean Sci. 242), Fisheries and Oceans
1214 Canada, 2005.
1215
1216 Prinsenberg, S. J. and Peterson, I. K.: Sea-ice properties off Labrador and Newfoundland during LIMEX '89,
1217 Atmos.-Ocean, 30(2), 207–222, <https://doi.org/10.1080/07055900.1992.9649438>, 1992.
1218
1219 Rhein, M., Steinfeldt, R., Kieke, D., Stendardo, I., and Yashayaev, I.: Ventilation variability of Labrador Sea Water
1220 and its impact on oxygen and anthropogenic carbon: a review, Phil. Trans. R. Soc. A, 375, 20160321,
1221 <https://doi.org/10.1098/rsta.2016.0321>, 2017.
1222
1223 Richaud, B., Fennel, K., Oliver, E. C. J., DeGrandpre, M. D., Bourgeois, T., Hu, X., and Lu, Y.: Underestimation of
1224 oceanic carbon uptake in the Arctic Ocean: ice melt as predictor of the sea ice carbon pump, Cryosphere, 17,
1225 2665–2680, <https://doi.org/10.5194/tc-17-2665-2023>, 2023.
1226
1227 Richaud, B., Kwon, Y.-O., Joyce, T. M., Fratantoni, P. S., and Lentz, S. J.: Surface and bottom temperature and
1228 salinity climatology along the continental shelf off the Canadian and U.S. east coasts, Cont. Shelf Res., 124, 165–
1229 181, <https://doi.org/10.1016/j.csr.2016.06.005>, 2016.
1230
1231 Ridenour, N. A., Hu, X., Sydor, K., Myers, P. G., and Barber, D. G.: Revisiting the circulation of Hudson Bay:
1232 Evidence for a seasonal pattern, Geophys. Res. Lett., 46, 3891–3899, <https://doi.org/10.1029/2019GL082344>,
1233 2019.
1234
1235 Ross, A. C., Stock, C. A., Adcroft, A., Curchitser, E., Hallberg, R., Harrison, M. J., Hedstrom, K., Zadeh, N.,
1236 Alexander, M., Chen, W., Drenkard, E. J., du Pontavice, H., Dussin, R., Gomez, F., John, J. G., Kang, D., Lavoie,
1237 D., Resplandy, L., Roobaert, A., Saba, V., Shin, S., Siedlecki, S., and Simkins, J.: A high-resolution physical-
1238 biological model for marine resource applications in the northwest Atlantic (MOM6-COBALT-NWA12 v1.0),
1239 Geosci. Model Dev., 16, 6943–6985, <https://doi.org/10.5194/gmd-16-6943-2023>, 2023.
1240
1241 Rutherford, K. and Fennel, K.: Elucidating coastal ocean carbon transport processes: A novel approach applied to
1242 the northwest North Atlantic shelf, Geophys. Res. Lett., 49, e2021GL097614,
1243 <https://doi.org/10.1029/2021GL097614>, 2022.
1244
1245 Saucier, F. J., Senneville, S., Prinsenberg, S., Roy, F., Smith, G., Gachon, P., Caya, D., and Laprise, R.: Modelling
1246 the sea ice-ocean seasonal cycle in Hudson Bay, Foxe Basin and Hudson Strait, Canada, Clim. Dynam., 23, 303–
1247 326, <https://doi.org/10.1007/s00382-004-0445-6>, 2004.
1248
1249 Schwab, D. J., Clites, A. H., Murthy, C. R., Sandall, J. E., Meadows, L. R., and Meadows, G. A.: The effect of wind
1250 on transport and circulation in Lake St. Clair, J. Geophys. Res., 94(C4), 4947–4958,
1251 <https://doi.org/10.1029/JC094iC04p04947>, 1989.
1252
1253 Shapiro, R.: Linear filtering, Math. Comput., 19(132), 1094–1097, <https://doi.org/10.1090/S0025-5718-1975-0389356-X>, 1975.
1254
1255 Sheng, J.: Circulation and drift pathways in the northwest Atlantic Ocean, in: Estuarine and Coastal Modeling:
1256 Proceedings of the Seventh International Conference, St. Petersburg, FL, 5–7 November 2001, 364–383,
1257 [https://doi.org/10.1061/40628\(268\)23](https://doi.org/10.1061/40628(268)23), 2002.
1258
1259 Smith, G. C., Roy, F., and Brasnett, B.: Evaluation of an operational ice-ocean analysis and forecasting system for
1260 the Gulf of St. Lawrence, Q. J. Roy. Meteor. Soc., 139, 419–433, <https://doi.org/10.1002/qj.1982>, 2013.
1261
1262 Song, Y. and Haidvogel, D.: A semi-implicit ocean circulation model using a generalized topography-following
1263 coordinate system. J. Comput. Phys., 115(1), 228–244, <https://doi.org/10.1006/jcph.1994.1189>.
1264
1265 St. Lawrence Global Observatory: Freshwater runoffs of the St. Lawrence at the height of Québec City [data set],
1266 https://catalogue.ogsl.ca/dataset/ca-cioos_84a17ffc-4898-4261-94de-4a5ea2a9258d?local=en, 2023.
1267
1268

1269 Strutton, P. G., Martz, T. R., DeGrandpre, M. D., McGillis, W. R., Drennan, W. M., and Boss, E.: Bio-optical
1270 observations of the 2004 Labrador Sea phytoplankton bloom, *J. Geophys. Res.*, 116, C11037,
1271 <https://doi.org/10.1029/2010JC006872>, 2011.

1272

1273 Szekely, T.: Product user manual: In situ TAC objective analysis products, v1.11, Mercator Ocean International,
1274 2023.

1275

1276 Takahashi, T., Sutherland, S. C., Wanninkhof, R., Sweeney, C., Feely, R.A., Chipman, D. W., Hales, B., Friederich,
1277 G., Chavez, F., Sabine, C., Watson, A., Bakker, D. C. E., Schuster, U., Metzl, N., Yoshikawa-Inoue, H., Ishii, M.,
1278 Midorikawa, T., Nojiri, Y., Körtzinger, A., Steinhoff, T., Hoppema, M., Olafsson, J., Arnarson, T. S., Tilbrook, B.,
1279 Johannessen, T., Olsen, A., Bellerby, R., Wong, C. S., Delille, B., Bates, N. R., de Barr, H. J. W., Climatological
1280 mean and decadal change in surface ocean pCO₂, and net sea-air CO₂ flux over the global oceans, *Deep-Sea Res.*
1281 Pt. II, 56, 554–577, <https://doi.org/10.1016/j.dsr2.2008.12.009>, 2009.

1282

1283 Tang, C. L., Gui, Q., and DeTracey, B. M.: A modeling study of upper ocean winter processes in the Labrador Sea, *J.*
1284 *Geophys. Res.*, 104(C10), 23411–23425, <https://doi.org/10.1029/1999JC900214>, 1999.

1285

1286 The Lab Sea Group: The Labrador Sea Deep Convection Experiment, *B. Am. Meteorol. Soc.*, 79(10), 2033–2058,
1287 [https://doi.org/10.1175/1520-0477\(1998\)079%3C2033:TLSDCE%3E2.0.CO;2](https://doi.org/10.1175/1520-0477(1998)079%3C2033:TLSDCE%3E2.0.CO;2), 1998.

1288

1289 Thyng, K. M., Greene, C. A., Hetland, R. D., Zimmerle, H. M., and DiMarco, S. F.: True colors of oceanography:
1290 Guidelines for effective and accurate colormap selection. *Oceanography*, 29(3), 9-13,
1291 <https://doi.org/10.5670/oceanog.2016.66>, 2016.

1292

1293 Tian, R. C., Deibel, D., Rivkin, R. B., and Vézina, A. F.: Biogenic carbon and nitrogen export in a deep-convection
1294 region: simulations in the Labrador Sea, *Deep-Sea Res. Pt. I*, 51, 413–437,
1295 <https://doi.org/10.1016/j.dsr.2003.10.015>, 2004.

1296

1297 Urrego-Blanco, U., and Sheng, J.: Study on subtidal circulation and variability in the Gulf of St. Lawrence, Scotian
1298 Shelf, and Gulf of Maine using a nested-grid shelf circulation model, *Ocean Dynam.*, 64, 385–412,
1299 <https://doi.org/10.1007/s10236-013-0688-z>, 2014.

1300

1301 Volk, T. and Hoffert, M. I.: Ocean carbon pumps: Analysis of relative strengths and efficiencies in ocean-driven
1302 atmospheric CO₂ changes, in: *The carbon cycle and atmospheric CO₂: Natural variations Archean to present*,
1303 *Geoph. Monog. Series vol. 32*, edited by Sundquist, E. T. and Broecker, W. S., 99–110,
1304 <https://doi.org/10.1029/GM032p0099>, 1985.

1305

1306 Wang, B., Fennel, K., An assessment of vertical carbon flux parameterizations using backscatter data from BGC
1307 Argo, *Geophys. Res. Lett.*, <https://doi.org/10.1029/2022GL101220>, 2023.

1308

1309 Wang, B., Fennel, K., Biogeochemical Argo data suggest only a minor contribution of small particles to long-term
1310 carbon sequestration in the subpolar North Atlantic, *Limnol. Oceanogr.*, <https://doi.org/10.1002/lno.12209>, 2022.

1311

1312 Wang, Y., Sheng, J., and Lu, Y.: Examining tidal impacts on seasonal circulation and hydrography variability over
1313 the eastern Canadian shelf using a coupled circulation-ice regional model, *Prog. Oceanogr.*, 189, 102448,
1314 <https://doi.org/10.1016/j.pocean.2020.102448>, 2020.

1315

1316 Wang, Z., Lu, Y., Greenan, B., Brickman, D., and DeTracey, B.: BNAM: An eddy-resolving North Atlantic Ocean
1317 model to support ocean monitoring. (*Can. Tech. Rep. Hydrogr. Ocean Sci.* 327), Fisheries and Oceans Canada,
1318 2018.

1319

1320 Wu., Y., Peterson, I. K., Tang, C. C. L., Platt, T., Sathyendranath, S., and Fuentes-Yaco, C.: The impact of sea ice on
1321 the initiation of the spring bloom on the Newfoundland and Labrador Shelves, *J. Plankton. Res.*, 29(6), 509–514,
1322 <https://doi.org/10.1093/plankt/fbm035>, 2007.

1323

1324 Wu, Y., Platt, T., Tang, C. C. L., and Sathyendranath, S.: Regional differences in the timing of the spring bloom in
1325 the Labrador Sea, *Mar. Ecol. Prog. Ser.*, 355, 9–20, <https://doi.org/10.3354/meps07233>, 2008.
1326
1327 Wu, Y., Tang, C., and Hannah, C.: The circulation of eastern Canadian seas, *Prog. Oceanogr.*, 106, 28–48,
1328 <https://doi.org/10.1016/j.pocean.2012.06.005>, 2012.
1329
1330 Wu, H. and Zhu, J.: Advection scheme with 3rd high-order spatial interpolation at the middle temporal level and its
1331 application to saltwater intrusion in the Changjiang Estuary, *Ocean Model.*, 33(1–2), 33–51,
1332 <https://doi.org/10.1016/j.ocemod.2009.12.001>, 2010.
1333
1334 Yang, B., Fox, J., Behrenfeld, M. J., Boss, E. S., Haëntjens, N., Halsey, K. H., Emerson, S. R., and Doney, S. C.: In
1335 situ estimates of net primary production in the western North Atlantic with Argo profiling floats, *J. Geophys.*
1336 *Res.-Biogeo.*, 126, e2020JG061116, <https://doi.org/10.1029/2020JG061116>, 2020.
1337
1338 Yang, S., Sheng, J., Ohashi, K., Yang, B., Chen, S., Xing, J.: Non-linear interactions between tides and storm surges
1339 during extreme weather events over the eastern Canadian shelf, *Ocean Dynam.*, 73, 279–301,
1340 <https://doi.org/10.1007/s10236-023-01556-w>, 2023.
1341
1342 Yao, T., Tang, C. L., and Peterson, I. K.: Modeling the seasonal variation of sea ice in the Labrador Sea with a
1343 coupled multicategory ice model and the Princeton Ocean Model, *J. Geophys. Res.*, 105(C1), 1153–1165,
1344 <https://doi.org/10.1029/1999JC900264>, 2000.
1345
1346 Yashayaev, I.: Intensification and shutdown of deep convection in the Labrador Sea were caused by changes in
1347 atmospheric and freshwater dynamics, *Commun. Earth Environ.*, 5, 1–23, [https://doi.org/10.1038/s43247-024-](https://doi.org/10.1038/s43247-024-01296-9)
1348 [01296-9](https://doi.org/10.1038/s43247-024-01296-9), 2024.
1349
1350 Yashayaev, I. and Loder, J. W.: Further intensification of deep convection in the Labrador Sea in 2016, *Geophys.*
1351 *Res. Lett.*, 44(3), 1429–1438, <https://doi.org/10.1002/2016GL071668>, 2017.
1352
1353 Zhang, S., Sheng, J., and Greatbatch, R. J.: A coupled ice-ocean modeling study of the northwest Atlantic Ocean, *J.*
1354 *Geophys. Res.*, 109, C04009, <https://doi.org/10.1029/2003JC001924>, 2004.
1355